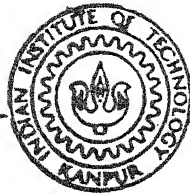


# EFFECT OF Ta AND B ADDITIONS ON THE STABILITY OF $\text{Ni}_3\text{Al}$ INTERMETALLIC PHASE

by

DEBASHISH BHATTACHARJEE



DEPARTMENT OF METALLURGICAL ENGINEERING  
INDIAN INSTITUTE OF TECHNOLOGY, KANPUR

APRIL, 1989

ME  
1989  
M  
BHA  
SFA

# EFFECT OF Ta AND B ADDITIONS ON THE STABILITY OF $\text{Ni}_3\text{Al}$ INTERMETALLIC PHASE

*A Thesis Submitted  
In Partial Fulfilment of the Requirements  
for the Degree of  
MASTER OF TECHNOLOGY*

*by*  
DEBASHISH BHATTACHARJEE

*to the*  
DEPARTMENT OF METALLURGICAL ENGINEERING  
INDIAN INSTITUTE OF TECHNOLOGY, KANPUR  
APRIL, 1989

105931

ME-1989-M-BHA-EFF

11)  
20/4/89  
Dy. Prof.

CERTIFICATE

This is to certify that the work on "EFFECT OF A AND B ADDITIONS ON THE STABILITY OF  $\text{Ni}_3\text{Al}$  INTERMETALLIC PHASE" has been carried out by Mr. Debashish Bhattacharjee under my supervision and it has not been submitted elsewhere for a degree.

April, 1989.

(K.P. Gupta)  
Professor  
Department of Metallurgical Engineering  
Indian Institute of Technology  
Kanpur



ACKNOWLEDGEMENTS

Working with Professor K.P. Gupta has been a very good and memorable experience. I feel myself privileged to have been able to work with him. With his excellent guidance and constant advice he has made this work very interesting and I esteem very much the valuable experience I gained under his supervision.

I owe greatly to Professor A.K. Jena for his immense encouragement to pursue this work and for giving me the opportunity to work in the field of Phase Transformations and Phase Stability.

I would like to acknowledge the guidance and valuable help of Professor R.K. Ray in the early stages of this work.

It gives me great pleasure to thank my colleagues. I would like to acknowledge specially the help I got from Mr. Jitendra Singh Sachan, without which completing the work would have been an enormously difficult job. I would also like to thank Mr. I. Mukherjee, Mr. S.R. Ponkshe, Mr. R.R. Nagr, Mr. A. Singhal, Mr. N.K. Nath and Dr. H.K. Gupta for their valuable assistance at various stages of the work. I also thank Ms. S. Bardhan for her help.

I am grateful to Mr. V. Kumar and Mr. G.S. Thapa for their resourcefulness and help in the experimental stages of

my work, and the latter also for drawing the figures in this thesis.

The pain and immense care that Mr. U.S. Misra took in typing the manuscript in a very short time is gratefully acknowledged.

-DEBASHISH BHATTACHARJEE

CONTENTS

|  | <u>Page</u> |
|--|-------------|
| LIST OF TABLES   | viii)       |
| LIST OF FIGURES  | x)          |
| ABSTRACT   | xiv)        |
| <br>CHAPTER 1  |             |
| INTRODUCTION   | 1           |
| <br>CHAPTER 2  |             |
| LITERATURE REVIEW  | 3           |
| 2.1 Superalloys  | 3           |
| 2.2 Nickel-Base Superalloys                                  | 4           |
| 2.2.1 Gamma Prime Phase ( $\gamma'$ )                        | 5           |
| 2.2.2 $\text{Ni}_3\text{Al}$ ( $\gamma'$ ) in Ni-Al-X Alloys | 6           |
| 2.2.3 The Ni-Al-Ta System                                    | 9           |
| 2.3 Binary Systems   | 9           |
| 2.3.1 Ni-Al System   | 9           |
| 2.3.2 Ni-Ta System   | 12          |
| 2.3.3 Al-Ta System   | 15          |
| 2.4 Ni-Al-Ta Ternary System                                  | 17          |
| 2.5 Effect of Boron on $\text{Ni}_3\text{Al}$                | 21          |
| 2.5.1 Solubility, Segregation                                | 21          |
| Characteristics, and Effect on                               |             |
| Lattice Properties   |             |
| 2.5.2 Improvement of Ductility                               | 24          |
| 2.6 Mechanical Properties of $\text{Ni}_3\text{Al}$ and the  | 25          |
| Effect of Alloying Additions                                 |             |
| 2.6.1 Effect of Alloying Addition and                        | 26          |
| Solution Strengthening                                       |             |
| 2.7 Statement of Problem                                     | 28          |
| REFERENCES   | 30          |
| <br>CHAPTER 3  |             |
| EXPERIMENTAL PROCEDURE                                       | 34          |
| 3.1 Alloy Preparation  | 34          |
| 3.1.1 Alloys Containing Boron                                | 34          |
| 3.1.2 Alloys Not Containing Boron                            | 34          |
| 3.2 Melting  | 35          |
| 3.3 Homogenization   | 36          |
| 3.4 Equilibration at $1000^\circ\text{C}$                    | 37          |
| 3.5 X-ray Diffraction  | 37          |
| 3.5.1 Sample Preparation                                     | 37          |
| 3.5.2 The Sample Holder                                      | 38          |
| 3.5.3 X-ray Diffraction                                      | 39          |
| 3.6 Optical Microscopy                                       | 42          |
| 3.7 Microhardness-Measurements                               | 43          |
| 3.8 Differential Scanning Calorimetry                        | 43          |

|  | <u>Page</u> |
|--|-------------|
| CHAPTER 4      RESULTS   | 44          |
| 4.1 Indexing of the X-ray Diffraction Patterns   | 44          |
| 4.2 Method for Lattice Parameter Measurement   | 45          |
| 4.3 Homogenization   | 48          |
| 4.4 Lattice Parameter of Alloys Annealed at 1200°C   | 50          |
| 4.5 Lattice Parameters of Alloys Annealed at 1000°C  | 53          |
| 4.5.1 Indexing of the Diffraction Patterns obtained at 1000°C                                    | 53          |
| 4.5.2 Lattice Parameters of the Alloys at 1000°C   | 55          |
| 4.6 Optical Microscopy   | 55          |
| 4.6.1 Choice of Etching Reagent  | 55          |
| 4.6.2 The Photomicrographs   | 59          |
| 4.7 The Differential Scanning Calorimetry of Ni-Al-Ta Alloys                                     | 74          |
| 4.8 Microhardness  | 74          |
| 4.9 Measurement of Intensity of Diffraction Peaks  | 78          |
| REFERENCES   | 80          |
| CHAPTER 5      DISCUSSION  | 81          |
| 5.1 Composition of the Alloys  | 81          |
| 5.2 Homogenizing Temperature   | 82          |
| 5.3 Lattice Parameters of the $\gamma'$ Phase  | 83          |
| 5.4 Analysis of Diffraction Peaks due to the Unknown Phase                                       | 84          |
| 5.5 Microstructure and Phase Boundary  | 91          |
| 5.6 Analysis of the Split Diffraction Peaks  | 93          |
| 5.6.1 Differential Scanning Calorimetry  | 94          |
| 5.7 Structural Analysis of the Split Diffraction Peaks   | 97          |
| 5.7.1 Intensity Calculations for Ni <sub>3</sub> Al at 1000°C                                    | 98          |
| 5.7.2 Intensity Calculations for Ni <sub>3</sub> Al with 1 atom % Ta and Containing B, at 1000°C | 101         |
| REFERENCES   | 106         |
| CHAPTER 6      CONCLUSIONS   | 107         |
| CHAPTER 7      SCOPE FOR FUTURE WORK   | 108         |

|   | <u>Page</u> |
|---|-------------|
| APPENDIX A      Calculation of Weight of Ingredients<br>for Making 15 GMS of Boron Doped Alloy      | 110         |
| APPENDIX B      Calculations for Lattice Parameter  | 112         |
| APPENDIX C      Structure Factor and Intensity Calculations<br>for Ordered $\text{Ni}_3\text{Al}$ . | 114         |

| <u>Table No.</u> | <u>Caption</u>   | <u>Page</u> |
|------------------|--|-------------|
| 5.1              | Melting loss of some alloys  | 81          |
| 5.2              | Comparison of the set of unknown peaks<br>with the diffraction patterns of phases in<br>the Ni-Al-Ta system  | 86          |
| 5.3              | Comparison of the set of unknown peaks<br>with the diffraction pattern of NiAlTa<br>phase  | 87          |
| 5.4              | Indexing of the unknown peaks of B-doped,<br>7at% Ta on the basis of a fcc structure   | 88          |
| 5.5              | Comparison of the set of unknown peaks<br>with the diffraction pattern of TaC  | 88          |
| 5.6              | Lattice parameter of $\text{Ni}_3\text{Al}$ as a function of<br>composition  | 95          |
| 5.7              | Calculated and observed relative intensities<br>of the phases separated in $\text{Ni}_3\text{Al}$ at $1000^\circ\text{C}$<br>due to a miscibility gap              | 100         |
| 5.8              | Calculated and observed relative intensities<br>of the phases separated in $\text{Ni}_3\text{Al}$ with 1 at %<br>Ta due to miscibility gap at $1000^\circ\text{C}$ | 102         |
| 5.8              | Ratio of the scaled relative intensities<br>of the first two superlattice lines (100)<br>and (110) reflections)  | 104         |
| A.1              | Calculation of correction factor   | 112         |
| A.2              | The calculated relative intensities compared<br>with observed relative intensities of $\text{Ni}_3\text{Al}$ .   | 116         |

# LIST OF TABLES

| <u>Table No.</u> | <u>Caption</u>  | <u>Page</u> |
|------------------|---|-------------|
| 2.1              | Crystal structures and lattice parameters of different phases in the Ni-NiAl-Ni <sub>3</sub> Ta triangle                                  | 22          |
| 2.2              | Limiting compositions of phases near the $\gamma'$ region in Ni-Al-Ta system  | 22a         |
| 4.1              | Diffraction pattern of the master alloy (Ni <sub>3</sub> Al with B)   | 46          |
| 4.2              | Indexing of the diffraction patterns of alloy containing 7 at % Ta and B  | 47          |
| 4.3              | Lattice parameters of alloys containing Boron, at 1200°C  | 51          |
| 4.4              | Lattice parameters of alloys not containing Boron, at 1200°C  | 51          |
| 4.5              | Diffraction pattern of B-doped alloy containing 1 at % Ta, at 1000°C, showing two sets of peaks due to two Ni <sub>3</sub> Al type phases | 54          |
| 4.6              | Lattice parameters of alloy containing Boron, at 1000°C   | 56          |
| 4.7              | Lattice parameters of alloy not containing Boron, at 1000°C   | 56          |
| 4.8              | Details of DSC run  | 75          |
| 4.9              | Scaled integrated intensities from area under diffraction peaks   | 78          |

LIST OF FIGURES

| <u>Fig.No.</u> | <u>Caption</u>   | <u>Page</u> |
|----------------|--|-------------|
| 2.1            | The $L1_2$ structure   | 7           |
| 2.2            | Anomalous behaviour of $Ni_3Al$  | 7           |
| 2.3            | Al-Ni binary phase diagram   | 11          |
| 2.4            | Ni-Ta binary phase diagram   | 14          |
| 2.5            | Al-Ta binary phase diagram   | 16          |
| 2.6            | Isotherm of Ni-Al-Ta system  | 19          |
| 2.7            | Isotherm of Ni-Al-Ta system  | 20          |
| 4.1            | Plot of lattice parameter versus Nelson-Riley function   | 49          |
| 4.2            | Plot of lattice parameter versus time of homogenization at $1200^{\circ}C$                     | 49          |
| 4.3            | Plot of lattice parameter versus Ta content at $1200^{\circ}C$                                 | 52          |
| 4.4            | Splitting of the (100) peak of $Ni_3Al$ at $1000^{\circ}C$                                     | 52          |
| 4.5            | Plot of lattice parameter versus Ta content of Alloys containing Boron, at $1000^{\circ}C$     | 57          |
| 4.6            | Plot of lattice parameter versus Ta content of alloys not containing Boron, at $1000^{\circ}C$ | 58          |
| 4.7            | Photomicrograph of As-Cast structure of alloy buttons. Mag: 100X                               | 62          |
| 4.8            | Photomicrograph of Boron-doped 1at% Ta alloy, at $1200^{\circ}C$ . Mag: 500X                   | 63          |
| 4.9            | Photomicrograph of without-Boron 1at% Ta alloy, at $1200^{\circ}C$ . Mag: 500X                 | 63          |



| <u>Fig. No.</u> | <u>Caption</u>  | <u>Page</u> |
|-----------------|---|-------------|
| 4.10            | Photomicrograph of Boron-doped 3at% Ta alloy, at 1200°C. Mag:200X                                 | 64          |
| 4.11            | Photomicrograph of without-Boron 3at% Ta alloy, at 1200°C, before etching, Mag: 100X              | 64          |
| 4.12            | Photomicrograph of without-Boron 3at% Ta alloy, at 1200°C, after etching. Mag: 200X               | 65          |
| 4.13            | Photomicrograph of Boron-doped 7at% Ta alloy, at 1200°C, before etching. Mag: 100X                | 65          |
| 4.14            | Photomicrograph of Boron-doped 7at% Ta alloy, at 1200°C, after etching. Mag: 100X                 | 66          |
| 4.15            | Photomicrograph of without-Boron 7at% Ta alloy, at 1200°C, before etching, Mag: 100X              | 66          |
| 4.16            | Photomicrograph of without-Boron 7at% Ta alloy, at 1200°C, after 5 minutes of etching. Mag: 100X  | 67          |
| 4.17            | Photomicrograph of without-Boron 7at% Ta alloy, at 1200°C, after 10 minutes of etching. Mag: 500X | 67          |
| 4.18            | Photomicrograph of Boron doped, 9at% Ta alloy, at 1200°C, before etching, Mag: 100X               | 68          |
| 4.19            | Photomicrograph of Boron-doped, 9at% Ta alloy, at 1200°C, after 5 minutes etching. Mag: 500X      | 68          |
| 4.20            | Photomicrograph of Boron-doped 9at% Ta alloy, at 1200°C, after 10 minutes of etching. Mag: 200X   | 69          |

| <u>Fig.No.</u> | <u>Caption</u>   | <u>Page</u> |
|----------------|--|-------------|
| 4.21           | Photomicrograph of without-Boron, 9at% Ta alloy, at 1200°C, before etching. Mag:100X               | 69          |
| 4.22           | Photomicrograph of without Boron, 9at% Ta alloy, at 1200°C after 10 minutes of etching. Mag: 100X  | 70          |
| 4.23           | Photomicrograph of without Boron, 9at% Ta alloy, at 1200°C after 10 minutes of etching. Mag: 500X  | 70          |
| 4.24           | Photomicrograph of without-Boron, 1at% Ta alloy, at 1200°C, after 10 minutes of etching. Mag: 100X | 71          |
| 4.25           | Photomicrograph of without-Boron, 3at% Ta alloy, at 1200°C, before etching. Mag:500X               | 71          |
| 4.26           | Photomicrograph of without-Boron, 7at% Ta alloy, at 1000°C, after 10 minutes of etching. Mag: 100X | 72          |
| 4.27           | Photomicrograph of Boron-doped, 9at% Ta alloy, at 1000°C, after 10 minutes of etching. Mag: 100X   | 72          |
| 4.28           | Photomicrograph of without-Boron, 9at% Ta alloy, at 1000°C, before etching. Mag: 100X              | 73          |
| 4.29           | Photomicrograph of without-Boron, 9at% Ta alloy at 1000°C, after 10 minutes of etching. Mag: 500X  | 73          |
| 4.30           | The differential scanning calorimeter plots for two samples  | 76          |

| <u>Fig.No.</u> | <u>Caption</u>  | <u>Page</u> |
|----------------|---|-------------|
| 4.31           | Extrapolation of peaks for area calculations  | 79          |
| 5.1            | The split 100 peaks for Boron doped $\text{Ni}_3\text{Al}$ without Ta and containing 1 at % Ta. | 105         |

## ABSTRACT

In the present work an attempt has been made to study the phase stability of  $\text{Ni}_3\text{Al}$  (with or without B) on the addition of Ta. The phase stability study has been made at two temperatures:  $1200^\circ\text{C}$  and  $1000^\circ\text{C}$ . In the present study, x-ray diffraction is extensively used along with microstructural and differential scanning calorimetry studies. Lattice parameters, obtained from the X-ray diffraction patterns of the alloys, show increase with increasing addition of Ta. Addition of Boron, however, decreases the lattice parameter. Microstructural studies indicate that the phase boundary of  $\text{Ni}_3\text{Al}$  alloyed with Ta, along the 75 at % Ni line, is between 7 at % Ta and 9 at % Ta. Diffraction peaks other than those of  $\text{Ni}_3\text{Al}$ , are obtained in all the alloys that contain Ta. Microstructures of the alloys containing Ta show precipitation of a brittle phase at the grain boundaries. High values of microhardness obtained for these particles at the grain boundaries, and the analysis of the extra diffraction peaks suggest that the grain boundary precipitated phase is  $\text{TaC}$ . At  $1000^\circ\text{C}$  all the diffraction peaks of  $\text{Ni}_3\text{Al}$  have split into two peaks, including the superlattice reflection. The possibility of existence of a miscibility gap in the

$\text{Ni}_3\text{Al}$  region has been hypothesized. Differential scanning calorimetry shows an irreversible endothermic reaction occurring in the temperature region between  $900^\circ\text{C}$  and  $1100^\circ\text{C}$ . Intensity calculations based on assumed compositions for the separated phases, due to the miscibility gap, show reasonable match with the observed intensities of the diffraction peaks. The DSC results and structural analysis support the hypothesis regarding the existence of a miscibility gap.

## CHAPTER 1

### INTRODUCTION

Studies on intermetallics and superalloys form the leading edge of research on materials today. Ni-base intermetallics and superalloys are by far the most important of all materials in this category. The  $\text{Ni}_3\text{Al}$  intermetallic is unique for its strange mechanical property by which its proof stress increases with temperature upto about 600-700°C. By virtue of this property  $\text{Ni}_3\text{Al}$  becomes the ideal material for high temperature use.

Pure polycrystalline  $\text{Ni}_3\text{Al}$  is extremely brittle. Its ductility improves remarkably by even a very small addition of Boron. Ternary solute elements add to the strength of  $\text{Ni}_3\text{Al}$  by imparting solution strengthening.

The improvement of mechanical properties of any alloy by the addition of solutes can be fully utilized if the phase diagram of the system is known. The phase boundary of a phase can be detected by the change in slope of the lattice parameter versus composition plot. Presence of an unknown phase in the microstructure may complicate the situation. In that case phase boundary can be established with the help of microstructure.

If any new phases appears, either in the X-ray or in microstructure the new phase can be identified by indexing the diffraction pattern and comparing with the diffraction patterns of known phases. If this method fails, structural analysis can be done on the basis of assumed compositions. Structure factor calculations on the basis of the assumed compositions, should predict the relative intensities of the diffraction peaks if the assumptions are correct.

In the present work effect of Ta and B on the phase stability of  $\text{Ni}_3\text{Al}$  has been studied.

## CHAPTER 2

### LITERATURE REVIEW

#### 2.1 SUPERALLOYS

Many definitions of superalloys have appeared over the years. Superalloys are a class of materials around which it is difficult to create an exact boundary (1) . However, a reasonable acceptable definition would be: "A superalloy is an alloy, usually based on group VIIIA elements, developed for elevated temperature service, where relatively severe mechanical stressing is encountered, and where high surface stability is frequently required" (2) .

Superalloys are divided into three classes: Ni-base superalloys, Co-base superalloys, and Fe-base superalloys. In addition, a major subgroup, those that have metallurgical characteristics similar to the Ni-base superalloys but contain relatively large Fe contents, are called Ni-Fe superalloys.

Superalloys, because of their retention of strength at high temperatures, are used at a high proportion of their actual melting point than any other class of broadly commercial metallurgical materials. These materials have made much of our high-temperature technology possible.



## 2.2 NICKEL-BASE ALLOYS

The Ni-base alloys are the most complex and perhaps the most widely used material for high temperature applications of all the superalloys. Their use extends to the highest homologous temperatures of any common alloy system, and they currently comprise over 50% of the weight of advanced aircraft engines. Their physical metallurgy is complex, subtle and sophisticated (3) .

The alloying elements that the Ni-base superalloys may contain are Cr, Al, Ti, B, Zr, C, Mo, W, Nb, Ta and Hf. These elements tend to be grouped with some common characteristics in the periodic system. Accordingly, we can divide them into certain classes (3) .

The first class consists of elements that prefer and make up the face-centered cubic  $\gamma$  -matrix. These are from Groups V, VI and VII and include Co, Fe, Cr, Mo and W. The second class of elements partition to make up the  $\gamma'$  precipitate  $\text{Ni}_3\text{X}$ . These elements are from Groups III, IV, and V and include Al, Ti, Nb, Ta and Hf. N, C and Zr make up a third class of elements that tend to segregate to grain boundaries. These elements are from Groups II, III and IV and are very odd sized in atomic diameter.

The major phases that may be found in Ni-base superalloys are:

1. Gamma Matrix ( $\gamma$ )
2. Gamma Prime ( $\gamma'$ )
3. Carbides:

Carbon, added at levels of about 0.05-0.2% combines with reactive refractory elements such as Ti, Ta, Hf to form MC carbides.

After heat treatment  $M_{23}C_6$  and  $MC_6$  carbides may form. The carbides tend to populate the grain boundaries.

4. Grain Boundary  $\gamma'$

5. Borides:

These occur as infrequent grain boundary particles.

6. TCP-Type Phases: (Topologically close-packed)

e.g.  $\sigma$ ,  $\mu$  or Laves phases.

The most important phase for the superalloys is the  $\gamma'$  phase.

#### 2.2.1 GAMMA-PRIME PHASES ( $\gamma'$ )

The precipitation of FCC  $A_3B$  compounds,  $\gamma'$ , in superalloys is a most fortunate event. The Nickel atom is incompressible owing to its 3d electron state. Thus a high Nickel matrix favours precipitation of  $\gamma'$ , which requires little size change.

In the  $\gamma'$  type  $A_3B$  phases, the relatively electronegative element such as Ni composes the A, and the more electropositive elements, such as Al, Ti, Ta or Nb, compose the B elements.

$\gamma'$  is a unique intermetallic phase. It contributes remarkable strengthening by dislocation interaction, by-passing or particle-cutting to the  $\gamma$  -  $\gamma'$  alloy. More remarkably, the strength of  $\gamma'$  increases as temperature increases. Furthermore, the inherent ductility of  $\gamma'$  prevents it from being a source of fracture.

In recent years attention has been paid to the potential of the  $\gamma'$ -phase  $Ni_3Al$ , as a base for superalloy development.

### 2.2.2 $Ni_3Al$ ( $\gamma'$ ) IN Ni-Al-X ALLOYS

$Ni_3Al$ , which is the so-called  $\gamma'$  phase in Ni-based superalloys, has a  $Cu_3Au$  ( $L1_2$ ) structure. The structure is shown in Figure 2.1. A great deal of interest has been shown in  $Ni_3Al$  because of a substantial increase in flow stress with increasing temperature. The strength increases with increasing temperature upto a peak value (4,5). This behaviour is represented in Figure 2.2. In most of the Ni-base superalloys the major contribution to the retention of strength at elevated temperatures is provided by this anomalous behaviour of

In the  $\gamma'$  type  $A_3B$  phases, the relatively electron-negative element such as Ni composes the A, and the more electropositive elements, such as Al, Ti, Ta or Nb, compose the B elements.

$\gamma'$  is a unique intermetallic phase. It contributes remarkable strengthening by dislocation interaction, by-passing or particle-cutting to the  $\gamma$ - $\gamma'$  alloy. More remarkably, the strength of  $\gamma'$  increases as temperature increases. Furthermore, the inherent ductility of  $\gamma'$  prevents it from being a source of fracture.

In recent years attention has been paid to the potential of the  $\gamma'$ -phase  $Ni_3Al$ , as a base for superalloy development.

### 2.2.2 $Ni_3Al$ ( $\gamma'$ ) IN Ni-Al-X ALLOYS

$Ni_3Al$ , which is the so-called  $\gamma'$  phase in Ni-based superalloys, has a  $Cu_3Au$  ( $L1_2$ ) structure. The structure is shown in Figure 2.1. A great deal of interest has been shown in  $Ni_3Al$  because of a substantial increase in flow stress with increasing temperature. The strength increases with increasing temperature upto a peak value (4,5). This behaviour is represented in Figure 2.2. In most of the Ni-base superalloys the major contribution to the retention of strength at elevated temperatures is provided by this anomalous behaviour of

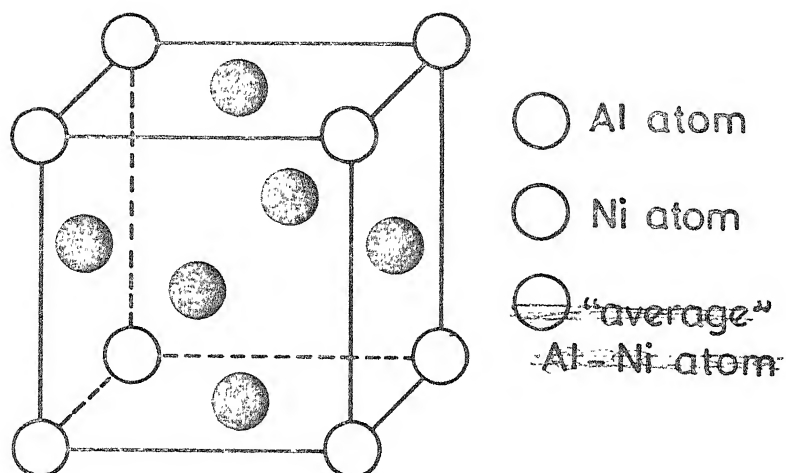


Fig.2.1 The  $L1_2$  structure.

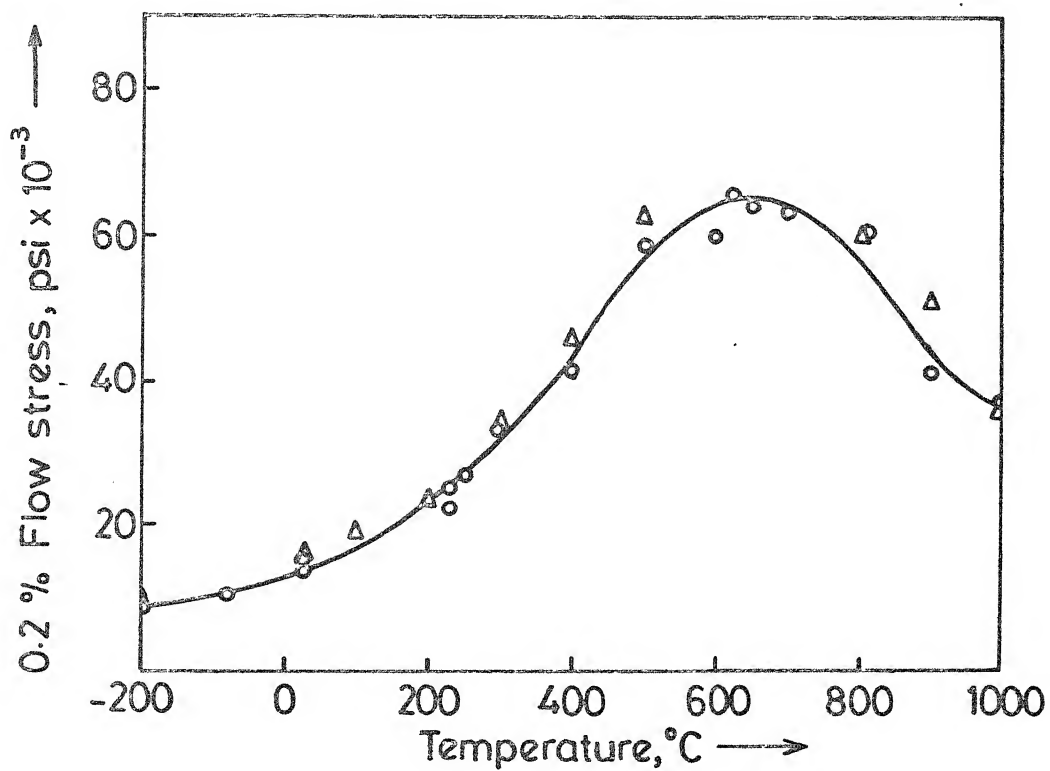


Fig.2.2 Anomalous behaviour of  $\text{Ni}_3\text{Al}$ .

$\text{Ni}_3\text{Al}$ .

The effect of ternary additions on the mechanical properties of  $\text{Ni}_3\text{Al}$  has attracted much attention (5,6,7). This is because  $\text{Ni}_3\text{Al}$  can accommodate fairly substantial amount of ternary additions into solution, and thus a number of alloying elements is partitioned in  $\gamma'$  in commercial alloys (4,8). Moreover, it has been shown (9,10) that the anomalous mechanical response of  $\text{L1}_2$  compounds is systematically affected by the phase stability which can be varied by partial substitution of any one of the components.

The alloying behaviour of  $\text{Ni}_3\text{Al}$ , i.e. whether the addition substitutes exclusively for Al or exclusively for Ni, or for both sites, was first given by Gaurd and Westbrook (4). Knowledge of the direction of the solubility lobe of  $\text{Ni}_3\text{Al}$  in the ternary diagram and information on the extracted and analysed  $\gamma'$  are crucial to understanding of the controlling factors in alloying behaviour.

It has been established (10,11) that Ta and other refractory metals like Ti, Hf, Nb substitute for Al in the  $\text{Ni}_3\text{Al}$  phase.

The progressive improvement obtained over the past 40 years in the ability of turbine blades to withstand high temperatures has been achieved to a large extent by a gradual increase in the volume fraction of

the hardening phase  $\gamma'$  in Ni-base superalloys, together with processing innovations such as columnar grain and single-crystal casting. The trend has been retarded by the associated rise in  $\gamma'$  solvus and the concomitant decrease in the solidus temperature, rapidly leading to the appearance of eutectic  $\gamma'$ .

In order to counteract this tendency, there has been a shift in composition; many recent high temperature performance turbine blade alloys are largely based on the Ni-Al-Ta system. The use of Ta, in preference to Ti or Nb, leads to higher solidus temperatures and enables larger  $\gamma'$  volume fractions to be obtained (12).

### 2.2.3 THE Ni-Al-Ta SYSTEM

In spite of its practical importance, the Ni-Al-Ta system has been relatively little investigated. Nash and West (11) studied the solid state phase equilibria at 1000°C and 1250°C in the region containing 50-100 atomic % Ni. Willemin et al (12) confirmed overall form of the 1250°C isothermal section determined by Nash and West, and have enabled the phase boundaries to be determined more accurately.

## 2.3 BINARY SYSTEMS

### 2.3.1 Ni-Al SYSTEM

Willemin et al (12), in a recent review of the Ni-Al system, have accepted the version of the binary

system given by Hansen and Anderko (13) to be proper. The phase diagram for the Ni-Al binary system, shown in Figure 2.3, is largely based on X-ray analysis of slowly cooled powder, thermal and micrographic analysis.

The partial phase diagram for alloys with 0-50 at % Ni, is well established. There are two intermediate, peritectically formed phases: (i)  $\text{NiAl}_3$  (42.03 wt% Ni or at % Ni) forms peritectically at  $854^\circ\text{C}$  and (ii) the intermediate phase  $\text{Ni}_2\text{Al}_3$  also forms peritectically at  $1133^\circ\text{C}$  and was finally accepted to be of ideal composition (59.19 wt % Ni or 40.0 at % Ni). The  $\beta'$  phase, based on the composition  $\text{NiAl}$  (68.51 wt % Ni or 50.0 at % Ni) has a maximum melting point of  $1638^\circ\text{C}$ .  $\text{NiAl}_3$  has an orthorhombic structure of the  $\text{TiAl}_3$  ( $\text{DO}_{22}$ ) type,  $\text{NiAl}$  is bcc of B2 type and  $\text{Ni}_2\text{Al}_3$  is hexagonal  $\text{D}_{5_{13}}$  type.

The constitution in the 50-100 at % Ni range of composition has proved to be more complicated and has been subjected to numerous investigations. The phase diagram depicted in Fig. 2.3 incorporates both a eutectic and a peritectic reaction close together in the region of  $\text{Ni}_3\text{Al}$ . After some initial debate, these were found to be situated on the Ni-rich side of  $\gamma'$  following experiments carried out by Floyd (14).

$\text{Ni}_3\text{Al}$ , according to Hansen and Anderko (13) has an FCC structure of the  $\text{Cu}_3\text{Au}$  type ( $\text{L}_{12}$ ) with lattice parameter  $a = 3.589 \text{ \AA}$  at 75 at % Ni.



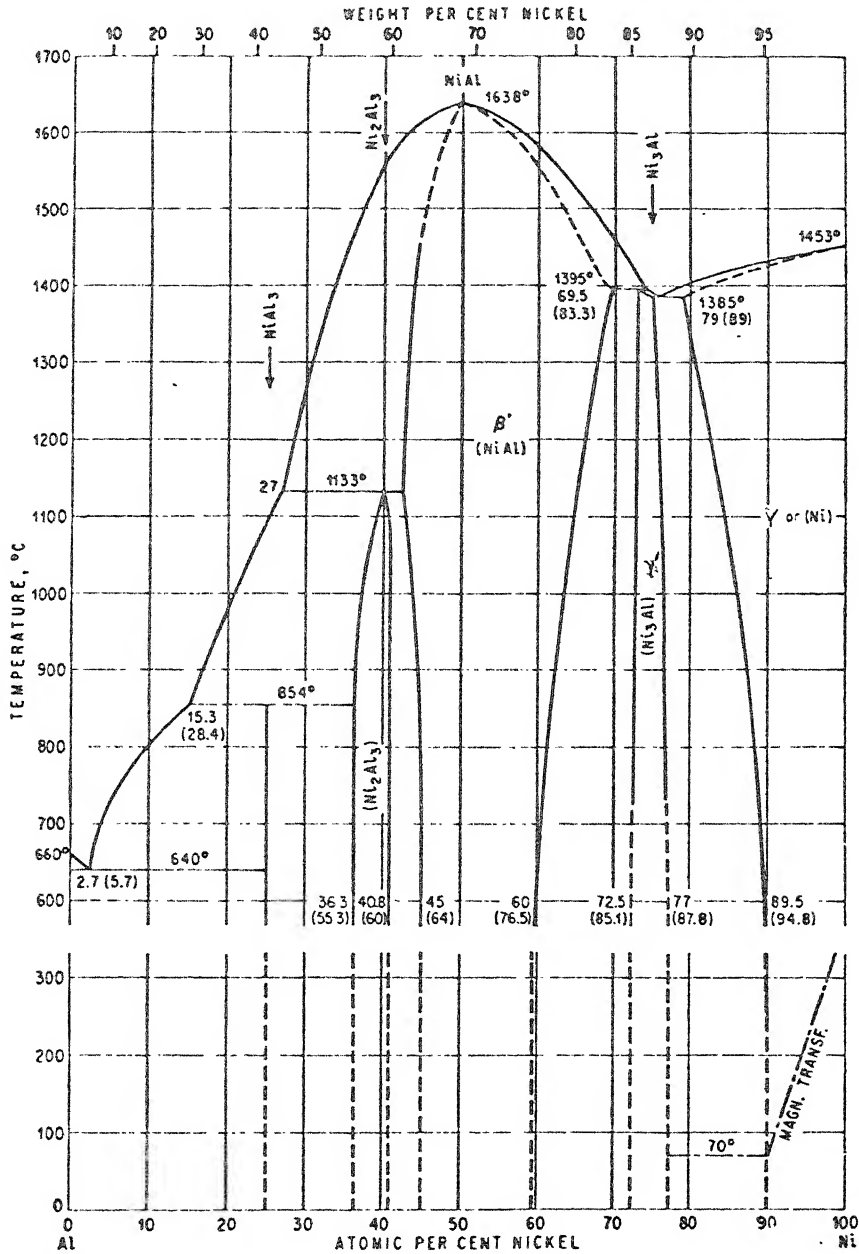


Fig. 2.3 : Al-Ni Binary Phase Diagram

Electrical resistivity and thermal dilation measurements exhibit sharp minima at the compositions NiAl and Ni<sub>3</sub>Al, at constant temperature (13). From the dilation data it is suggested (13) that Ni<sub>3</sub>Al undergoes a solid state transformation at 600°C.

Gaurd and Westbrook (15) in a study of the third-element effect on Ni<sub>3</sub>Al show that Ni<sub>3</sub>Al does not order at elevated temperatures. They also state that at 1150°C, Ni<sub>3</sub>Al is stable over the range 72-78.5 a/o Ni. At the stoichiometric composition the cubic parameter is 3.5700 Å (15,16).

### 2.3.2 Ni-Ta SYSTEM

The binary Ni-Ta system consists of five compounds (Ni<sub>8</sub>Ta, Ni<sub>3</sub>Ta, Ni<sub>2</sub>Ta, NiTa and NiTa<sub>2</sub>) and the two terminal solid solutions, (Ni) and (Ta).

Ni<sub>8</sub>Ta, at a composition of 11.1 at % Ta, was first reported by Larson et al (18,19) and was later confirmed by Nash and West (20). Nash and West determined the peritectoid temperature for the formation of Ni<sub>8</sub>Ta to be between 1320°C and 1340°C. The structure of Ni<sub>8</sub>Ta was investigated using electron diffraction, X-ray diffraction and electrical resistivity techniques. It was found that Ni<sub>8</sub>Ta is a long-range ordered stoichiometric compound with fct structure, isomorphous with NbNi<sub>8</sub>.

$\text{Ni}_3\text{Ta}$  was first discovered by Therkelsen (21) and later was confirmed by numerous workers (17). It melts congruently at  $1550^\circ\text{C}$ . Three distinct structural modifications of  $\text{Ni}_3\text{Ta}$  have been reported to form under different conditions. One form is orthorhombic, of the structure type  $\text{TiCu}_3$  ( $\text{DO}_a$ ) and is stabilized due to surface contamination. It may also be written as  $\text{Ni}_3\text{TaO}_x$ . Heavy cold work produces the tetragonal  $\text{TiAl}_3$  ( $\text{DO}_{22}$ )-type structure. Both the orthorhombic and tetragonal  $\text{Ni}_3\text{Ta}$  are metastable. Giessen and Grant (22) were the first to identify the equilibrium form of  $\text{Ni}_3\text{Ta}$ . They identified the crystal structure as monoclinic of type  $\text{TaPt}_3$  with 12-layer stacking period.

$\text{Ni}_2\text{Ta}$  has been reported to form peritectically at  $1420^\circ\text{C}$  at 33.3 at % Ta (17). There are also reports of it forming at 36.0 at % Ta and  $1320^\circ\text{C}$  from a eutectic reaction.  $\text{Ni}_2\text{Ta}$  has a tetragonal structure, isotypic with  $\text{Cr}_2\text{Al}$ , which is a variation of the type  $\text{MoSi}_2$ .

$\text{NiTa}$  was obtained at 50.0 at % Ta from a peritectic reaction at  $1570^\circ\text{C}$ . The structure of  $\text{NiTa}$  was found to be of  $\text{W}_6\text{Fe}_7$  type with lattice parameters  $a = 0.4921 \text{ nm}$  and  $c = 2.6905 \text{ nm}$ .

$\text{NiTa}_2$  has been reported (17) to form at  $1788^\circ\text{C}$  from a peritectic reaction. It has been indexed on the basis of a bct lattice and has been found to have the structure of  $\text{NiTa}_2$ , with lattice parameters,  $a = 0.6216 \text{ nm}$ ,  $c = 0.4872 \text{ nm}$ .

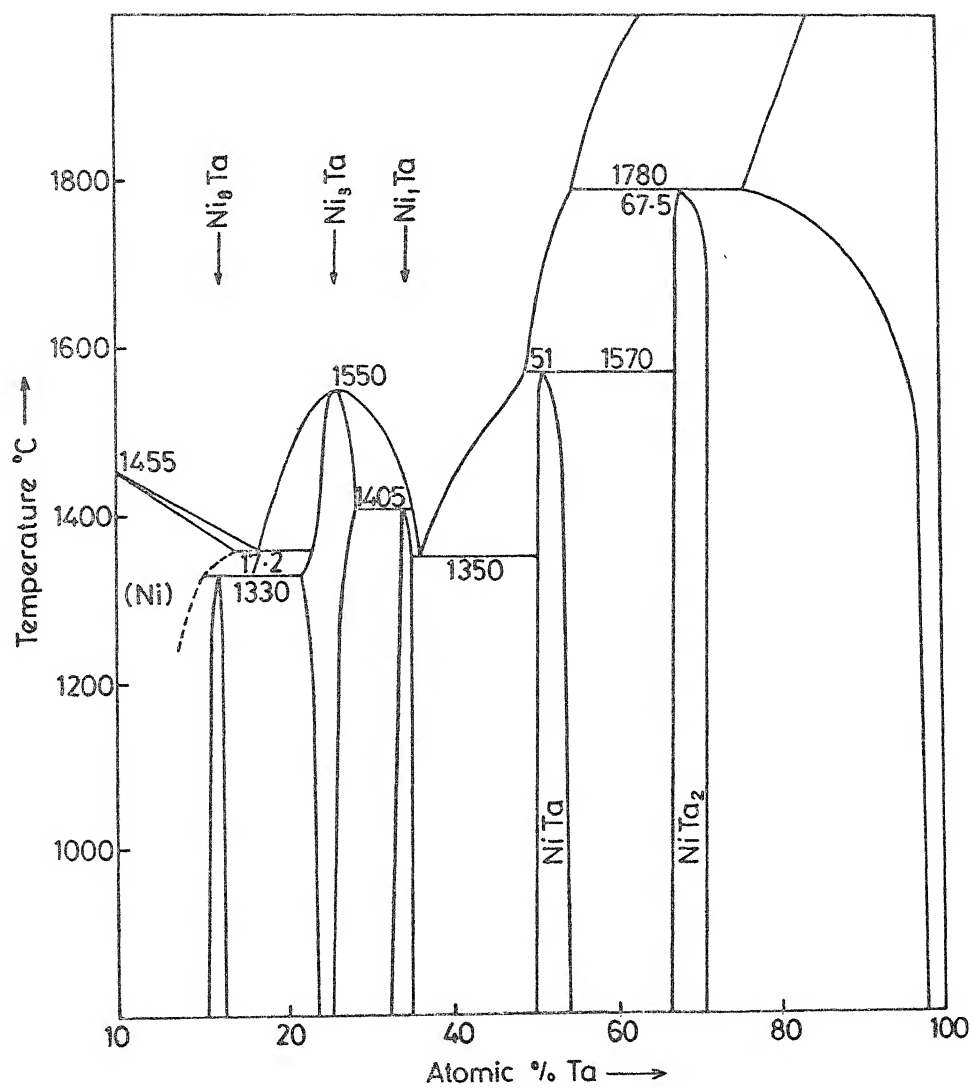


Fig. 2.4 Ni-Ta binary phase diagram.

In a recent review A. Nash and P. Nash (17) have critically reviewed the existing data and phase diagram of the Ni-Ta system. The assessed phase diagram is shown in Figure 2.4.

### 2.3.3 Al-Ta SYSTEM

Not much literature is available on this binary system. The phase diagram, also, is only partially developed. Figure 2.5 shows the binary phase diagram of the Al-Ta system, as given by Massalski (24).

Hansen and Anderko (13) reported the existence of the compound  $\text{TaAl}_3$  (69.09 wt % Ta or 25.0 at % Ta). Its structure was found to be isotypic with  $\text{TiAl}_3$  ( $\text{DO}_{22}$ ) with the lattice parameters  $a = 5.433 \text{ \AA}$ ,  $c = 8.553 \text{ \AA}$ ,  $c/a = 1.574$ .

Elliott (16) reported the existence of  $\text{TaAl}_3$ ,  $\text{TaAl}_2$  and a phase of wide homogeneity, 64.80 a/o Ta. Edshammar et al (25) gave the phase the nominal composition  $\text{Ta}_2\text{Al}$ . The phase was found to be tetragonal with lattice parameters:  $a = 9.825 \text{ \AA}$ ,  $c = 5.23 \text{ \AA}$  at 67 a/o Ta and  $a = 9.98 \text{ \AA}$ ,  $c = 5.16 \text{ \AA}$  at 75 a/o Ta.  $\text{TaAl}_2$  was reported to have a "low symmetry" with a structure similar to  $\text{ZrAl}_3$  and  $\text{ZrSi}_2$ .

Al-Ta Phase Diagram

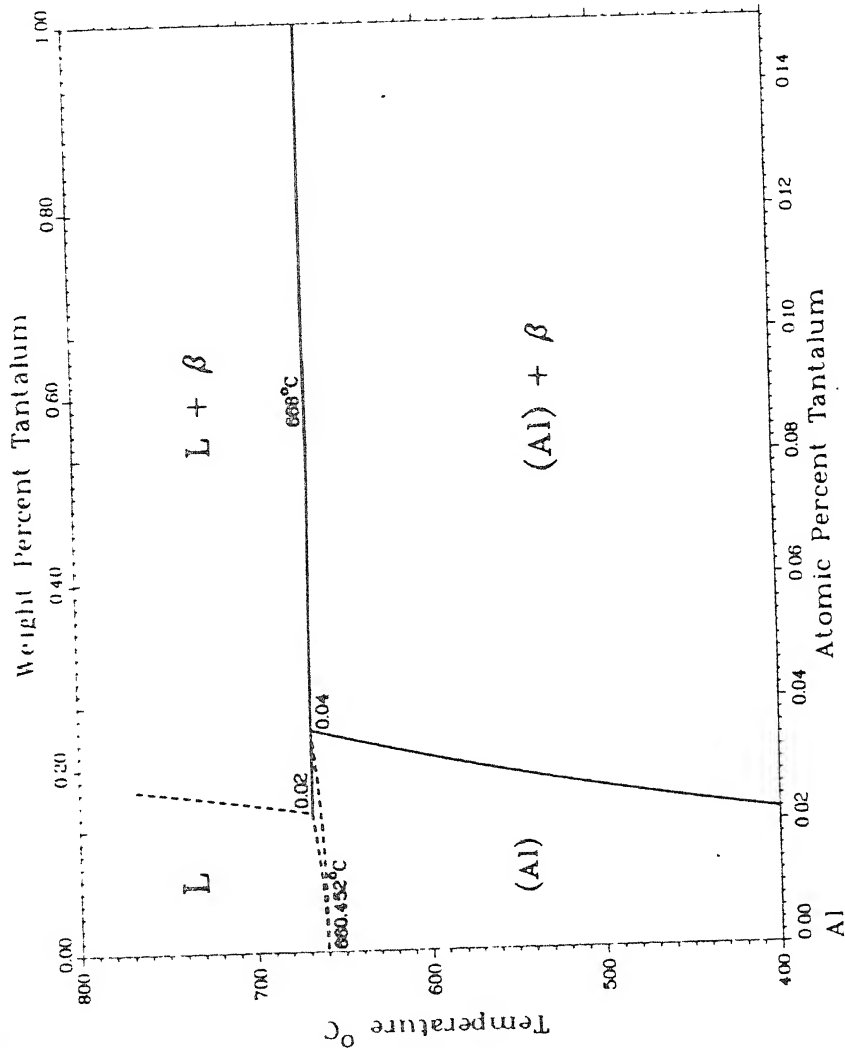


Fig. 2.5 : Al-Ta Binary Phase Diagram

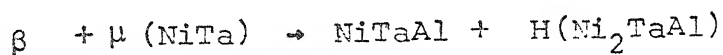
Shunk (23) reported that  $\text{TaAl}_3$  and  $\text{Ta}_2\text{Al}$  are formed peritectically; incipient melting of the stoichiometric alloys was observed at  $1500 \pm 5^\circ\text{C}$  and  $2100 \pm 5^\circ\text{C}$  respectively. Shunk also reported the existence of a high temperature phase  $\text{Ta}_{17}\text{Al}_{12}$  which is a BCC,  $\alpha$ -Mn type with  $a = 9.88 \text{ \AA}$ . A phase which was tentatively indexed as cubic with  $a = 19.2 \text{ \AA}$ , having composition between  $\text{TaAl}_2$  and  $\text{TaAl}_3$  was also observed.

## 2.4 Ni-Al-Ta TERNARY SYSTEM

One of the earliest investigations in the Ni-Al-Ta system was carried out by Hubert et al (26). They reported that  $\gamma'$  ( $\text{Ni}_3\text{Al}$ ) and  $\delta$  ( $\text{Ni}_3\text{Ta}$ ) formed a pseudo-binary eutectic analogous to that in the Ni-Al-Nb system. Mollard et al (27) confirmed this and reported a ternary eutectic between  $\gamma$ ,  $\gamma'$  and  $\delta$  at 79.5 Ni, 11.0 Ta - 9.5 Al (at %). However, the Ni-Al-Nb system differs from the Ni-Al-Ta system in that a ternary compound  $\text{Ni}_6\text{TaAl}$  (designated  $\eta$ ) was found in the  $\text{Ni}_3\text{Al}$ - $\text{Ni}_3\text{Ta}$  section (28,29). This ternary compound has a hexagonal structure ( $\text{Ni}_3\text{Ti}$  type) and melts congruently at 1800K ( $1527^\circ\text{C}$ ).

A partial isothermal section has been determined at 1273K ( $1000^\circ\text{C}$ ) for the range 0-50 at % Ni (30). Other ternary compounds have also been found. Among these  $\text{NiAlTa}$  has hexagonal ( $\text{Mg Zn}_2$  type) structure while  $\text{Ni}_2\text{TaAl}$  (designated H phase) has a cubic  $\text{Cu}_2\text{MnAl}$  type structure.

The work of Nash and West (11) established the isothermal sections at 1523K (1250°C) and 1273K (1000°C) in the 50-100 at % Ni range shown in Figure 2.6. The intermediate phases  $\gamma'$ ,  $\beta$ , and  $\text{Ni}_8\text{Ta}$  were found to show substantial ranges of solid solubility within the ternary system. At 1523K  $\gamma'$  dissolves about 10 at % Ta,  $\beta$  7 at % Ta and  $\text{Ni}_8\text{Ta}$  5 at % T. . The ternary phase  $\text{Ni}_6\text{TaAl}$  shows extensive solid solubility for Ni and enters into equilibrium with  $\gamma'$ ,  $\gamma$ ,  $\beta$ ,  $\delta$  and  $\text{Ni}_8\text{Ta}$ . A peritectoid reaction was reported at a temperature between 1273K and 1523K (1000°C and 1250°C), i.e.



The H phase enters into equilibrium with  $\text{NiAl}(\beta)$ ,  $\text{NiTaAl}$  and  $\text{NiTa}$  and  $\text{Ni}_3\text{Ta}$ .

Willemin et al (12) carried out a more detailed study of the system (12,31). Studying the solid-liquid equilibria, they identified five different phases within the triangle Ni-NiAl -  $\text{Ni}_3\text{Ta}$  :  $\gamma$ ,  $\gamma'$ ,  $\delta$ ,  $\beta$  and  $\text{Ni}_5\text{TaAl}$ , which has been designated as  $\pi$ . The crystal structure and lattice parameters are given in Table 2.1 (12).

The  $\delta$  phase dissolves very little Al, while the solubility of Ta in the  $\beta$  phase is also small. On the contrary,  $\gamma$ ,  $\gamma'$  and  $\pi$  phases have considerable solid solubility ranges.



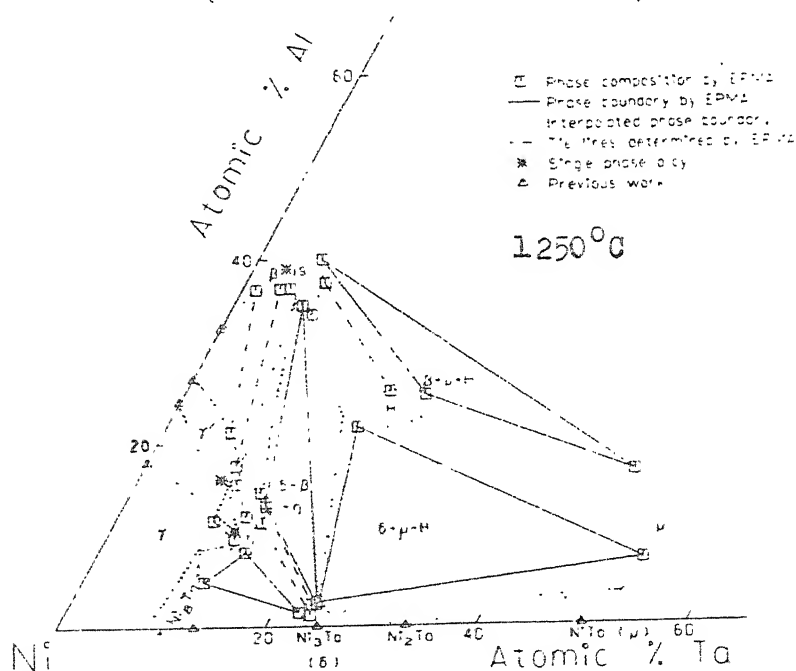


Fig. 2.6 Isotherm of the Ni-Al-Ta System

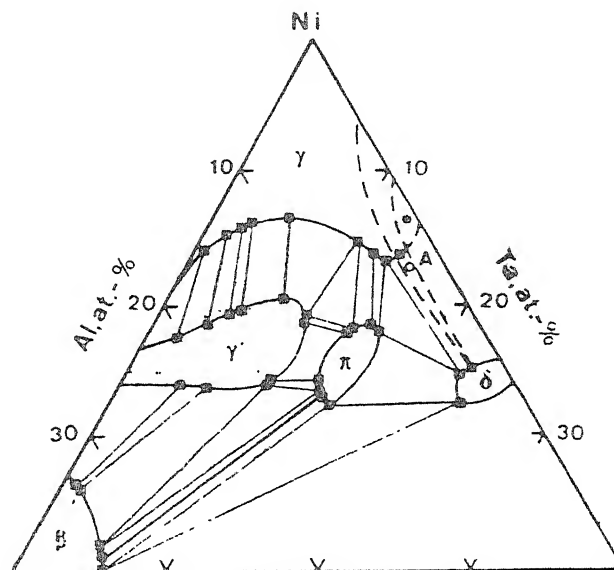


Fig. 2.7 Isotherm of Ni-Al-Ta System at 1250°C.

Willemin et al (12) determined the tie lines for the solid state equilibria by microprobe analysis for the 1250°C isothermal section. Several two-phase fields made up this part of the diagram, as shown in Figure 2.7.

Information on the  $\gamma'$  solvus in Figure 2.7 was obtained from two sources. The temperature at which  $\gamma'$  precipitates or is completely solutioned, and, for a given temperature the limiting compositions of alloys in the  $\gamma + \gamma'$  two phase fields.

The limiting compositions of phases, corresponding to maximum solubility for primary phases are given in Table 2.2 (12).

The presence of  $\pi$ -phase, which had been reported by several workers (11,28), was shown (12) to melt congruently  $\sim 1400^\circ\text{C}$ .

The work by Willemin et al (12) confirmed the 1250°C isothermal obtained by Nash and West (11), with certain modifications.

## 2.5 EFFECT OF BORON ON $\text{Ni}_3\text{Al}$

### 2.5.1 SOLUBILITY, SEGREGATION CHARACTERISTICS, AND EFFECT ON LATTICE PROPERTIES

Though there are reports in the literature on the solubility of Boron in  $\text{Ni}_3\text{Al}$ , and on effect of Boron on the phase stability of  $\text{Ni}_3\text{Al}$ , no report could be found on the effect of Boron on the lattice properties and phase stability of Ni-Al-Ta alloys.

Table 2.1

Crystal Structures and Lattice Parameters (nm) of  $A_3B$  Systems in Ni-Al-Ta System

| Composition |      | Ni <sub>3</sub> Al | Ni <sub>6</sub> TaAl   | Ni <sub>3</sub> Ta                          | Ni <sub>3</sub> Ta                 | Ni <sub>3</sub> Ta                 | Ni <sub>8</sub>  |
|-------------|------|--------------------|------------------------|---|------------------------------------|------------------------------------|------------------|
|             |      | Phase type:        |                        |   |                                    |                                    |                  |
|             |      | Cu <sub>3</sub> Au | Ni <sub>3</sub> Ti     | Al <sub>3</sub> Ti                          | Pt <sub>3</sub> Nb                 | Cu <sub>3</sub> π                  | βCu <sub>3</sub> |
| at %        |      | Bravais Lattice:   |                        |   |                                    |                                    |                  |
| Al          | Ta   | Simple Cubic       | Hexagonal              | BCT   | Monoclinic                         | Ortho-rhombic                      | F.C              |
| 31.0        | 0    | a=0.3573           |                        |   |                                    |                                    |                  |
| 12.6        | 11.8 | a=0.3607           |                        |   |                                    |                                    |                  |
| 13.1        | 8.9  | a=0.3608           |                        |   |                                    |                                    |                  |
| 18          | 7    | a=0.3609           |                        |   |                                    |                                    |                  |
| 10.5        | 12   | .....              | { a=0.5114<br>c=0.8360 |   |                                    |                                    |                  |
| 10.4        | 14.3 | .....              | { a=0.5114<br>c=0.8362 |   |                                    |                                    |                  |
| 12.5        | 12.5 | .....              | { a=0.5112<br>c=0.8340 |   |                                    |                                    |                  |
| 12.5        | 12.5 | .....              | { a=0.5137<br>c=0.8366 |   |                                    |                                    |                  |
| 0           | 25   | .....              | { a=0.3627<br>c=0.7455 | { a=0.512<br>b=0.452<br>c=2.537<br>α=90°50' | { a=0.512<br>b=0.423<br>c=0.452    |                                    |                  |
| 0           | 25   | .....              |                        | { a=0.511<br>b=0.454<br>c=2.550<br>α=90°38' | { a=0.5114<br>b=0.4250<br>c=0.4542 |                                    |                  |
| 2.5         | 26   | .....              | { a=0.3571<br>c=0.7452 |   |                                    | { a=0.5117<br>b=0.4247<br>c=0.4527 |                  |
| 0           | 11.1 | .....              |                        |   |                                    |                                    | { a=1<br>c=0     |

Table 2.2

Limiting Compositions of Phase, Corresponding to Maximum Solubility For Primary Phases

| Phases                 | COMPOSITIONS |           | at %   |
|------------------------|--------------|-----------|--------|
|                        | Al           | Ta        | Ni     |
| $\pi$                  | 8-12         | 13.5-14.5 | 70-80  |
| $\delta$               | 0-2.5        | 23.5-25   | 70-85  |
| $\beta$                | 30-55        | 0-6       | 42-70  |
| $\gamma'$              | 7-25         | 0-10      | 75-80  |
| $\gamma$               | 0-15         | 0-15      | 80-100 |
| $\text{Ni}_8\text{Ta}$ | 0-4          | 12-14     | 84-88  |

Liu and Koch (32) estimated the solubility of Boron in  $\text{Ni}_3\text{Al}$  to be roughly  $0.3 \pm 0.05$  wt%. Beyond that level second phase particles with composition  $\text{Ni}_{20}\text{Al}_3\text{B}_6$  were observed. Studies revealed that while Al content has no observable effect on the segregation of carbon, oxygen and sulfur, the segregation of Boron to grain boundaries is effected by bulk the Al-concentration. As the bulk Al content decreases, the Boron segregated to the grain boundary increases and the grain boundary Al decreases significantly. It was also observed that Boron has a strong tendency to segregate to grain boundaries, but not to cavities or free surfaces. On the other hand, sulfur and other embrittling impurities tended to segregate more strongly to cavity surfaces than to grain boundaries.

Effect of Boron on the lattice properties of  $\text{Ni}_3\text{Al}$  and its alloys has been investigated by several authors (35-37). Kim et al (35) found that the lattice parameters of  $\text{Ni}_3\text{Al}$  increased with increasing Boron content under a constant heat treatment. They also found that lattice parameters varied with heat treatment, indicating that some Boron dissolves in the matrix as a solid solution element.

Baker et al (36) found that Boron is soluble as an interstitial upto at least 1.12 at % and produces a lattice strain of 0.13. They found the strengthening effect of Boron to be 387 MPa per at % Boron.

The large change in strength per fractional change in lattice parameter, due to Boron, compared to other B sub-group elements suggests that Boron produces an asymmetric strain field. This is possible if some Boron atoms occupy interstitial sites on the  $\text{Ni}_3\text{Al}$  unit cell edge. Line broadening in the Debye-Scherrer patterns reported by Weeks et al (38) are consistent with this suggestion.

#### 2.5.2 IMPROVEMENT OF DUCTILITY

Copley and Kear (39) showed that a single crystal of the  $\text{L1}_2$  type intermetallic compound  $\text{Ni}_3\text{Al}$  keeps its strength high upto about 1000K without any appreciable loss in its ductility. However, the use of polycrystalline  $\text{Ni}_3\text{Al}$  as a practical high temperature material has been prevented by its severe grain-boundary brittleness. It has been reported that localized flow accompanies the intergranular fracture of  $\text{Ni}_3\text{Al}$  (40).

Aoki and Izumi (41,42) first reported the beneficial effect of Boron in  $\text{Ni}_3\text{Al}$  and observed tensile ductility at room temperature. Liu and Koch (51), by control of Boron concentration and thermomechanical treatment reported a tensile elongation of 50%.

Although the improvement of ductility of polycrystalline  $\text{Ni}_3\text{Al}$  by addition of small amount of B has been extensively reported ever since 1971 (41), the real reason for this ductility improvement is still not exactly known.

The nature and amount of plastic deformation, reported by Schulson et al (40), is important in understanding the mechanical aspects of grain boundary brittleness. Ogura and coworkers (33) examined the chemistry of grain boundaries and the plasticity associated with the intergranular fracture of  $\text{Ni}_3\text{Al}$ . They inferred that the cohesive strength of grain boundaries in  $\text{Ni}_3\text{Al}$  is very sensitive to the change in atomic structure of grain boundaries. Polycrystalline  $\text{Ni}_3\text{Al}$  obtained by recrystallization of rolled single crystals was shown to have remarkable resistivity against intergranular cracking. Hence they concluded that Boron improved the ductility in  $\text{Ni}_3\text{Al}$  possibly by modifying the weak nature of atomic bonds (or structure) in grain boundaries. Messmer and Briant (34) showed by quantum mechanical calculations that boron acts as a cohesive enhancer in Nickel. With this result they tried to explain the improvement of ductility of  $\text{Ni}_3\text{Al}$  by Boron addition.

## 2.6 MECHANICAL PROPERTIES OF $\text{Ni}_3\text{Al}$ AND THE EFFECT OF ALLOYING ADDITIONS

After Westbrook (43) showed in 1957, for the first time, that  $\text{Ni}_3\text{Al}$  has an anomalous temperature dependence of hardness, enormous amount of work has been done by numerous workers (5,31, 43-46) to substantiate this fact and to find out the mechanism behind this anomalous behaviour. Davies and Stoloff (5) showed that the flow stress increases by seven folds between  $-196^\circ\text{C}$  and a maximum at  $\sim 600^\circ\text{C}$ .



Over the years, the following mechanisms had been proposed to explain the anomalous behaviour of  $\text{Ni}_3\text{Al}$ :

- (i) Diffusion Mechanism
- (ii) Intrinsic Effects
- (iii) The Cross-slip model.

Pope and Ezz (46), in a recent review, have discussed these mechanisms in great detail.

#### 2.6.1 EFFECT OF ALLOYING ADDITION AND SOLUTION STRENGTHENING

The alloying behaviour of  $\text{Ni}_3\text{Al}$ , i.e., whether the addition substitutes exclusively for Al or exclusively for Ni, or for both sites, was first given by Gaurd and Westbrook (4). They divided the elements which dissolve substitutionally in  $\text{Ni}_3\text{Al}$  into three groups:

- i) Those which substitute for Ni - Co and Cu.
- ii) Those which substitute for Al - Si, Ti, Mn, V etc.
- iii) Those which substitute for both the constituent elements - Fe, Cr and Mo.

Gaurd and Westbrook (4) suggested that the substitution behaviour is determined by electronic (chemical) factors rather than atomic size factors.

Recently, Ochiai et al (52) and Mishima et al (53,54) have reported quite extensively on the effect of ternary additions on the mechanical properties of  $\text{Ni}_3\text{Al}$  (52, 53) and on solid solution hardening of  $\text{Ni}_3\text{Al}$  (54).

It was concluded that solid solution hardening in ternary compound cannot be fully interpreted even by the combined effect of "atomic size effect" and "modulus effect" (54). Though Mishima et al (54) gave original evidence of solution hardening being governed by the elastic interaction involving edge dislocations, they did not give any explanation for the behaviour of transition metal elements. Rawlings and Staton-Bevan (6) and Aoki and Izumi (55) investigating the effects of additions to polycrystalline  $\text{Ni}_3\text{Al}$ , came to the same conclusions.

Wee and co-workers (56,57) have proposed what is so far the most comprehensive model of solid solution strengthening effects in  $\text{L1}_2$  ordered alloys. They pointed out that other ordered structures can be produced from  $\text{L1}_2$  structure by introducing periodic faults on (111) or (010) planes. For example,  $\text{DO}_{22}$  structure results from introducing a periodic array of APBs on (010) planes. Since APB energy is anisotropic and also dependent on structure, hence the anomalous increase in flow stress in  $\text{L1}_2$  alloys depends on the difference in APB energy on (010) and (111) planes. An element which increases this difference, also increases the anomalous increase of CRSS with temperature. This theory works very well for additions which make the  $\text{L1}_2$  structure unstable relative to  $\text{DO}_{22}$  e.g. Ta and Nb, but less well for those which make it unstable relative to  $\text{DO}_{19}$ , e.g. Ti and Fe.

## 2.7 STATEMENT OF PROBLEM

Full potential of an alloy system can be exploited only when its phase diagram has been properly established and understood. For practical applications of an alloy system, its mechanical properties are of prime importance. But, for the mechanical properties to be predicted and to be reproduced with consistency, knowledge about the phase diagram of the system is essential.

Ternary alloys of Ni-Al-Ta system have excellent mechanical properties and are useful for many practical applications, particularly in the composition range near the  $\gamma'$  region (i.e., the solubility to be of  $\text{Ni}_3\text{Al}$ ). Small addition of Boron (of the order of even  $10^2$  ppm) has been reported to give remarkable improvement in the ductility of the otherwise brittle intermetallic  $\text{Ni}_3\text{Al}$  and its superalloys. However, the review of literature shows that the solubility lobe of  $\text{Ni}_3\text{Al}$  is established for only two isothermals :  $1250^\circ\text{C}$  and  $1000^\circ\text{C}$ . Moreover, except for two detailed studies of the Ni-Al-Ta system near the  $\gamma'$  region, not much phase stability work has been done on this system.

There is almost no report on the effect of Boron on the stability of the  $\gamma'$  phase, or for that matter, of any phase in the Ni-Al-Ta system. Though the maximum

Solubility of B in  $\text{Ni}_3\text{Al}$  has been determined, its solubility and behaviour in presence of Ta has not been reported.

Hence it was proposed that the stability of the  $\gamma'$  phase in the Ni-Al-Ta system be studied at three temperatures:  $800^\circ\text{C}$ ,  $1000^\circ\text{C}$  and  $1200^\circ\text{C}$ , in presence of Boron. An  $\text{Ni}_3\text{Al}$  master alloy containing about 500 ppm Boron, supplied by the Defence Metallurgical Research Laboratory, Hyderabad, was to be used for preparing the samples.

In order to establish the effect of Boron, comparisons would have to be made with alloys not containing Boron. The properties of non-Boron alloys reported in literature could be used for comparison. But for studying the properties under identical conditions, it was proposed that the non-Boron alloys be also prepared.

# REFERENCES

1. C.T. Sims, "Superalloys: Genesis and Character", Superalloy II, Sims, Stoloff, Hagel (Eds.) John Wiley and Sons, New York, 1987.
2. C.T. Sims and Whagel, "The Superalloys", John Wiley and Sons, New York, 1972.
3. E.W. Ross and C.T. Sims, "Superalloys II", John Wiley and Sons, New York, 1987, p. 97-133.
4. R.W. Guard and J.H. Westbrook, Trans. Metall. Soc. AIME, Vol. 215, 1959, p. 807.
5. R.G. Davis and N.S. Stoloff, Trans. Metall. Soc. AIME, Vol. 233, 1965, p. 714.
6. R.D. Rawlings and A.E. Staton-Bewan, J. Mater. Sci., Vol. 10, 1975, p. 505.
7. P.R. Thornton, R.G. Davis and T.C. Johnson, Met. Trans., Vol. 17, 1976, p. 212.
8. R.F. Decker and J.R. Mihalisin, Trans. Am. Soc. Metals, Vol. 62, 1969, p. 481.
9. T. Suzuki, Y. Oya and D.M. Wee, Acta Metall, Vol. 28, 1980, p. 301.
10. S. Ochiai, Y. Oya and T. Suzuki, Acta Metall, Vol. 32, 1984, p. 289.
11. P. Nash and D.R.F. West, Metal. Sci. J., Vol. 13, 1979, p. 670.
12. P. Willemijn, O. Dugue, M. Durrand, Charre and J.H. Davidson, Mat. Sc. & Tech., Vol. 2, April 1986, p. 314.
13. M. Hansen and K. Anderko, "Constitution of Binary Alloys" (2nd Edition), 1958, McGraw Hill, N.Y.
14. R.W. Floyd, J. Inst. Metals, 1951-52, Vol. 80, pp. 551-553.
15. R.W. Gaurd and J.H. Westbrook, Trans. AIME, Vol. 215, 1959, pp.871-872.
16. Eliot, "Constitution of Binary Alloys - 1st Supplement" 1961, McGraw Hill, N.Y.

17. A. Nash and P. Nash, Bull. of Alloy Phase Diag., Vol. 5, No.3, 1984, pp. 259-265.
18. J.M. Larson, R. Taggart and D.H. Polonis, Metall. Trans, Vol. 1 (1970), pp. 485-489.
19. J.M. Larson, R. Taggart and D.H. Polonis, Mater. Sci. Eng., Vol. 9, No.1, 1972, pp. 31-36.
20. P. Nash and D.R.F. West, Met. Sci., Vol. 17, 1983, pp. 99-100.
21. E. Therkelsen, Met. Alloys, Vol. 4, 1933, pp. 105-108.
22. B.C. Giessen and N.J. Grant, Acta Metall, Vol. 15, No.5, 1967, pp. 871-877.
23. F.A. Shunk, "Constitution of Binary Alloys - 2nd Supplement", McGraw Hill, N.Y.
24. T.B. Massalski, "Binary Alloy Phase Diagrams".
25. L. Edshammar and Holmberg, Acta Chem. Scand, Vol. 14, 1960, pp. 1219-1220.
26. J.C. Hubert, W. Kurz and B. Lux, J. Crystal Growth, Vol. 13/14, 1972, p. 757.
27. F. Hollard, B. Lux and J.C. Hubert, Z. Metallk, Vol. 65, (1974), p. 461.
28. B.C. Giessen and N.J. Grant, Acta Cryst. Vol. 18, 1965, p. 1080.
29. S. Chakraborty and D.R.F. West, Met. Sc. Vol. 18, April 1984, p. 207.
30. C.R. Hunt and A. Raman, Z. Metallk, Vol. 59, 1968, p. 701.
31. P. Willemien, O. Dugue, M. Durrande-Charre and J. Davidson, "Superalloys 1984", Edts. Gell et al, 1984, T.M.S. of AIME, pp. 637-647.
32. C.T. Liu, C.L. White and J.A. Horton, Acta. Metall. Vol. 33, No.2, 1985, pp. 213-229.
33. T. Ogura, S. Hanada, T. Masumoto and O. Izumi, Met. Trans. A, Vol. 16A, March 1985, p. 441.
34. R.P. Messmer and C.L. Briant, Acta Metall, Vol. 30 (1982), p. 457.

35. Y.G. Kim, Gi. W. Yoon, N.S. Stoloff, J. of Mat. Sc. Letters, Vol. 4, 1985, pp. 1407-1408.
36. I. Baker, B. Huang, E.M. Schulson, Acta Metall., Vol. 34, No.3, 1988, pp. 493-499.
37. S.C. Huang, Ai Taub, K.-M.Chang, Acta Metall, Vol.32, 1984, p. 1703.
38. T.P. Weiks, V. Zinoviev, D.V. Viens and E.M.Schulson, Acta. Metall, Vol. 35, 1987, p. 1109.
39. S.M. Copley and B.H. Kear, Trans. Met. Soc. AIME, Vol. 239, 1967, p. 977.
40. E.M. Schulson, D.L. Davidson and D. Viens, Met. Trans. A, Vol. 14A, 1983, p. 1523.
41. K. Aoki and O. Izumi, Nippon Kinzoku Gakkaishi, Vol.41, 1971, p. 170.
42. K. Aoki and O. Izumi, Trans. Japan, Inst. Metals, Vol. 19, 1978, p. 203.
43. J.H. Westbrook, Trans. AIME, Vol. 209, 1957, p. 898.
44. A. Flinn, Trans. Met. Soc. AIME, Vol. 218, 1960, p. 145.
45. P.H. Thornton, R.G. Davies and T.L. Johnson, Met. Trans., Vol. 1, 1970, p. 207.
46. D.P. Pope and S.S. Ezz, Int. Met. Rev., Vol. 29, No.3, 1984, pp. 136-167.
47. T.L. Johnston, A.J. McEvily, and A.S. Tetelman, "High Strength Materials" (eds. V.F. Zackay), 1965, pp. 363-381.
48. B.H. Kear and H.G.F. Wilsdorg, Trans. Met. Soc. AIME, Vol. 224, 1962, p. 382.
49. B.H. Kear and M.F. Hornbecker, Trans. ASM, Vol. 59, 1966, p. 155.
50. B.H. Kear, Acta. Metall., Vol. 12, 1964, p. 555.
51. S. Takeuchi and E. Kuramoto, Acta Metall., Vol. 21, 1973, p. 415.
52. S. Ochiai, Y. Mishima, M. Yodogawa and T. Suzuki, Trans. of Jap. Inst. of Metals, Vol. 27, No. 1, 1986, p. 32.

53. Y. Mishima, S. Ochiai, M. Yodogawa and T. Suzuki, Trans. of Jap. Inst. of Metals, Vol. 27, No. 1 (1986), p. 41.
54. Y. Mishima, S. Ochiai, N. Hamao, M. Yodaga and T. Suzuki, Trans. of Jap. Inst. of Metals, Vol.27, No. 1, 1986, p. 648.
55. K. Aoki, O. Izumi, Phys. Stat. Sol. (a), Vol. 32, 1975, p. 657.
56. D.H. Wee, T. Suzuki, Trans. Japan Inst. of Metals, Vol. 20, 1979, p. 634.
57. D.H. Wee, O. Noguchi, Y. Oya, T. Suzuki, Trans. Japan Inst. of Metals, Vol. 21, 1980, p. 237.



## CHAPTER 3

### EXPERIMENTAL PROCEDURE

#### 3.1 ALLOY PREPARATION

##### 3.1.1 ALLOYS CONTAINING BORON

The starting material for alloys containing Boron was Boron-doped  $\text{Ni}_3\text{Al}$  obtained from the Defence Metallurgical Research Laboratory (DMRL), Hyderabad. No chemical analysis was supplied with the material. The Boron content was known to be about 500 ppm. X-ray diffraction patterns and microstructure for the DMRL supplied material showed it to be single phase.

In order to make an alloy of a certain composition, the DMRL supplied  $\text{Ni}_3\text{Al}$  alloy was used and extra Nickel (or Aluminium) and Tantalum was added as per the requirement.

In calculating the weight of component elements needed for an alloy, the weight of Boron was neglected as it is present in the  $\text{Ni}_3\text{Al}$  in very small quantity (Refer Appendix A)

##### 3.1.2 ALLOYS NOT CONTAINING BORON

The starting materials for alloys not containing Boron were elemental Nickel of 99.99% purity, elemental Aluminium of 99.99% purity, and Ta of 99.9% purity. The weight of each component required for making 15 gm of the alloy was calculated directly from weight percent

composition.

### 3.2 MELTING

The alloys were melted into buttons of 15 gm weight in a non-consumable electrode water-cooled Cu hearth arc melting furnace. A specific furnace charging sequence was used to avoid variation in melting loss. The alloys containing Boron were arranged in such a way that a large flat piece of  $\text{Ni}_3\text{Al}$  remained at the top with Nickel pieces at the bottom and small pieces of Ta sheet allround. In case of non-Boron alloys, Aluminium pieces were kept at the bottom, on top of them were kept Ni-pieces and all were topped with pieces of Ta. All these ingredients were arranged around a large rod of Ni (1.5 cm long, 5 mm in diameter) which was made to stand vertically. Arc was struck on the flat surface of the vertical Ni-rod.

Before striking the arc, the furnace was evacuated and flushed with Argon. The alloy was melted three times. After each melting, the button was inverted and the furnace was evacuated and flushed with Argon. This was done to ensure maximum possible homogenization during melting.

After melting, the buttons were weighed to obtain the weight loss. Next they were cut by a diamond into atleast three parts.

### 3.3 HOMOGENIZATION

The alloys were vacuum sealed in fused silica tube using a rotary pump to obtain a vacuum of the order of  $10^{-2}$  to  $10^{-3}$  torr. Each sealed tube containing three pieces of a sample was put in for homogenization at  $1200^{\circ}\text{C}$ . The furnace was calibrated and maintained within  $\pm 2^{\circ}\text{C}$  of the required temperature.

The time of homogenization was determined by experimenting on a Boron-doped alloy containing 7 atomic % Ta. The sample was quenched from  $1200^{\circ}\text{C}$  after every consecutive 3 days of homogenization. X-ray diffraction pattern was taken for the sample and its lattice parameter was calculated. The homogenization was continued till there was practically no change in the lattice parameter of the alloy. It was found that homogenization was effected after about 12 days. So all the samples were homogenized at  $1200^{\circ}\text{C}$  for 12 days.

In order to reduce the time of anneal for homogenization, attempt was made to homogenize one sample at  $1300^{\circ}\text{C}$ . But after 3 days it was found that the alloy melted partially.

Since homogenization was done at  $1200^{\circ}\text{C}$  within a variation of  $\pm 2^{\circ}\text{C}$ , for the samples whose phase stability was to be studied at  $1200^{\circ}\text{C}$ , no further equilibration was

required. Yet, after the 12 days of homogenization anneal, the samples were not taken out of the furnace, but were kept for another 2 days under the same conditions. This was not absolutely necessary, but was done to ensure complete equilibration at  $1200^{\circ}\text{C}$ . The samples were quenched by letting them fall directly into water.

### 3.4 EQUILIBRIATION AT $1000^{\circ}\text{C}$

One of the 3 pieces of each sample homogenized and equilibrated at  $1200^{\circ}\text{C}$  was taken out for annealing at  $1000^{\circ}\text{C}$ . The piece was vacuum sealed, as before, in a fused silica tube and kept at  $1000^{\circ}\text{C}$  for 12 days. The furnace was maintained at  $1000^{\circ}\text{C}$  with an accuracy of  $\pm 1.5^{\circ}\text{C}$ . The choice of the time (12 days) was based on that reported in the literature\* (7 days) and on our experience during homogenization.

### 3.5. X-RAY DIFFRACTION

#### 3.5.1 SAMPLE PREPARATION

Powder for X-ray diffraction work was prepared by filing a piece of alloy button with hardened steel file. Before filing, the surface of the piece of the alloy was cleaned by grinding on the belt grinder. This was done to ensure the removal of any oxide layer that might have formed on the surface.

\* P. Nash and D.R.F. West, Metal. Sci. J, Vol.13, 1979, p.670.

To make powder for diffraction work, a piece of an alloy was closed in a vice and the edges were filed off. The filings were collected on a piece of paper.

After enough powder had been filed off, the powder was transferred to a fused silica tube. The powder was vacuum sealed in the tube and stress-relieved for about 10 minutes at the temperature of equilibration.

### 3.5.2 THE SAMPLE HOLDER

The X-ray beam coming out of the collimator and falling on the powder was found to have a rectangular cross-section. While the length of the rectangle was fixed, the breadth could be adjusted by changing the X-ray slit width. The rectangular cross-section was measured to be of dimensions 15mm x 4 mm approximately with a slit opening of 1 mm.

Initially, the sample holder was a 25mm x 25 mm square perspex sheet with a rectangular groove (16 mm long, 6 mm wide, 0.5 mm deep) at the center of the sheet. It was found that owing to the fluorescence from the perspex the background intensity increased, especially at low angles of incidence of the X-ray beam. This could be reduced by increasing the area of powder exposed to X-ray and by simultaneously decreasing the area of

perspex exposed to radiation. There were two ways of doing this, either by enlarging the central slit so that more powder could be held, or by removing the excess perspex as much as possible by machining. The former solution would require more powder. Since filing itself was a very tedious process, the second solution was opted for.

Thus in its final shape, the perspex sheet was rectangular piece of perspex with external dimensions 25mm x 10mm. The central groove for holding powder being of the dimension 16mmx6mm. This resulted in a remarkable improvement in the quality of diffraction pattern.

### 3.5.3 X-RAY DIFFRACTION

The X-ray diffraction work was carried out on a Rich Seifert Isodebye flux 2002 diffractometer using Cu target. A curved graphite crystal monochromator attachment at the diffracted beam side of the diffractometer was used to cut down stray radiation reaching the counter as well as to remove reflections. The diffraction pattern was recorded on a strip-chart recorder.

For taking X-ray diffraction pattern, at first a rapid scan was made from  $20^{\circ}$  to  $150^{\circ}$  ( $2\theta$  values) to see the positions of the diffraction peaks. In the second step slow scanning was done near the peaks in order to get more accurate  $2\theta$  values for the peak positions.

Conditions under which the diffraction patterns were obtained are listed below:

PROCEDURE 1:

(RAPID SCAN):

Voltage = 30 kV

Current = 20 mA

Scanning speed =  $3^{\circ}$ /min (in  $2\theta$  values)

Chart speed = 30 mm/min

Time constant = 3 sec.

Counts per minute = 200

X-ray slit opening = 1 mm

PROCEDURE 2:

(SLOW SCAN):

Voltage = 30 kV

Current = 20 mA

Scanning speed =  $0.6^{\circ}$ /min

Chart speed = 15 mm/min

Time constant = 3 sec.

Counts per minute = It was varied to obtain proper peaks height

X-ray slit opening = 1 mm.

In order to know the error in the machine in showing angles, a standard silicon sample was scanned at slow speed (same speed as in the 2nd step mentioned above). The difference between the angles of the peaks recorded on the strip chart recorder and the corresponding

angles known for standard Si sample gave the correction factor. The correction factor, when added to recorded angles for the diffraction peaks of the alloy sample, gave the exact angular positions of the diffraction peaks (i.e., the correct values of  $2\theta$ ). These corrected angles were later used in calculating precise lattice parameters for the alloy.

It was observed that with the scanning speed of  $3^\circ/\text{min}$  (as used in the rapid scan) the weak superlattice reflections of (100) and (110) planes etc. in  $\text{Ni}_3\text{Al}$ , were not detectable. So slower scanning speeds were resorted to. In order to get detectable intensities of the weak diffraction peaks, higher current and voltage ratings were used. The X-ray slit opening was widened to 1.5 mm for the same reason. The conditions set for detecting the superlattice reflection, were;

#### PROCEDURE 3:

Voltage = 40 kV

Current = 30 mA

Scanning speed =  $0.3^\circ/\text{min}$  (in  $2\theta$  values)

Chart speed = 300 mm/hr or 15 mm/min for better resolution

Time = 10 sec

Counts per minute = 200

X-ray slit opening = 1.5 mm.



### 3.6 OPTICAL MICROSCOPY

The samples were etched electrolytically using 10% Oxalic Acid solution. Previous to selecting this etching reagent, Alcoholic Ferric chloride ( $\text{FeCl}_3$  5 gm, HCl 10 ml, Ethanol 100 ml) and Marble's Reagent ( $\text{CuSO}_4$  4 gm, HCl 20 ml,  $\text{H}_2\text{O}$  20 ml) had been tried out. But 10% Oxalic Acid solution was seen to give better results.

For electro-etching the proper time-current combination was found out by starting with low voltage (3V) and inspecting the microstructure after etching for different durations of time, at intervals of 30 seconds. At 3V and 5V hardly any difference occurred in the microstructure even after 10 minutes of etching. Etching action became more rapid at 10V. At 15V changes in the microstructure were clearly visible after about 5 minutes of etching.

All the microstructures showed pits at the grain boundaries. One alloy was taken and polishing was started from the belt grinder. After wheel polishing, the microstructure was seen without etching. Polishing was then repeated from No. 2 emery paper upto the polishing wheel. The idea was to remove the material from the surface and observe the effect on the pit size.

### 3.7 MICROHARDNESS-MEASUREMENTS

Microhardness measurements were made on the grains and across grain-boundaries. A load of 25 gm was used for taking hardness of the matrix.

For the small particles, barely outlined in the microstructure, a weight of 5 gm was used for microhardness measurements.

### 3.8 DIFFERENTIAL SCANNING CALORIMETRY

Differential scanning calorimetry was done on two alloys: Boron-doped  $\text{Ni}_3\text{Al}$  without Ta and Boron-doped  $\text{Ni}_3\text{Al}$  with 1 at %Ta. The details of the runs are given below:

Heating :  $10^\circ\text{C}$  per minutes

Temperature range:  $25^\circ\text{C}$  to  $1240^\circ\text{C}$

Chart speed: 12 cm/hr.

## CHAPTER 4

### RESULTS

For the purpose of studying the phase stability of the Ni-Al-Ta system, with and without Boron condition, the alloys were at first homogenized. Next extensive X-ray diffraction analysis was carried out. Electron microscopy would have formed a very important part of the work, but owing to the unavailability of the equipment, we had to be satisfied with optical microscopy. This was followed by microhardness measurements and Differential Scanning Colorimeter (D.S.C.) runs.

The results that were obtained at the various stages of investigation, are given in the following sections.

#### 4.1 INDEXING OF THE X-RAY DIFFRACTION PATTERNS

The present work required extensive use of X-ray diffraction. But before any analysis can be made of the diffraction pattern, proper indexing has to be done. In other words, the correct Miller indices are to be assigned to the diffraction peaks. The indexing work in the present case was simplified because the crystal structure of  $\text{Ni}_3\text{Al}$  is well established. However, the diffraction pattern of the master alloy ( $\text{Ni}_3\text{Al}$  containing Boron), obtained from the Defence Metallurgical Research Laboratory (DMRL) was

properly indexed and compared with the diffraction pattern of  $\text{Ni}_3\text{Al}$  given in the ASTM data cards. Table 4.1 shows the diffraction pattern of the master alloy in the as obtained condition, before any heat treatment was given to it.

The diffraction pattern of alloys which contained Ta, irrespective of Boron content showed some extra peaks besides those that could be indexed on the basis of  $\text{Ni}_3\text{Al}$ . As an example, the diffraction pattern of an alloy containing 7 atomic % Ta, with Boron, is shown in Table 4.2. The superlattice reflections were very weak. So it was not possible to measure their exact angular positions, accurately.

#### 4.2 METHOD FOR LATTICE PARAMETER MEASUREMENT

In the present work extensive use was made of precise lattice parameters. Lattice parameter was used not only to find the effect of solute addition on  $\text{Ni}_3\text{Al}$ , but also to determine the time required for homogenizing the alloys, to have an idea about the approximate composition of a phase, and to determine the phase boundary. Thus it was necessary to obtain the precise lattice parameter values.

The alloy system used in the present work gave very broad X-ray diffraction peaks at high angles ( $2\theta \leq 100^\circ$ ). Thus low angle diffraction peaks had to be used for lattice parameter calculations.

Table 4.1 : Diffraction Pattern of the Master Alloy  
(Ni<sub>3</sub>Al with B)

| Observed Values |              |                                   |                  | Values from ASTM Data Card |                  |     |
|-----------------|--------------|-----------------------------------|------------------|----------------------------|------------------|-----|
| Line No.        | 2θ           | $d = \frac{\lambda}{2\sin\theta}$ | I/I <sub>0</sub> | d                          | I/I <sub>0</sub> | hkl |
| 1.              | 24.726       | 3.60                              | 30               | 3.600                      | 40               | 100 |
| 2.              | 35.182       | 2.55                              | 20               | 2.547                      | 40               | 110 |
| 3.              | 43.684       | 2.072                             | 100              | 2.074                      | 100              | 111 |
| 4.              | 51.019       | 1.79                              | 75               | 1.799                      | 70               | 200 |
| 5.              | 57.567       | 1.602                             | 30               | 1.603                      | 40               | 210 |
|                 | Not observed |                                   |                  | 1.461                      | 20               | 211 |
| 6.              | 75.231       | 1.263                             | 60               | 1.265                      | 60               | 220 |
| 7.              | 91.087       | 1.080                             | 65               | 1.078                      | 60               | 311 |
| 8.              | 96.660       | 1.032                             | 40               | 1.032                      | 40               | 222 |

Table 4.2 : Indexing of the Diffraction pattern of Alloy  
containing 7 at % Ta and B  
Lattice Parameter of the Alloy =  $3.577 \text{ \AA}$

| Observed Values |             |                                    |         |     |   |
|-----------------|-------------|------------------------------------|---------|-----|---|
| Line<br>No.     | $2\theta$   | $d$<br>$= \lambda / 2 \sin \theta$ | $I/I_0$ | hkl | $d$<br>( $\text{Ni}_3\text{Al}$ )<br>Calculated |
| 1.              | $24.7240^*$ | 3.600                              | 10      | 100 | 3.577   |
| 2.              | 34.9150     | 2.569                              | 95      |     |   |
| 3.              | $35.1700^*$ | 2.551                              | 10      | 110 | 2.530   |
| 4.              | 40.5400     | 2.225                              | 75      |     |   |
| 5.              | 43.5860     | 2.076                              | 100     | 111 | 2.065   |
| 6.              | 50.8750     | 1.794                              | 70      | 200 | 1.789   |
| 7.              | $57.4275^*$ | 1.604                              | 10      | 210 | 1.599   |
| 8.              | 58.6650     | 1.573                              | 50      |     |   |
| 9.              | 70.1250     | 1.342                              | 45      |     |   |
| 10.             | 73.7000     | 1.285                              | 15      |     |   |
| 11.             | 74.9910     | 1.266                              | 60      | 220 | 1.265   |
| 12.             | 87.7350     | 1.112                              | 20      |     |   |
| 13.             | 90.8650     | 1.082                              | 60      | 311 | 1.078   |
| 14.             | 95.8600     | 1.036                              | 50      | 222 | 1.033   |
| 15.             | 98.0000     | 1.021                              | 30      |     |   |

\* Intensities of these peaks were very low.

Procedure 3 (see page 41) was used to resolve these peaks.

In order to minimize error, the lattice parameter was plotted against Nelson-Riley function. One such plot is shown in Figure 4.1. A best fit straight line was obtained by the least square method. The extrapolated value of the Lattice parameter along the best fit straight line was taken as the lattice parameter of the sample. The details are given in Appendix B.

#### 4.3 HOMOGENIZATION

Diffusivity of refractory metals in  $\text{Ni}_3\text{Al}$  is very low. For an alloy button to have the same properties throughout the bulk, it is necessary for the composition to be uniform. Hence, if there is any gradient in the concentration of the ternary addition, time has to be allowed for it to diffuse uniformly in the matrix. High temperature would accelerate the process of diffusion.

The literature reports that 7 days at  $1250^\circ\text{C}$  was necessary to homogenize the alloys of the Ni-Al-Ta (1) system. In the present work, a temperature of  $1300^\circ\text{C}$  was tried, but after 1 day at  $1300^\circ\text{C}$  incipient fusion was seen to occur. Since  $1200^\circ\text{C}$  was a temperature at which further studies would be made, it was decided to choose  $1200^\circ\text{C}$  as the homogenizing temperature.

To find out the time of homogenization, the lattice parameter of one of the alloys (7 atomic % Ta, containing B) was determined after every 3 days anneal at  $1200^\circ\text{C}$ . At the initial stages, due to rapid rate of diffusion, there should be a significant change in the lattice parameter

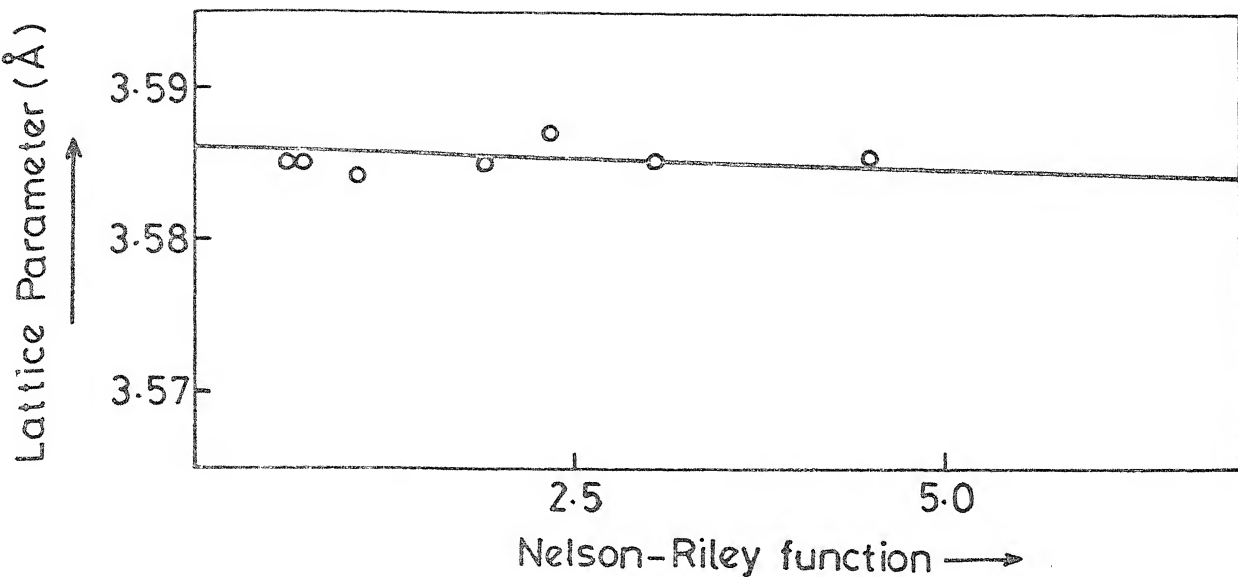


Fig 4.1 Plot of Nelson-Riley function versus lattice parameter.

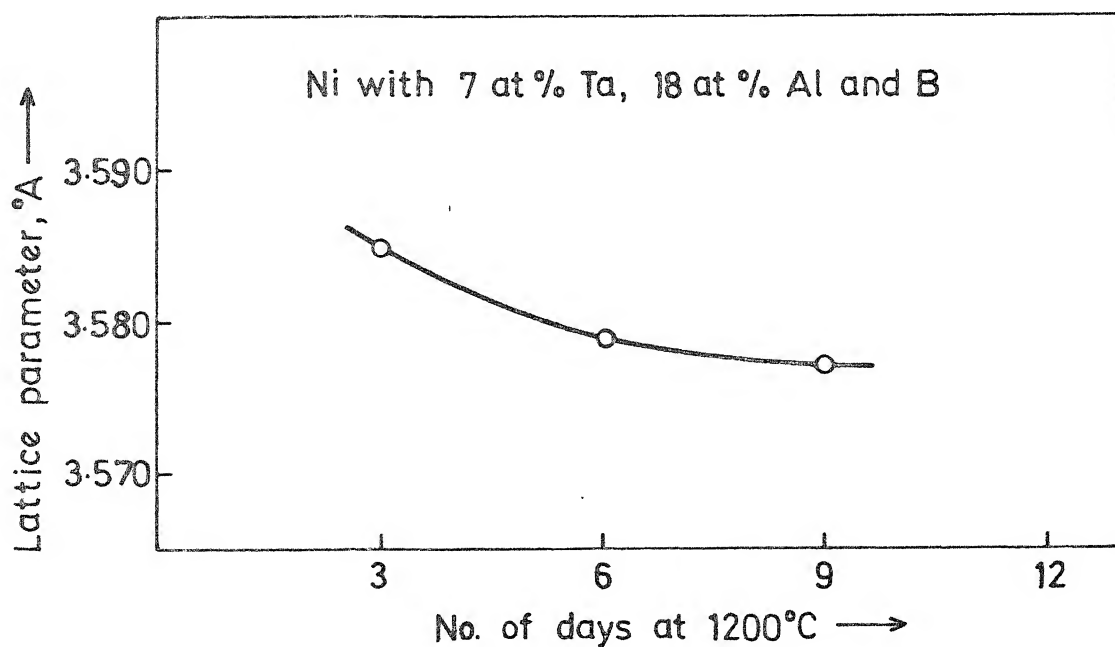


Fig. 4.2 Plot of lattice parameter versus time of homogenization at 1200°C.



of the sample, while at later stages the change would be small. This trend was observed for the alloy that was studied. Figure 4.2 gives the plot of lattice parameter versus time of homogenization.

As observed from Figure 4.2, the alloy is homogenized after about 9 days at  $1200^{\circ}\text{C}$ . But to be on the safe side, all the alloys were homogenized at  $1200^{\circ}\text{C}$  for 12 days.

#### 4.4 LATTICE PARAMETER OF ALLOYS ANNEALED AT $1200^{\circ}\text{C}$

After the alloys had been equilibrated at  $1200^{\circ}\text{C}$  for 12 days, the alloys were studied for their lattice parameters. Table 4.3 lists the lattice parameters for the alloys with Boron, at  $1200^{\circ}\text{C}$ . Table 4.4 gives the lattice parameter for alloys not containing Boron, annealed at  $1200^{\circ}\text{C}$ .

Figure 4.3 shows the plot of lattice parameter versus Ta content at  $1200^{\circ}\text{C}$  for both Boron-containing and no Boron alloys.

The lattice parameter of pure  $\text{Ni}_3\text{Al}$  without any Ta or B has been taken from literature (2). Lattice parameter of  $\text{Ni}_3\text{Al}$  is strongly dependant on heat treatment. Hence the above value taken from the literature cannot be compared with the experimentally obtained lattice parameter of Boron-doped  $\text{Ni}_3\text{Al}$ . Though the values of lattice parameter reported in the literature for pure (Boron-free)  $\text{Ni}_3\text{Al}$ , vary anywhere between 3.57 to 3.58Å, the latter value has

Table 4.3 : Lattice Parameters of Alloys Containing Boron,  
at 1200°C

| Alloy<br>Composition |         | Lattice<br>Parameter<br>(A) | Standard Deviation   |
|----------------------|---------|-----------------------------|----------------------|
| At % Ni              | At % Ta |                             |                      |
| 75                   | 0       | 3.574                       | $1.5 \times 10^{-3}$ |
| 75                   | 1       | 3.575                       | $2 \times 10^{-3}$   |
| 75                   | 2       | 3.576                       | $1 \times 10^{-3}$   |
| 75                   | 3       | 3.575                       | $1.5 \times 10^{-3}$ |
| 75                   | 7       | 3.577                       | $1 \times 10^{-3}$   |
| 75                   | 9       | 3.586                       | $1.5 \times 10^{-3}$ |

Table 4.4 : Lattice Parameter of Alloys not containing  
Boron, at 1200°C

| Alloy<br>Composition |         | Lattice<br>Parameter<br>(A) | Standard Deviation   |
|----------------------|---------|-----------------------------|----------------------|
| At % Ni              | At % Ta |                             |                      |
| 75                   | 0       | 3.580 <sup>*</sup>          | -                    |
| 75                   | 1       | 3.584                       | $1 \times 10^{-3}$   |
| 75                   | 2       | 3.585                       | $1.5 \times 10^{-3}$ |
| 75                   | 3       | 3.586                       | $1.5 \times 10^{-3}$ |
| 75                   | 7       | 3.584                       | $2 \times 10^{-3}$   |
| 75                   | 9       | 3.593                       | $2 \times 10^{-3}$   |

\* Taken from literature (Ref. 2).

105931

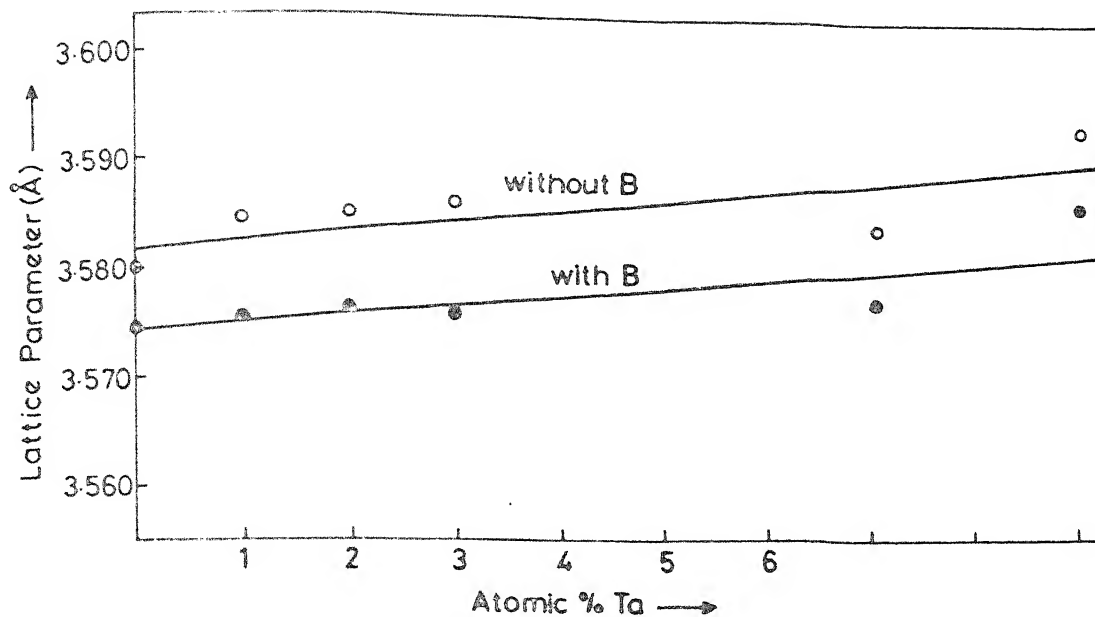


Fig.4.3 Plot of lattice parameter versus Ta content at 1200°C.

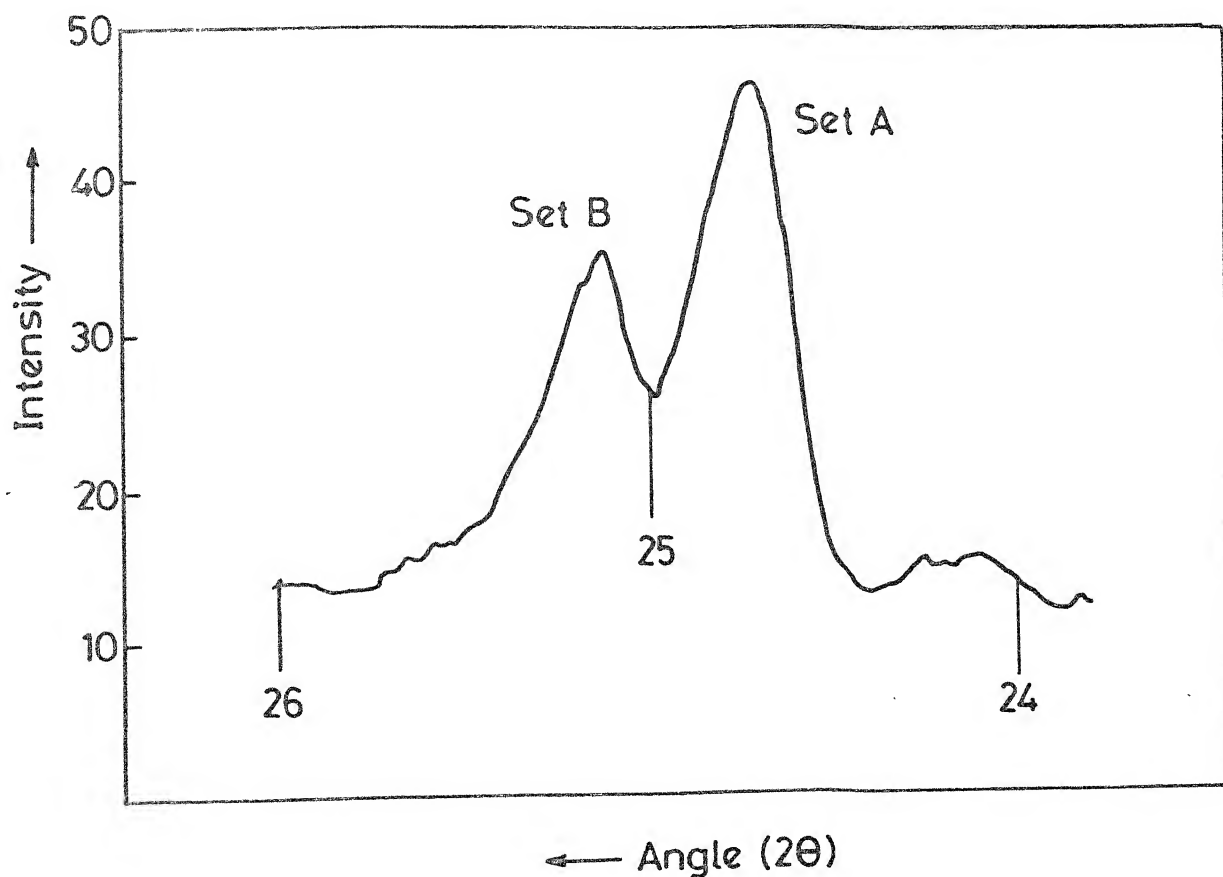


Fig.4.4 Splitting of the (100) peak of  $\text{Ni}_3\text{Al}$  at 1000°C.

been chosen because it matches with the experimentally determined parameters.

#### 4.5 LATTICE PARAMETERS OF ALLOYS ANNEALED AT 1000°C

In order to study the phase stability of the alloy system at 1000°C, extensive X-ray diffraction analysis was carried out on the samples.

##### 4.5.1 INDEXING OF THE DIFFRACTION PATTERNS OBTAINED AT 1000°C

The X ray diffraction patterns of all the alloys at 1000°C were visibly different from the diffraction patterns of the alloys at 1200°C. The unknown peaks, as given in Table 4.2 above, also appeared at 1000°C for samples containing Ta, irrespective of their B content. However, the diffraction patterns of the alloys annealed at 1000°C had the following characteristics: for each of the  $\text{Ni}_3\text{Al}$  diffraction lines (at 1200°C) there were now two peaks at 1000°C. One of the two peaks was at a slightly higher angle and the other at a slightly lower angle relative to the  $\text{Ni}_3\text{Al}$  peaks. Figure 4.4 shows the splitting of the (100) peak. It appeared as if the single peaks of  $\text{Ni}_3\text{Al}$  had split into two. Table 4.5 gives the diffraction pattern of an alloy containing 1 atom % Ta and Boron.

For our convenience, we have grouped the split peaks in two sets. The first set (Set A) is made up of peaks which are at relatively lower angles and the second set (Set B

Table 4.5 : Diffraction Pattern for B-doped Alloy containing 1 at % Ta, at 1000°C, showing two sets of peaks due to two  $\text{Ni}_3\text{Al}$  type phases

Lattice parameter for Set A,  $a = 3.580 \text{ \AA}$

Lattice parameter for Set B,  $a_3 = 3.541 \text{ \AA}$

| Line No. | $2\theta$ | Set A |         |     |              | Set B |         |     |              |
|----------|-----------|-------|---------|-----|--------------|-------|---------|-----|--------------|
|          |           | d     | $I/I_0$ | hkl | d calculated | d     | $I/I_0$ | hkl | d calculated |
| 1.       | 24.9270   | 3.586 | 20      | 100 | 3.580        |       |         |     |              |
| 2.       | 25.0900   |       |         |     |              | 3.549 | 20      | 100 | 3.541        |
| 3.       | 34.8610*  | -     | -       | -   | -            | -     | -       | -   | -            |
| 4.       | 35.2296   | 2.547 | 15      | 110 | 2.531        |       |         |     |              |
| 5.       | 35.4261   |       |         |     |              | 2.533 | 15      | 110 | 2.503        |
| 6.       | 40.4960*  | -     | -       | -   | -            | -     | -       | -   | -            |
| 7.       | 43.7773   | 2.068 | 100     | 111 | 2.067        |       |         |     |              |
| 8.       | 44.2173   |       |         |     |              | 2.048 | 100     | 111 | 2.044        |
| 9.       | 51.0240   | 1.789 | 75      | 200 | 1.790        |       |         |     |              |
| 10.      | 51.4040   |       |         |     |              | 1.775 | 75      | 200 | 1.771        |
| 11.      | 57.5475   | 1.601 | 15      | 210 | 1.601        |       |         |     |              |
| 12.      | 57.9623   |       |         |     |              | 1.591 | 10      | 210 | 1.584        |
| 13.      | 58.6250*  | -     | -       | -   | -            | -     | -       | -   | -            |
| 14.      | 70.1050*  | -     | -       | -   | -            | -     | -       | -   | -            |
| 15.      | 75.0888   | 1.265 | 60      | 220 | 1.265        |       |         |     |              |
| 16.      | 75.9488   |       |         |     |              | 1.253 | 60      | 220 | 1.252        |
| 17.      | 91.0123   | 1.080 | 40      | 311 | 1.079        |       |         |     |              |
| 18.      | 91.9263   |       |         |     |              | 1.072 | 35      | 311 | 1.068        |
| 19.      | 96.5286   | 1.033 | 35      | 222 | 1.033        |       |         |     |              |
| 20.      | 97.7886   |       |         |     |              | 1.023 | 30      | 222 | 1.022        |

\* Peaks due to unknown phase, annealed alloys (See Table 4.2).

is made up of peaks which are at relatively higher angles in the pairs of split peaks. In Figure 4.4, the peak belonging to Set A is marked as A, while the one belonging to Set B is marked B.

Table 4.5 shows that both the sets can be individually indexed on the basis of  $\text{Ni}_3\text{Al}$  structure.

#### 4.5.2 LATTICE PARAMETERS OF THE ALLOYS AT 1000°C

At 1000°C, as has been mentioned before, the  $\text{Ni}_3\text{Al}$  peaks had split into two. These split peaks can be grouped into two sets (Sets A and B), as has been described in section 4.5.1 above, each set of which can be indexed on the basis of  $\text{Ni}_3\text{Al}$  structure. Hence, while calculating the lattice parameter, the two sets were considered separately and for each alloy two lattice parameters were obtained.

Table 4.6 gives the two lattice parameters of each alloy containing Boron. The lattice parameter data is also plotted in Figure 4.5. Table 4.7 and Figure 4.6 show the lattice parameter data for Boron-free alloys at 1000°C.

#### 4.6 OPTICAL MICROSCOPY

##### 4.6.1 CHOICE OF ETCHING REAGENT

Developing a proper microstructure depends greatly on the type of etching reagent used, besides being dependent on other factors such as careful polishing etc.

Initially, alcoholic ferric chloride was tried out as the etching reagent. But this reagent failed to reveal the second phase, whereas the X-ray diffraction pattern

Table 4.6 : Lattice Parameters of Alloys Containing Boron,  
at 1000°C

| Alloy Composition |         | Lattice<br>parameter<br>in A<br>for SET A | Standard<br>Deviation | Lattice<br>Parameter<br>in A<br>for SET B | Standard<br>Deviation |
|-------------------|---------|---|-----------------------|---|-----------------------|
| At % Ni           | At % Ta |   |                       |   |                       |
| 75                | 0       | 3.578                                     | $1 \times 10^{-3}$    | 3.542                                     | $1.5 \times 10^{-3}$  |
| 75                | 1       | 3.580                                     | $2 \times 10^{-3}$    | 3.541                                     | $1.5 \times 10^{-3}$  |
| 75                | 2       | 3.582                                     | $1.5 \times 10^{-3}$  | 3.543                                     | $2 \times 10^{-3}$    |
| 75                | 3       | 3.584                                     | $2 \times 10^{-3}$    | 3.547                                     | $3.5 \times 10^{-3}$  |
| 75                | 7       | 3.591                                     | $1 \times 10^{-3}$    | 3.561                                     | $1.5 \times 10^{-3}$  |
| 75                | 9       | 3.595                                     | $2 \times 10^{-3}$    | 3.570                                     | $1 \times 10^{-3}$    |

Table 4.7 : Lattice Parameters of Alloys not containing  
Boron, at 1000°C

| Alloy Composition |         | Lattice<br>parameter<br>in A<br>for SET A | Standard<br>Deviation | Lattice<br>Parameter<br>in A<br>for SET B | Standard<br>Deviation |
|-------------------|---------|---|-----------------------|---|-----------------------|
| At % Ni           | At % Ta |   |                       |   |                       |
| 75                | 0       | -   | -                     | -   | -                     |
| 75                | 1       | 3.579                                     | $1 \times 10^{-3}$    | 3.54                                      | $8 \times 10^{-3}$    |
| 75                | 2       | -   | -                     | -   | -                     |
| 75                | 3       | 3.585                                     | $2 \times 10^{-3}$    | 3.54                                      | $7.5 \times 10^{-3}$  |
| 75                | 7       | 3.583                                     | $1.5 \times 10^{-3}$  | 3.545                                     | $2 \times 10^{-3}$    |
| 75                | 9       | 3.588                                     | $1 \times 10^{-3}$    | 3.554                                     | $1 \times 10^{-3}$    |

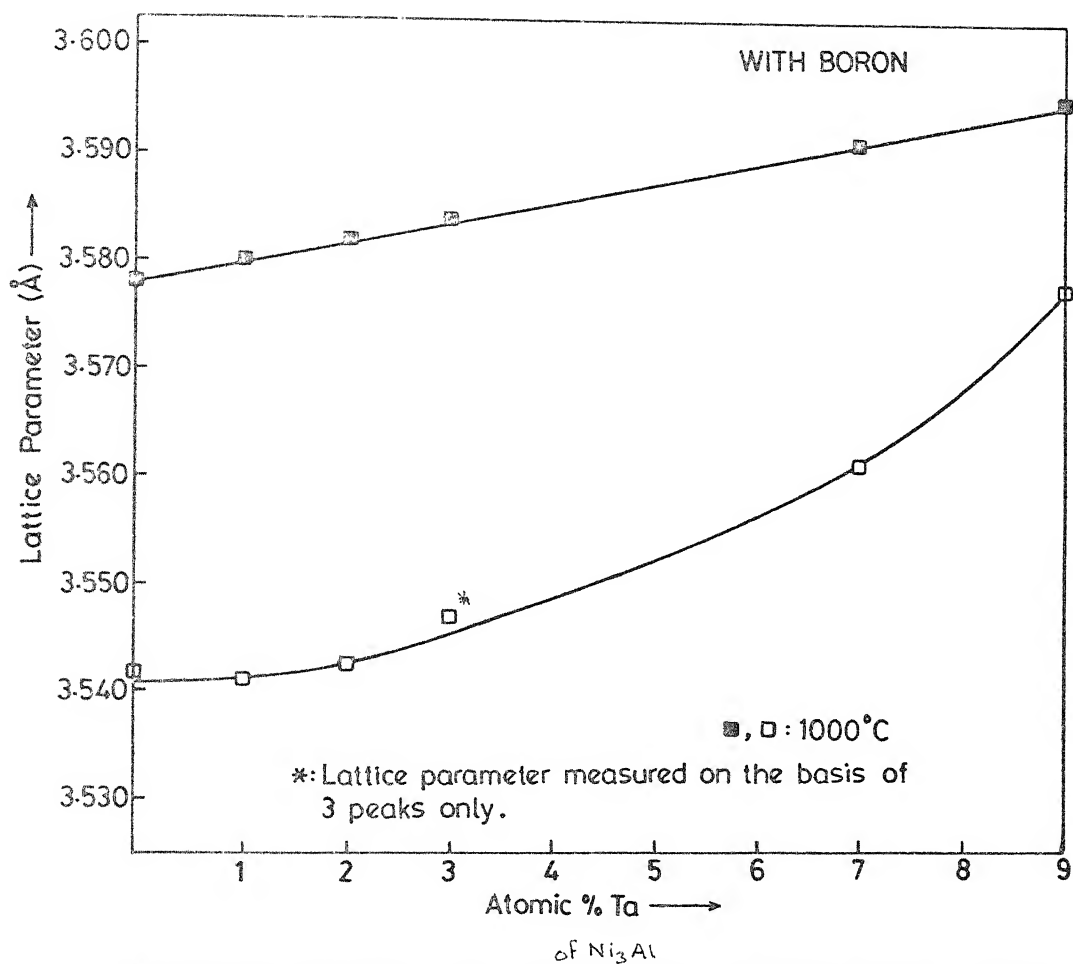


Fig.4.5 Plot of lattice parameter/versus Ta content of alloys containing Boron at 1000°C.



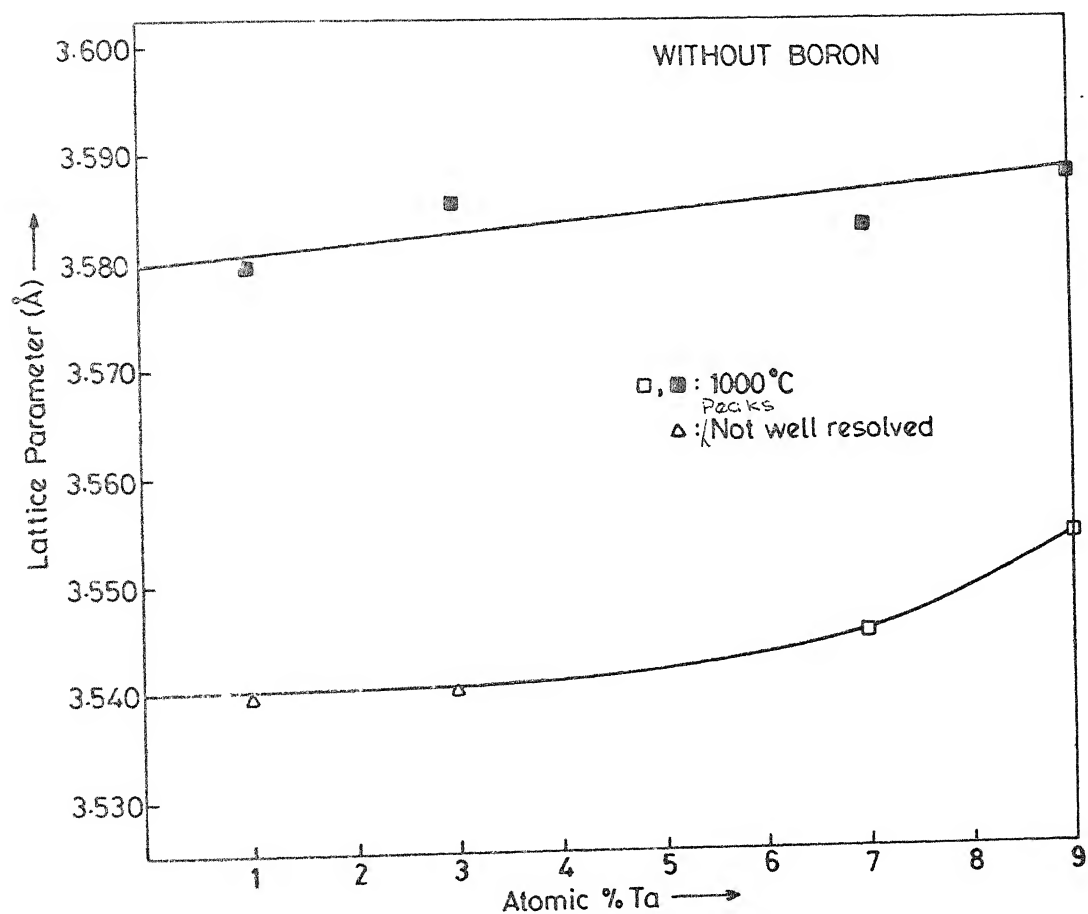


Fig. 4.6 Plot of lattice parameter versus Ta content of alloys not containing Boron at 1000°C.

clearly indicated that at least one phase besides  $\text{Ni}_3\text{Al}$  is present in the alloys. Except severe pitting and a flat matrix no other structures could be seen with this reagent. Alcoholic ferric chloride had hardly any effect.

Nash and West (1,3) report the use of Marble's Reagent as the etching reagent. This etchant was found to be very strong. The grain boundaries were very deeply etched while different areas in single grain showed different rates of etching. As a result the surface of the specimen became uneven with certain regions elevated and certain regions depressed. The microstructure that was obtained, was similar to that reported by Chakraborty et al (4). These effects of over-etching appeared just after 5 seconds of dipping in Marble's reagent. Hence, neither was it possible to observe the development of microstructure, nor was it possible to analyse the microstructure owing to the effect of over-etching. This etching reagent was, thus, rejected.

Finally electro-etching was tried out with 10% oxalic acid solution. The proper time-current combination was found out and the gradual evolution of the microstructure could be very easily followed. The photomicrographs given in figures 4.7 to 4.29 show the effect of etching.

#### 4.6.2 THE PHOTOMICROGRAPHS

Though electron microscope was essential for this work, owing to the unavailability of the equipment, optical

microscopy had to meet the necessity. In all the microstructures photographed (Fig. 4.7 to Fig. 4.29), some diffused dark patches have appeared. These features were not present in the microstructures. Close observation will reveal that the same pattern of patches appear on all the photographs as well as the photograph negatives. Hence, these patches must have come from the lens system of the microscope and are not features of the microstructures.

Figure 4.7 shows the photomicrograph of an alloy in the as-cast condition. The junction of the chilled layer and the columnar grains is clearly visible.

Figures 4.8 to 4.23 show the photomicrographs of alloys annealed at  $1200^{\circ}\text{C}$ . Figures 4.8, 4.10 and 4.14 show etched surfaces of Foron doped alloys containing 1 at % , 3 at % and 7 at % Ta respectively. They clearly show an increase in the amount of dark spots (holes) with increasing Ta. This trend is not carried on to the 9 at % Ta sample (Figure 4.19). That the dark spots can be seen before etching, is shown in Figures 4.11, 4.13, 4.15, 4.18 and 4.21. Also to be noticed in these figures is the fact that these dark spots are located along the grain boundaries. Figures 4.21 and 4.22, which are photomicrographs of the same region before and after etching. These two micrographs show that the numbers of dark spots or holes have increased with etching. In Figure 4.15 particles at the grain boundaries have been revealed by careful polishing. The effect of etching on

on this sample is shown in Figures 4.16 and 4.17. Etching reveals the grain boundaries but etches out the particles at the grain boundaries. The phase marked as A in Figure 4.17 appears only in this alloy (7 at % Ta and no B).

This phase is seen only near regions of large dark patches or holes, which may have been created to by chipping out or etching out of massive grain boundary precipitate particles.

In alloys with 9 atomic % Ta with or without Boron, a new phase is visible even before etching. This phase is marked B in Figures 4.18 to 4.23. This phase becomes clearly outlined on etching (Figures 4.19, 4.20, 4.23).

The photomicrographs of samples that had been annealed at 1000°C are shown in Figures 4.24 to 4.29. Holes at the grain boundaries persist in these samples too. But increase in the amount of holes with increasing Ta content is not so evident. In Figure 4.27 the band around the grain boundary is an etching effect. The phase marked B in Figures 4.18 to 4.23 also persist in case of 1000°C annealed for 9 at % Ta samples (Figures 4.27, 4.28, 4.29).

One thing to be noticed is that in the case of the Boron free alloy containing 1 atom % Ta twinned regions can be seen in some of the grains. These regions appear both at 1200°C and at 1000°C (Figures 4.9 and 4.24). In the Boron containing alloys, no twins were observed.

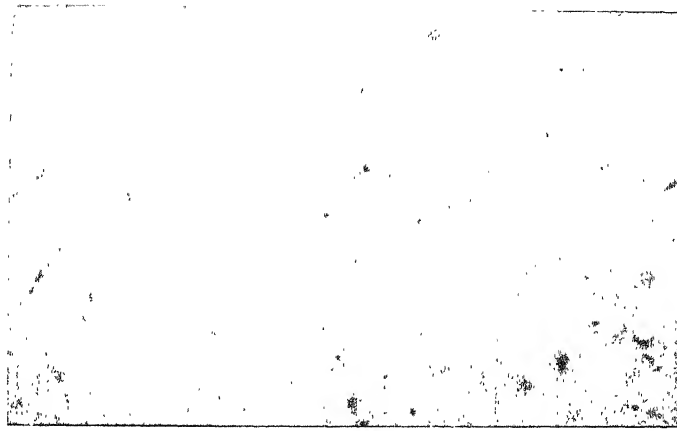


Fig. 4.7 : Photomicrograph of As-Cast Structure of Alloy Buttons.

Mag: 100X

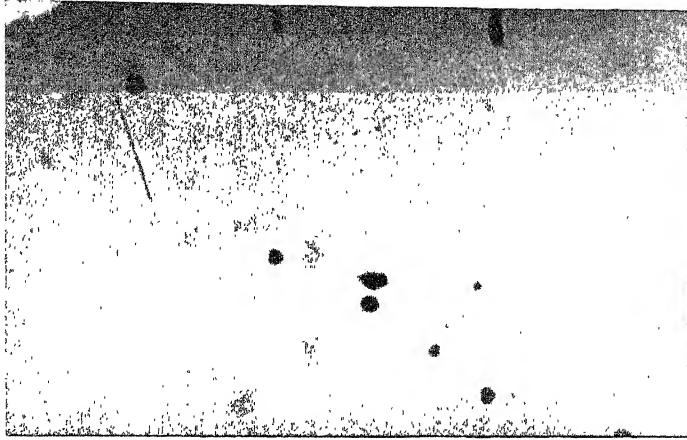


Fig. 4.8 : Photomicrograph of Boron-doped 1 at%Ta alloy,  
at 1200°C.  
Mag: 500X

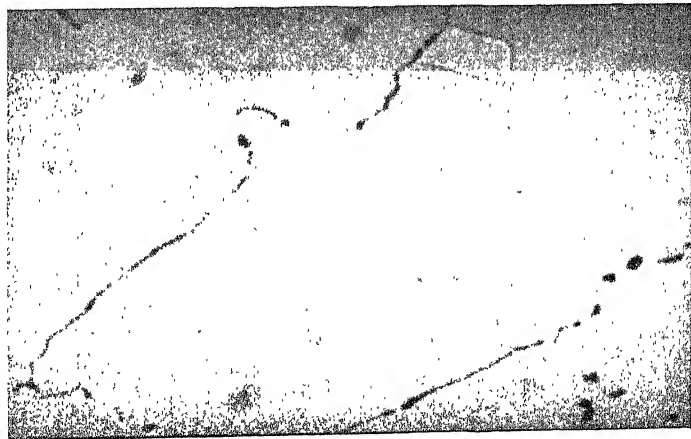


Fig. 4.9 : Photomicrograph of without-Boron 1 at%Ta alloy  
at 1200°C.

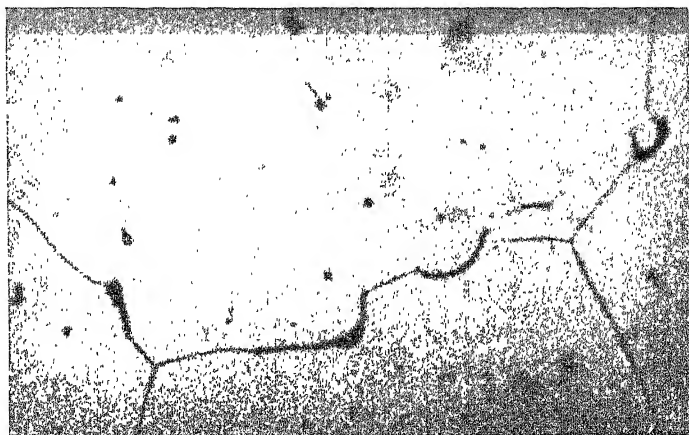


Fig. 4.10 : Photomicrograph of Boron-doped 3at% Ta alloy,  
at 1200°C.  
Mag: 200X

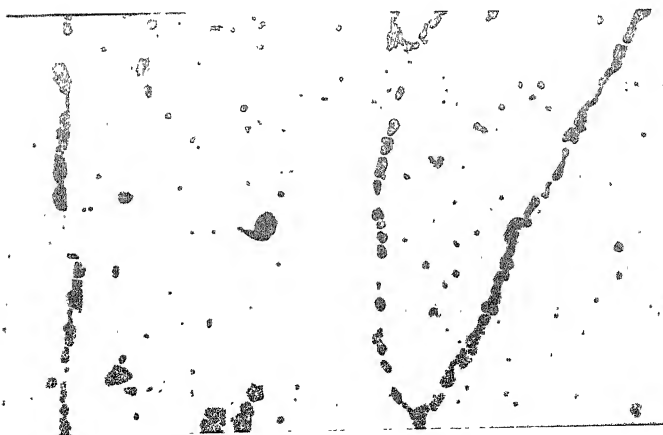


Fig. 4.11 : Photomicrograph of without-Boron 3at% Ta al  
at 1200°C, before etching.  
Mag: 100X

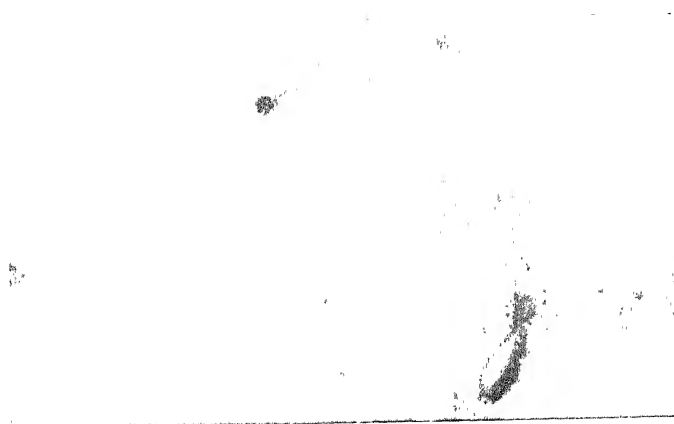


Fig. 4.12 : Photomicrograph of without-Boron 3at% Ta alloy,  
at 1200°C, after etching.  
Mag: 200X

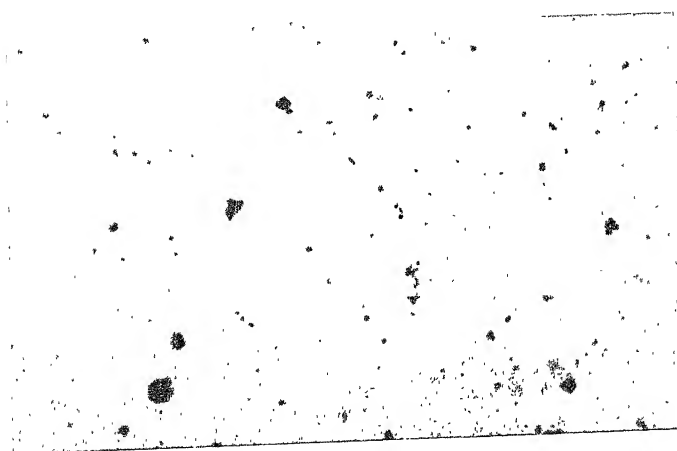


Fig. 4.13 : Photomicrograph of Boron-doped 7at% Ta alloy,  
at 1200°C, before etching.  
Mag: 100X



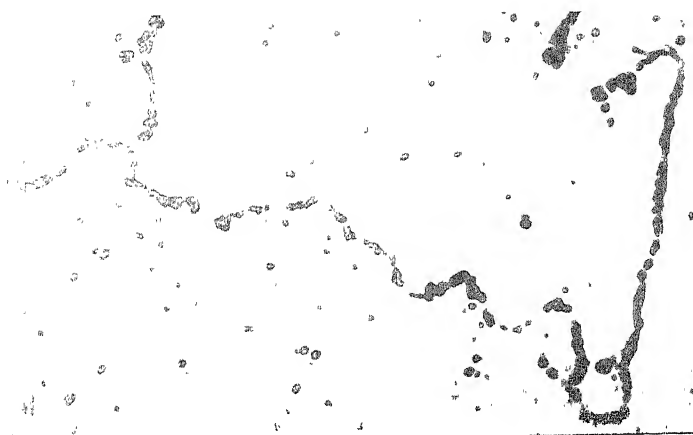


Fig. 4.14 : Photomicrograph of Boron-doped 7at% Ta alloy,  
at 1200°C, after etching.

Mag: 100X

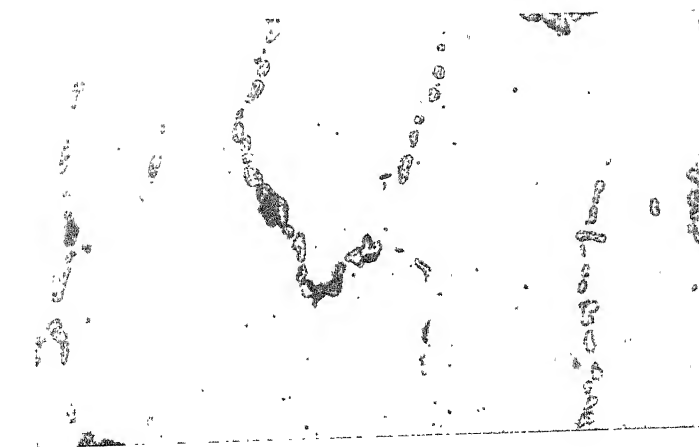


Fig. 4.15 : Photomicrograph of without-Boron 7at% Ta alloy  
at 1200°C, before etching.

Mag: 100X

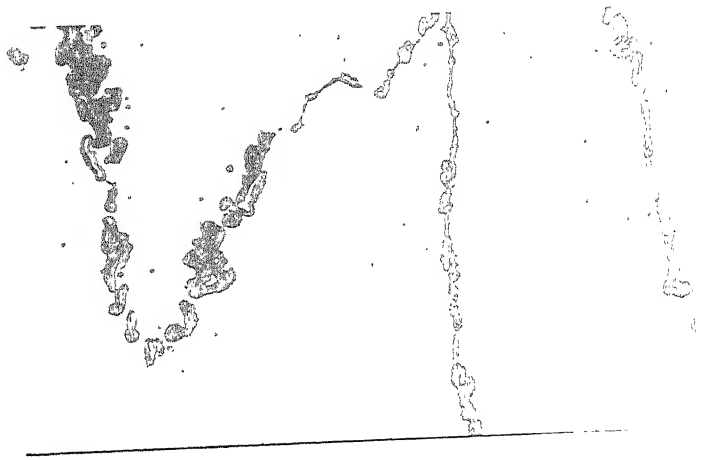


Fig. 4.16 : Photomicrograph of without-Boron 7at% Ta alloy,  
at 1200°C, after 5 minutes of etching,  
Mag: 100X.



Fig. 4.17 : Photomicrograph of without-Boron 7at% Ta alloy,  
at 1200°C, after 10 minutes of etching,  
Mag: 500X.

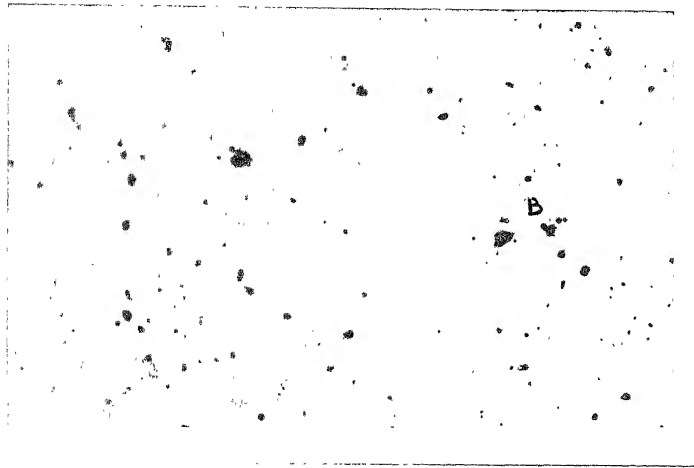


Fig. 4.18 : Photomicrograph of Boron doped, 9at% Ta alloy,  
at 1200°C, before etching.

Mag: 100X

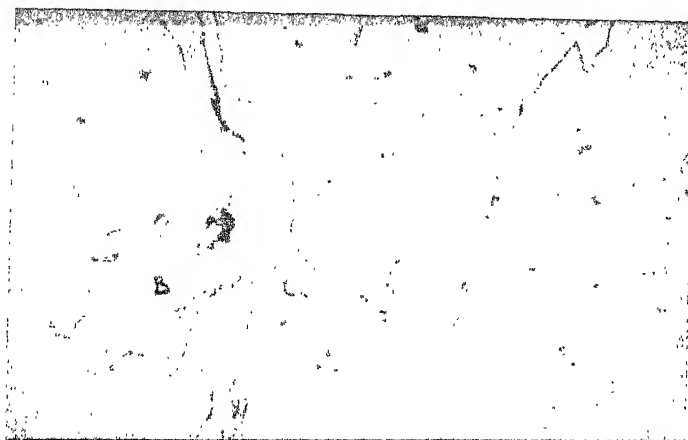


Fig. 4.19 : Photomicrograph of Boron-doped, 9at% Ta alloy,  
at 1200°C, after 5 minutes etching.

Mag: 100X.

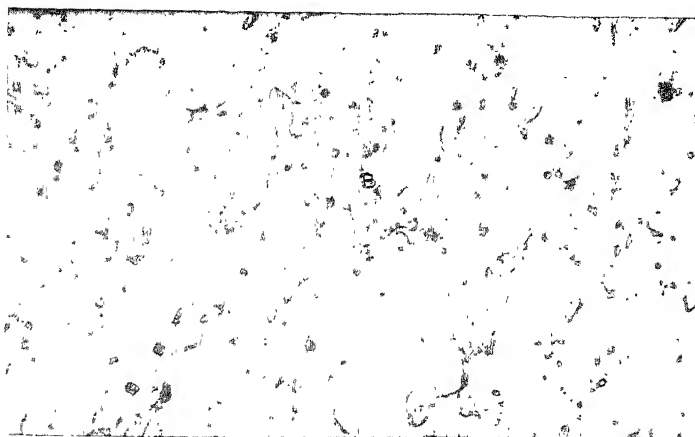


Fig. 4.20 : Photomicrograph of Boron-doped 9at% Ta alloy,  
at 1200°C, after 10 minutes of etching.  
Mag: 200X.

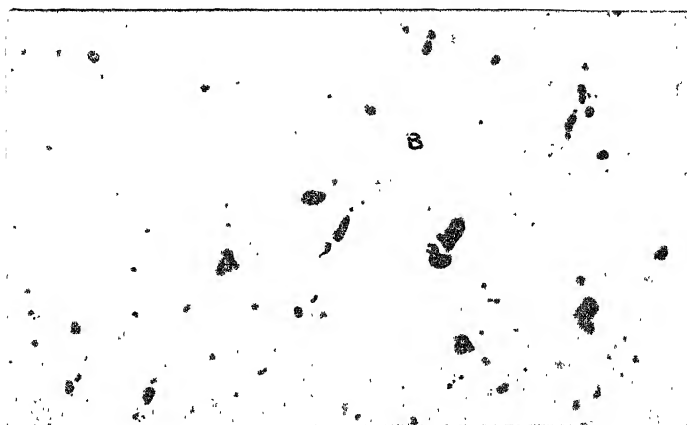


Fig.4.21 : Photomicrograph of without-Boron, 9at% Ta alloy  
at 1200°C, before etching.  
Mag: 100X.

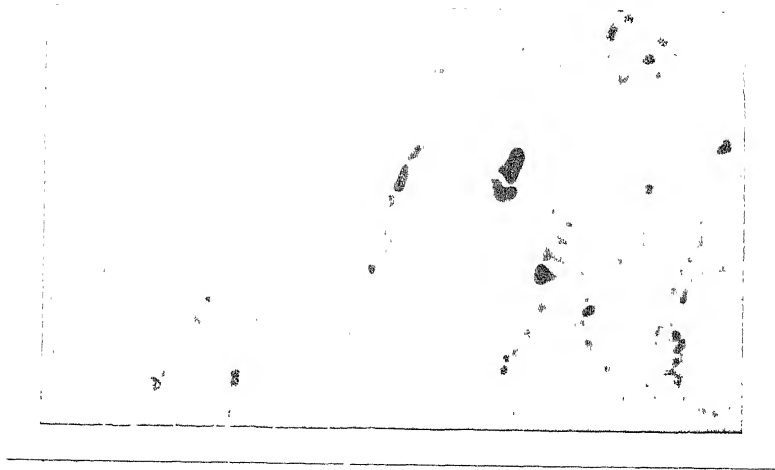


Fig. 4.22 : Photomicrograph of without Boron, 9at% Ta alloy, at 1200°C after 10 minutes of etching.  
Mag: 100X.

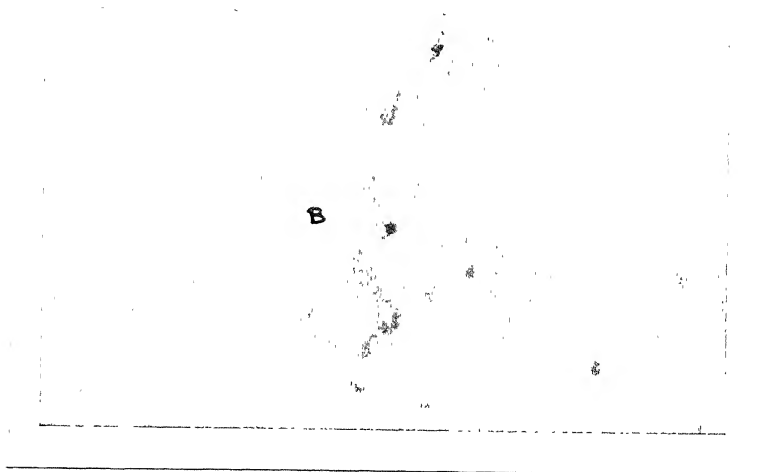


Fig. 4.23 : Photomicrograph of without Boron, 9at% Ta alloy, at 1200°C after 10 minutes of etching.  
Mag: 500X.

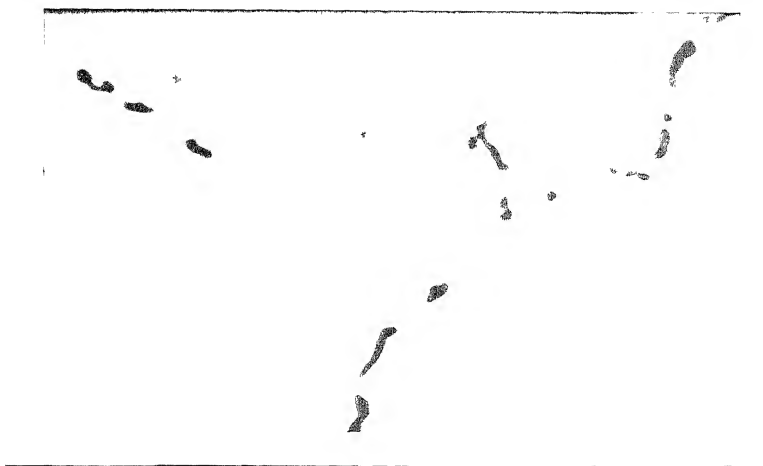


Fig. 4.24 : Photomicrograph of without-Boron, 1at% Ta Alloy  
at 1000°C, after 10 minutes of etching.  
Mag: 100X



Fig. 4.25 : Photomicrograph of without-Boron, 3at%Ta alloy  
at 1000°C before etching.  
Mag: 500X

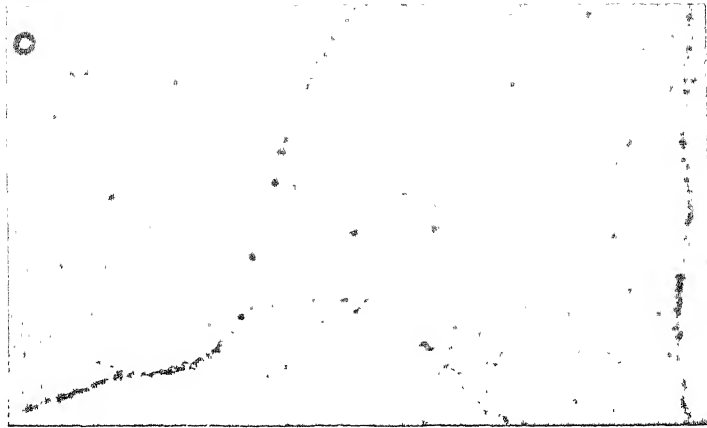


Fig. 4.26 : Photomicrograph of without-Boron, 7at% Ta alloy, at 1000°C, after 10 minutes of etching.  
Mag: 100X.

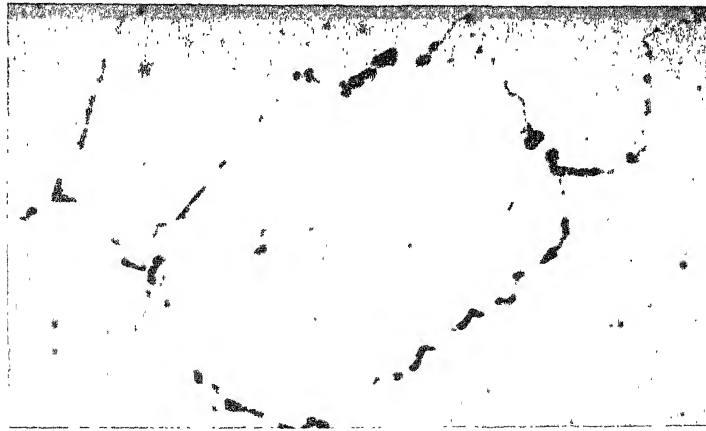


Fig. 4.27 : Photomicrograph of Boron-doped, 9at%Ta alloy, at 1000°C, after 10 minutes of etching.  
Mag: 100X.

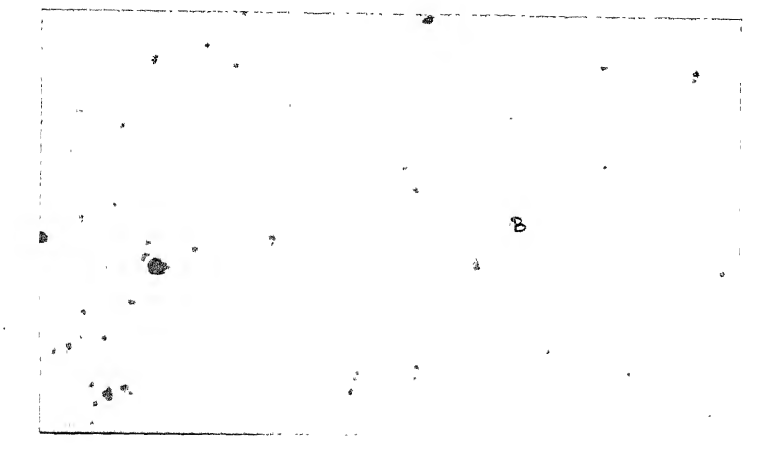


Fig. 4.28 : Photomicrograph of without-Boron, 9at%Ta alloy,  
at 1000°C, before etching.  
Mag: 100X.

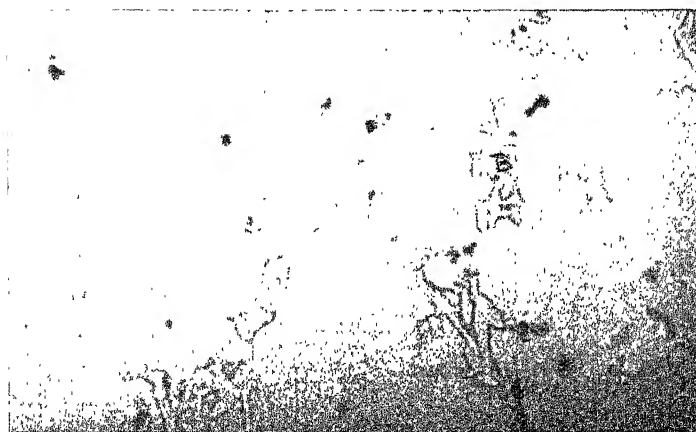


Fig. 4.29 : Photomicrograph of without-Boron, 9at% Ta alloy,  
at 1000°C, after 10 minutes of etching.  
Mag: 500X.



#### 4.7 THE DIFFERENTIAL SCANNING CALORIMETRY OF Ni-Al-Ta ALLOYS

After equilibrating the samples at 1000°C, an unprecedented splitting of the  $\text{Ni}_3\text{Al}$  diffraction peaks occurred for all alloys. This indicated that some phase transformation must have occurred in the system. Since a phase transformation would be associated with a thermal effect, differential scanning calorimetry was tried to detect the thermal effect as well as to determine the transformation temperature. Two alloys were investigated using the D.S.C. technique.

The D.S.C. plots are shown in Figure 4.30. The two samples give similar curves. The region A, C, D and E are reproduced in both the plots. The region B in curve 1 is absent in curve 2. This may be due to the effect of weight (weight of sample for curve 2 was less than that for curve 1) or an effect of Ta. Details for curves 1 and 2 are given in Table 4.8.

#### 4.8 MICROHARDNESS

If phases differ significantly in their compositions their microhardness values are expected to be different. So we used microhardness for phase identification.

Microhardness was taken on precipitate particles at grain boundaries. These particles had been revealed after taking utmost care in polishing. About 10 microhardness

Table 4.8 : Details of DSC Run

|                       | Curve 1                                     | Curve 2                                     |
|-----------------------|---|---|
| Specimen weight       | 195 mg                                      | 137 mg                                      |
| Pt. Standard          | 55.1 mg                                     | 113 mg                                      |
| Composition of sample | 75 % Ni<br>25 % Al<br>0 % Ta<br>Boron doped | 75 % Ni<br>24 % Al<br>1 % Ta<br>Boron doped |

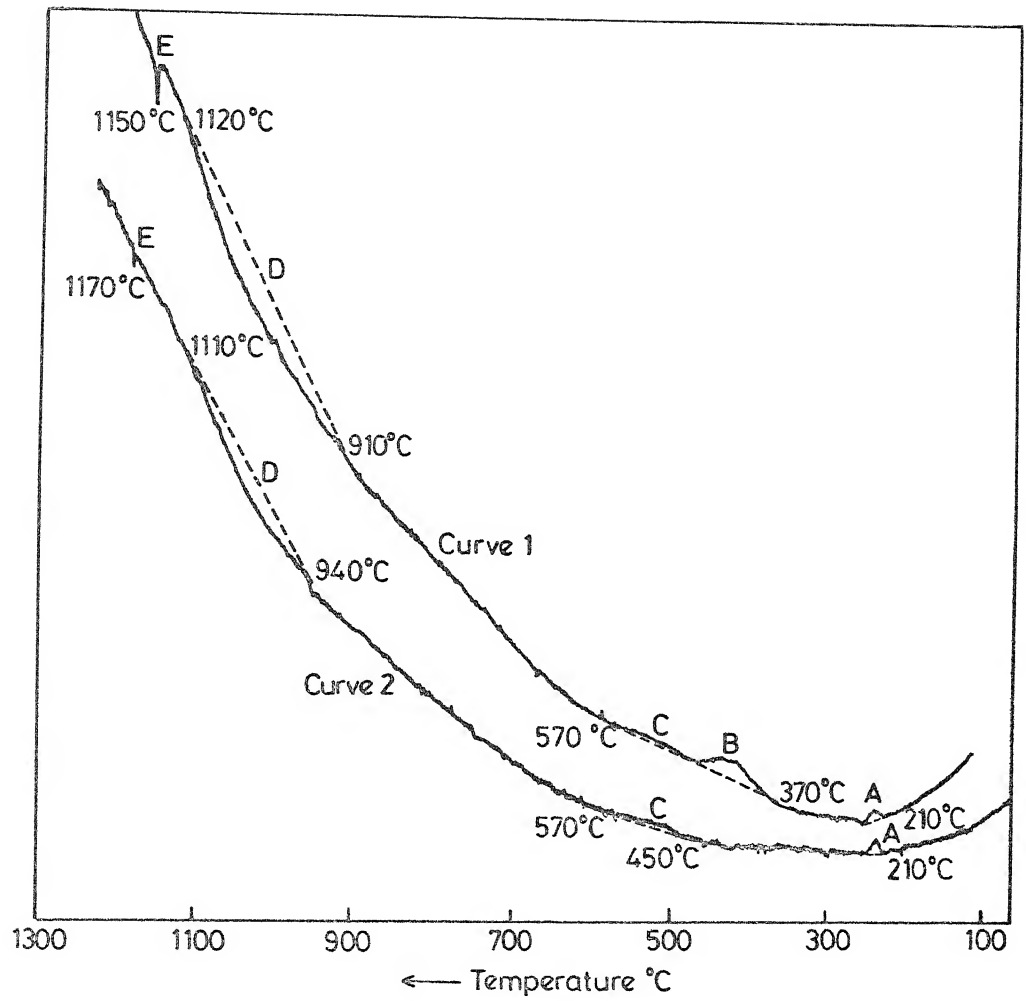


Fig. 4.30 The differential scanning calorimeter plot for two samples.

readings for grain boundary particles <sup>were</sup> taken on various samples. The microhardness of the particles at the grain boundaries <sup>were</sup> ~~may~~ very high compared to that of the matrix phase. Whereas the microhardness of the matrix phase varied between 450 and 530 kg/mm<sup>2</sup> (using Vickers indenter), that of the precipitate particle at the grain boundary varied between 1200 and 1400 kg/mm<sup>2</sup>.

However, the phase marked B in Figures 4.18 to 4.23 and in Figures 4.26, 4.28 and 4.29, do not show any difference in microhardness from that of the matrix.

The comparable intensities of the split peaks in the diffraction patterns of alloys annealed at 1000°C indicated that the two phases (which gave rise to the two sets of peaks) were present in the alloys in comparable amounts. This meant that the number of grains of the two phases would be comparable. As microstructurally the grains belonging to each phase could not be identified, attempt was made to find out the phases by their difference in microhardness. Microhardness readings were taken in various regions of the samples so that grains of both the phases could be covered. However, the microhardness values throughout varied between 450 kg/mm<sup>2</sup> and 500 kg/mm<sup>2</sup>. The microhardness of the two phases did not differ much each other. Hence the phases could not be identified from their difference in microhardness.

#### 4.9 MEASUREMENT OF INTENSITY OF DIFFRACTION PEAKS

Integrated intensities of diffraction peaks, particularly the superlattice lines, yield important information about the nature of substitution of alloying element. For structural analysis and to know whether Ta substitutes Al or Ni in  $\text{Ni}_3\text{Al}$ , the integrated intensities of the first two superlattice peaks and the first two fundamental peaks were calculated for the Boron doped 1 at% Ta alloy, annealed at  $1000^\circ\text{C}$ .

The integrated intensity was obtained from the area under the diffraction peak. Area under each split peak was obtained separately. As the split peaks were not fully resolved, extrapolation was done to obtain two superimposing, visually symmetrical peaks. This is shown in Figure 4.31. The area under each peak was calculated by placing the symmetrically extrapolated peaks on a measured grid (e.g. graph paper).

The result is shown in Table 4.9 .

Table 4.9 Scaled Integrated Intensities from Area Under Diffraction Peaks

| hkl | Peaks of Set A                     |                     | Peaks of Set B                     |                     |
|-----|------------------------------------|---------------------|------------------------------------|---------------------|
|     | Absolute<br>area ( $\text{mm}^2$ ) | Scaled<br>Intensity | Absolute<br>Area ( $\text{mm}^2$ ) | Scaled<br>Intensity |
| 100 | 567.0                              | 2.91                | 430.0                              | 1.44                |
| 110 | 460.5                              | 1.96                | 328.0                              | 1.10                |
| 111 | 2350.0                             | 10.00               | 2980.0                             | 10.00               |
| 200 | 496.0                              | 4.24                | 1253.0                             | 4.20                |

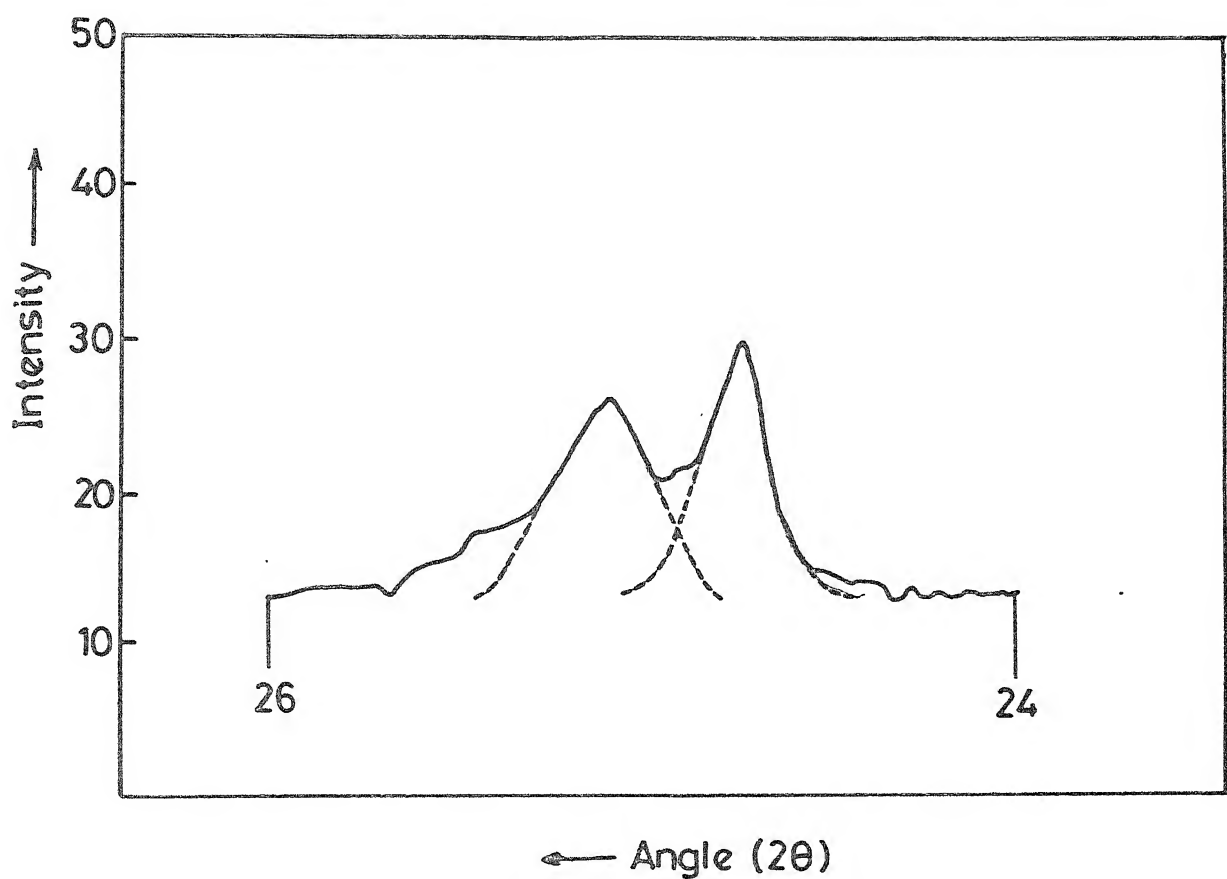


Fig.4.31 Extrapolation of peaks for area calculation.

REFERENCES

1. P. Nash and D.R.F. West, Metal Sci. J., Vol. 13, 1979, p.670.
2. Bradley and Taylor, Proc. Roy. Soc. (London), A159, 1937, pp. 56-72.
3. P. Nash and D.R.F. West, Met. Sci., Vol. 17, 1983, p. 99.
4. S. Chakraborty and D.R.F. West, Met. Sci., Vol. 18, 1984, p. 207.

## CHAPTER 5

### DISCUSSION

In order to study the effect of Ta and B on the phase stability of  $N_3Al$ , alloys were prepared in two sets with increasing Ta content. One set containing Boron and the other devoid of any Boron. X-ray diffraction was most widely used in the study.

#### 5.1 COMPOSITION OF THE ALLOYS

In the absence of proper facilities for accurate determination of chemical composition, the actual composition of the alloys could not be verified. However, the melting loss for the alloys was found to vary between 0.3 and 0.5% and hence it is expected that the alloy compositions did not deviate much from the intended ones. Table 5.1 gives the melting loss of some of the alloys.

Table 5.1 : Melting Loss of Some Alloys

| Alloy Composition |       |                     | Weight<br>before<br>melting | Weight<br>after<br>melting | %<br>Loss |
|-------------------|-------|---------------------|-----------------------------|----------------------------|-----------|
| At%Ni             | Al%Ta | Containing<br>Boron | Gms                         | Gms                        |           |
| 75                | 1     | Yes                 | 14.9991                     | 14.9286                    | 0.47      |
| 75                | 1     | No                  | 14.9986                     | 14.9405                    | 0.38      |
| 75                | 9     | Yes                 | 14.9957                     | 14.9416                    | 0.36      |
| 75                | 9     | No                  | 14.9979                     | 14.9462                    | 0.34      |



The master alloy, (Boron-doped  $\text{Ni}_3\text{Al}$ ) obtained from the Defence Metallurgical Research Laboratory could not be analysed for its exact chemical composition. However, the diffraction pattern obtained for the master alloy tallied very well with the diffraction pattern of  $\text{Ni}_3\text{Al}$  given in the ASTM data cards (Table 4.1)(App.C). Moreover, intensity calculations were done for pure  $\text{Ni}_3\text{Al}$ . The calculated relative intensities showed excellent match with the observed relative intensities for Boron-doped  $\text{Ni}_3\text{Al}$ . These indicate that the master alloy must have had a composition very near to stoichiometric  $\text{Ni}_3\text{Al}$ .

## 5.2 HOMOGENIZING TEMPERATURE

Lattice parameter measurement as a function homogenisation time at  $1200^\circ\text{C}$  showed (Figure 4.2) that almost 12 days are required at  $1200^\circ\text{C}$  for the alloys to get homogenized. An attempt was made to decrease the homogenizing time by increasing the homogenisation temperature to  $1300^\circ\text{C}$ . When the Boron doped sample containing 7 atomic % Ta was checked after 1 day at  $1300^\circ\text{C}$ , it was, however, found that the sample had partially melted. Though the Ni-Al binary shows the melting point of  $\text{Ni}_3\text{Al}$  to be around  $1360^\circ\text{C}$ , on addition of 7 at % Ta, the melting point seems to have come below  $1300^\circ\text{C}$ . A scan of the available literature revealed one mention about the reduction of the solidus temperature of  $\text{Ni}_3\text{Al}$  with increasing amount of Ta(1). However, no quantitative data was available in this regard. No attempt was made to

establish the exact solidus temperature or its dependence on Ta content.

Since 1200°C was a temperature at which phase equilibria study would be made, it was decided to homogenize the alloys at 1200°C.

### 5.3 LATTICE PARAMETERS OF THE $\gamma'$ PHASE

Lattice parameter studies formed the most important part of the present investigation. Initially lattice parameter was used to determine the time required for homogenising the alloys.

The atomic radius of Ta (1.46) is slightly greater than that of Al (1.41) and is much larger than that of Ni (1.26). Figures 4.3, 4.5 and 4.6 show that the lattice parameter of  $\text{Ni}_3\text{Al}$  increases with increasing Ta. But the increase is not very large. For a Boron-doped 7 at % Ta alloy at 1200°C, the percentage increase in lattice parameter ( $\frac{\Delta a}{a_{\text{Ni}_3\text{Al}}} \times 100$ ) is only about 0.08%. This possibly indicates that Ta substitutes Al and not Ni in  $\text{Ni}_3\text{Al}$ .

Since B is a small size atom, it is expected to go into the interstitial sites of  $\text{Ni}_3\text{Al}$  structure and an increase in lattice parameter is to be expected due to B addition. The lattice parameter data in Figures 4.3, 4.5 and 4.6, however show that the Boron doped alloys have smaller lattice parameter than the non-Boron alloys. This may be due to segregation of B

to the grain boundaries or due to the formation of Borides of elements with large atomic diameters (Al and Ta). Both Al and Ta form stable Borides. In either case most of B does not remain in solid solution. If B forms stable borides of Al and/or Ta, the matrix also gets depleted of Al or Ta (elements with large atomic diameter). This may results in a decrease of lattice parameters of the alloy relative to the  $\text{Ni}_3\text{Al}$  alloy containing on B.

#### 5.4 ANALYSIS OF DIFFRACTION PEAKS DUE TO THE UNKNOWN PHASE

X-ray diffraction patterns of the Ni-Al-Ta alloys with or without Boron showed the presence of diffraction peaks other than those for the  $\text{Ni}_3\text{Al}$  phase. An attempt was made to identify the phase which gave rise to the extra diffraction peaks.

In the Ni-Al-Ta system several intermediate phases exist. These phases are  $\text{Ni}_6\text{AlTa}$ ,  $\text{Ni}_2\text{AlTa}$ ,  $\text{Ni}_8\text{AlTa}$ ,  $\text{NiAlTa}$ . The binary phases near the investigated composition regions are:  $\text{Ni}_3\text{Ta}$  (monoclinic, tetragonal and orthorhombic),  $\text{Ni}_8\text{Ta}$  and  $\text{NiAl}$ . There is also the Ni-rich solid solution phase .

In order to identify the extra diffraction peaks observed in Ta containing alloys. The diffraction patterns of all the phases mentioned above are compared with the unknown diffraction peaks. For this comparison only three most

intense peaks of each phase was considered as shown in Table 5.2. None of the diffraction patterns listed in the Table 5.2 showed any match with the unknown peaks. The diffraction pattern of the phase NiAlTa showed some match of  $2\theta$  angles with the  $2\theta$  angles for the unknown peaks. NiAlTa is a phase which is much removed from the  $\gamma'$  phase boundary. Table 5.3 compares the diffraction patterns of NiAlTa and the unknown phase.

Table 5.3 shows that though the two diffraction patterns show close match of peak positions near  $2\theta$  values of  $35^\circ$ ,  $40^\circ$ ,  $70^\circ$  and  $73^\circ$ , the intensity ratios are quite different for the two patterns. Moreover, all lines of equal high intensity ( $I/I_0 = 100$ ) in the diffraction pattern of NiAlTa do not show up in the pattern of the unknown phase. Hence we conclude that the unknown phase, can not be NiAlTa.

Since it was not possible to find the source of the extra diffraction peaks in the stable phases of Ni-Ta, Ni-Al and Ni-Al-Ta systems it was concluded that the diffraction lines are due to an extraneous source. The possibility of oxides, borides etc. were considered next but this also failed to account for the extra diffraction peaks. Since the powder for X-ray diffraction work was filed using a steel file, there is a possibility of contamination of the powder due to the file material (steel). The extra diffraction lines could not be accounted for on the basis of this

Table 5.2 : Comparison of the Set of Unknown Peaks with the Diffraction Patterns of Phases in the Ni-Al-Ta System

| Unknown phase    |       |       |       | $\gamma$<br>(Ref. 2)<br>f.c.c. |       |       | NiAl (Ref. 3)<br>Cubic |       |       |
|------------------|-------|-------|-------|--------------------------------|-------|-------|------------------------|-------|-------|
| I/I <sub>0</sub> | 100   | 75    | 50    | 100                            | 42    | 21    | 100                    | 70    | 40    |
| d                | 2.57  | 2.225 | 1.57  | 2.034                          | 1.762 | 1.246 | 2.02                   | 1.179 | 2.87  |
| 2 $\theta$       | 34.91 | 40.54 | 58.57 | 44.54                          | 51.89 | 76.44 | 44.87                  | 81.77 | 31.16 |

| Ni <sub>6</sub> AlTa (Ref.4)<br>Hexagonal |       |       | Ni <sub>2</sub> AlTa (Ref.5)<br>Cubic (L2 <sub>1</sub> ) |       |       | Ni <sub>3</sub> Ta (Ref.6)<br>Monoclinic |       |       |       |
|---|-------|-------|--|-------|-------|--|-------|-------|-------|
| I/I <sub>0</sub>                          | 100   | 50    | 30   | 100   | 70    | 20                                       | 100   | 80    | 70    |
| d   | 1.96  | 2.09  | 3.04   | 2.10  | 3.44  | 1.79                                     | 2.05  | 1.89  | 2.11  |
| 2 $\theta$                                | 46.32 | 43.29 | 29.38  | 43.07 | 25.89 | 51.02                                    | 44.18 | 48.14 | 42.86 |

| Ni <sub>3</sub> Ta (Ref. 7)<br>Tetragonal |       |      | Ni <sub>3</sub> Ta (Ref.8)<br>Orthorhombic |       |       | Ni <sub>8</sub> Ta (Ref.9)<br>Tetragonal |       |       |      |
|---|-------|------|--|-------|-------|--|-------|-------|------|
| I/I <sub>0</sub>                          | 100   | 80   | 80   | 100   | 70    | 70                                       | 100   | 60    | 20   |
| d   | 2.11  | 1.30 | 1.10                                       | 1.97  | 2.10  | 1.99                                     | 1.27  | 2.07  | 1.8  |
| 2 $\theta$                                | 42.85 | 72.7 | 88.98                                      | 46.07 | 43.07 | 45.58                                    | 74.70 | 43.73 | 50.7 |

| Ni <sub>8</sub> AlTa (Ref. 10) |      |      |      |
|--------------------------------|------|------|------|
| I/I <sub>0</sub>               | 100  | 20   | 10   |
| d                              | 1.92 | 2.00 | 2.07 |
| 2 $\theta$                     | 47.3 | 45.3 | 43.7 |

Table 5.3 : Comparison of the Set of unknown peaks with the Diffraction Pattern of NiAlTa Phase

| Ni Al Ta (11) |                  |        | Unknown Phase |                  |        |
|---------------|------------------|--------|---------------|------------------|--------|
| d             | I/I <sub>0</sub> | 2θ     | d             | I/I <sub>0</sub> | 2θ     |
| 4.28          | 15               | 20.75  |               |                  |        |
| 2.48          | 75               | 36.22  | 2.569         | 100              | 34.915 |
| 2.262         | 100              | 39.85  | 2.23          | 75               | 40.540 |
| 2.108         | 100              | 42.90  | 21.574        | 50               | 58.665 |
| 1.434         | 50               | 65.038 |               |                  |        |
| 1.388         | 100              | 67.47  |               |                  |        |
| 1.349         | 100              | 69.70  | 1.342         | 40               | 70.125 |
| 1.281         | 100              | 73.99  | 1.285         | 15               | 73.700 |
| 1.241         | 100              | 76.805 |               |                  |        |
| 1.185         | 100              | 81.16  |               |                  |        |

possibility as no diffraction peak due to Fe could be detected.

The diffraction pattern due to the unknown phase (the extra diffraction peaks in Ta containing alloys) appears to be somewhat simple. An attempt was made to index the extra diffraction lines of alloy containing 7 at% Ta and B on the basis of a cubic structure. As shown in Table 5.4 all the diffraction lines, due to the unknown phase could be indexed on the basis of a fcc cell.

Table 5.4 : Indexing of the Unknown Peaks of B-doped 7 at% Ta alloy on the basis of a f.c.c. Structure  
Lattice Parameter = 4.4500 Å (Std.Dev.=8x10<sup>-4</sup>)

| 2θ     | d = $\frac{\lambda}{2\sin\theta}$ | hkl | I/I <sub>0</sub> | d<br>Calculated |
|--------|-----------------------------------|-----|------------------|-----------------|
| 34.915 | 2.569                             | 111 | 100              | 2.569           |
| 40.540 | 2.225                             | 200 | 75               | 2.225           |
| 58.665 | 1.574                             | 220 | 50               | 1.573           |
| 70.125 | 1.342                             | 311 | 40               | 1.342           |
| 73.700 | 1.285                             | 222 | 15               | 1.285           |
| 87.735 | 1.112                             | 400 | 10               | 1.112           |
| 98.000 | 1.021                             | 331 | 40               | 1.021           |

The set of diffraction peaks due to the unknown phase with the diffraction pattern of TaC in Table 5.5.

Table 5.5 : Comparison of the Set of Unknown Peaks with the Diffraction Pattern of TaC

| Observed Values |               |       |                  | Values From ASTM Data CARD FOR Ta |                  |     |
|-----------------|---------------|-------|------------------|-----------------------------------|------------------|-----|
| Line No.        | Unknown Phase |       |                  | d                                 | I/I <sub>0</sub> | hkl |
|                 | 2θ            | d     | I/I <sub>0</sub> |                                   |                  |     |
| 1               | 34.915        | 2.569 | 100              | 2.57                              | 100              | 111 |
| 2               | 40.540        | 2.225 | 75               | 2.23                              | 70               | 200 |
| 3               | 58.665        | 1.574 | 50               | 1.58                              | 50               | 220 |
| 4               | 70.125        | 1.342 | 40               | 1.34                              | 40               | 311 |
| 5               | 73.700        | 1.285 | 15               | 1.28                              | 20               | 222 |
| 6               | 87.735        | 1.112 | 10               | 1.11                              | 20               | 400 |
| 7               | 98.000        | 1.021 | 40               | 1.02                              | 40               | 331 |

The excellent match of the diffraction patterns (in Table 5.5) prompted further speculation on the possible source of C in the Ni-Al-Ta alloys. The microstructures of the alloys had revealed precipitation of a phase along grain boundaries. This phase was found to chip off easily during polishing, indicating the phase to be brittle. Microhardness taken on these precipitated particles gave very high values compared to those of the surrounding matrix. All these results indicate that the unknown phase is a hard and brittle substance, such as a carbide. Since the diffraction pattern of the unknown phase matches very well with that of TaC, the unknown phase may be TaC.

Carbon was not an intentional or intended additive for the alloys that had been melted for the present study. Yet there must have been some source of carbon due to which TaC precipitated out in such large amounts that the entire diffraction pattern of TaC could be recorded.

The carbon could have come from the raw materials, i.e., the ingredients used for melting the alloys. Owing to the unavailability of equipment, we could not have accurately assay the ingredients for their carbon content. However, the purity of the elemental Ni and Al that had been used was 99.99%. Ta sheet of purity 99.9% had been used. That the Ta was in sheet form, indicates that its



carbon content, as well as concentration of other interstitial atoms in Ta is very low. The only other ingredient we used was the master alloy supplied by the DMRL. Since all the alloys, irrespective of whether prepared by using the master alloy or not, showed the TaC peaks, we could infer that the source of carbon was not the master alloy.

Carbon could come from the process of alloy preparation. Melting was done in argon-purged and evacuated arc-melting furnace using non-consumable W electrode and water-cooled Cu hearth. Some samples were melted at DMRL, while others at I.I.T. Kanpur. All the samples showed TaC peaks. So carbon pick-up from melting can be ruled out.

Heat treatment was done by keeping the samples in evacuated silica capsules. Carbon pick-up from this stage is also not possible.

The only other source of carbon could have been the diamond cutter which had been used to cut the ingredients as well as the melted buttons. Possibly, some diamond particles had got embedded into the material while cutting the raw material. During melting there was thorough mixing of the carbon and it possibly reacted with Ta, which on heat treatment precipitated out as TaC. The number of diamond particles getting embedded, would naturally differ from sample to sample. Hence the amount of carbides would also differ from sample to sample, depending upon the

number of diamond particles embedded. In other words, a systematic increase in the amount of TaC with increasing Ta content is not to be expected. A study of the microstructures reveals that the amount of dark holes (assumed to be created by chipping out of TaC particles during polishing) does not show any systematic variation with Ta content, except for alloys with low Ta content.

Hence we conclude that the extra peaks appearing in the alloys which contain Ta, are due to TaC. The carbide formed due carbon pick up from diamond particles which were embedded into the material during cutting on the diamond cutter. However, the validity our conclusion could have been verified if an alloy had been prepared without using the diamond cutter. Disappearance of the TaC peaks in that case would have confirmed our conclusion. This could not be done owing to the lack of time.

## 5.5 MICROSTRUCTURE AND PHASE BOUNDARY

Besides the peaks due to TaC and  $\text{Ni}_3\text{Al}$ , there was no other extra peak in any of the diffraction patterns. Microstructures for alloys containing upto 7 at % did not show any other phase whereas in the 9 at % Ta alloy small amount of a phase other than the  $\text{Ni}_3\text{Al}$  and TaC was present. As diffraction peaks of a phase will be visible only if the amount of the phase is more than 5-6 volume %, the amount of the new phase in the 9 at %, alloy was too

small to give any diffraction<sup>pattern</sup>. Microhardness measurements on this phase yielded values similar to those of the matrix ( $\text{Ni}_3\text{Al}$ ). Owing to the unavailability of electron microscope, this phase could not be identified.

It was noticed that the microstructures of alloys containing less than 9 at % Ta, did not show this phase. The phase seen in Figure 4.17 for the 7 at % Ta alloy is typical of this alloy only. This phase is seen only near areas of large cavities. These cavities may have been created by chipping out of some precipitate particles (not necessarily TaC) and further etching. Some local variation in composition of the matrix due to massive precipitation must have caused this new phase to occur. This phase, is microstructurally different from the phase in the 9 at % alloys. For instance, the phase in the 7 at % Ta alloy is not visible before etching whereas the phase seen in the microstructure of 9 at % Ta alloy was visible without etching. Hence, if we assume the unidentified phase in the 9 at % Ta alloys as one of the Ni-Al-Ta phases, we can conclude that the phase boundary of  $\text{Ni}_3\text{Al}$  lies somewhere in between 7 at % and 9 at % Ta. This corroborates well with literature data (Figure 2.6), which shows that with decrease in temperature from  $1250^\circ\text{C}$  to  $1000^\circ\text{C}$ , the phase boundary along the 75 at % Ni line decreases from 10 at % Ta to about 8 at % Ta.

## 5.6 ANALYSIS OF THE SPLIT DIFFRACTION PEAKS

The diffraction pattern of the alloys which were equilibrated at  $1000^{\circ}\text{C}$  showed splitting of all the  $\text{Ni}_3\text{Al}$  peaks. As recorded in Table 4.5, both the fundamental and superlattice peaks of  $\text{Ni}_3\text{Al}$  have split. There can be many reasons for splitting of peaks. For example, tetragonality may give rise to splitting of diffraction peaks. But in that case the fundamental reflection (111) will not split.

In the literature there are reports of precipitation of FCC  $\gamma$  phase giving rise to splitting of the peaks (12,13). Owing to prolonged ageing at  $1000^{\circ}\text{C}$  there is a loss of coherency  $\gamma$  and  $\gamma'$  and hence the peaks of  $\gamma$  are resolved. As  $\gamma$  has an FCC structure, with a lattice parameter very close to that of  $\gamma'$ , their peaks are very close and may give an appearance of split in  $\text{Ni}_3\text{Al}$  peaks. But this separation of  $\gamma$  and  $\gamma'$  peaks will occur for only the fundamental reflection as  $\gamma$  has an FCC structure. In the reported splitting of diffraction peak (12,13), the (004) peak was considered, possibly for reasons of greater resolution achievable at the higher  $2\theta$  angle. The (004) is a fundamental reflection. In this report it was also stated that no split of superlattice reflection (003) was detected. In the present investigation however, all  $\text{Ni}_3\text{Al}$  reflections have split, as shown in Table 4.5.

The only other explanation for the split of all diffraction peaks of  $\text{Ni}_3\text{Al}$  phase would be the formation of two phases. Since both the sets of split peaks can be indexed on the basis of cubic structure similar to  $\text{Ni}_3\text{Al}$  (Table 4.5), it appears that there must exist a miscibility gap in the  $\text{Ni}_3\text{Al}$  phase region, i.e., the  $\gamma'$  phase should give rise to two phases  $\gamma'_1$  and  $\gamma'_2$  one rich in Ni and the other rich in Al respectively. In the Ni-Al binary  $\gamma'$  phase region has a width of about 5 at % near  $1000^\circ\text{C}$ . Hence the compositions of the two phases  $\gamma'_1$  and  $\gamma'_2$  can not be very much different from that of the stoichiometric  $\text{Ni}_3\text{Al}$ .

As reported in literature (14), and shown in Table 5.6, the lattice parameter of  $\text{Ni}_3\text{Al}$  increases with increasing Al-content. This should be expected since the atomic radius of Al (1.41) is greater than that of Ni (1.26). On the basis of this we assume that of the two phases separated by the miscibility gap, the one with the larger lattice parameter is the Al-rich phase, and the one with the smaller lattice parameter, is the Ni-rich phase.

#### 5.6.1 DIFFERENTIAL SCANNING CALORIMETRY

Since at  $1200^\circ\text{C}$  the  $\gamma'$  phase exists and at  $1000^\circ\text{C}$  two phases  $\gamma'_1$  and  $\gamma'_2$  exist due to the presence of a miscibility gap, it is expected that if the  $1000^\circ\text{C}$  annealed alloy is heated to higher temperatures, there will be a change

Table 5.6 : Lattice Parameter of  $\text{Ni}_3\text{Al}$  as a Function of Composition

| At % Al | Anneal Temperature $^{\circ}\text{C}$ |                         |                        |
|---------|---------------------------------------|-------------------------|------------------------|
|         | 1150 $^{\circ}\text{C}$               | 1000 $^{\circ}\text{C}$ | 750 $^{\circ}\text{C}$ |
| 25.1    | 3.5588                                | 3.5592                  | 3.5603                 |
| 25.9    | -                                     | -                       | 3.5599                 |
| 27.8    | 3.5630                                | 3.5631                  | 3.5624                 |

in composition of the  $\gamma_1'$  and  $\gamma_2'$  phases and at some temperature between  $1000^\circ\text{C}$  and  $1200^\circ\text{C}$  there will be change over from  $\gamma_1' + \gamma_2' \longrightarrow \gamma'$ . Since the reaction should take place over a range of temperature, any thermal effect associated with this transformation ( $\gamma_1' + \gamma_2' \rightarrow \gamma'$ ) will be spread over a range of temperatures. To check whether such a transformation is detectable, DSC runs were made with two specimens, one containing no Ta and the other with 1 % Ta.

The DSC traces, Figure 4.30 show several thermal effects. Two small exothermic reactions occur at the lower temperatures - one at  $\sim 210^\circ\text{C}$  and the other over a small range of of temperature  $450^\circ\text{C}$  to  $570^\circ\text{C}$ . This is followed by an endothermic effect over a wide range of temperature, starting at  $\sim 900^\circ\text{C}$  and ending at  $\sim 1100^\circ\text{C}$  and a very sharp endothermic reaction at  $\sim 1130^\circ\text{C}$ . During cooling of the alloy, after the heating run in DSC, both the high temperature thermal effects do not show up whereas the low temperature thermal effects show up as endothermic reactions. On heating the sample upto  $\sim 500^\circ\text{C}$  cooling it room temperature and again heating it also reproduces both the low temperature reactions and shows that both the low temperature transformations are completely reversible. The low temperature thermal effects and the sharp endothermic reaction at  $\sim 1130^\circ\text{C}$  are not understood at present but the thermal effect observed between  $900^\circ\text{C}$  to  $1100^\circ\text{C}$  match will with the expected behaviour of a two phase alloy undergoing a transformation with change in temperature. Since the reaction takes place over a range of temperature it is not

possible to accurately determine the end point of  $\gamma_1' + \gamma_2' \rightarrow \gamma'$  reaction, it is expected to be slightly below  $1100^\circ\text{C}$ . Further experimentation is needed to establish the true transition temperature.

## 5.7 STRUCTURAL ANALYSIS OF THE SPLIT DIFFRACTION PEAKS

If on annealing  $\text{Ni}_3\text{Al}$  phase at low temperatures bring about the miscibility gap reaction  $\gamma' \rightarrow \gamma_1' + \gamma_2'$  then it may be possible to verify this by proper phase identification through chemical composition analysis using EPM technique. Since this was not possible to do at present, another method was adopted for this verification. Ni-Al and Ni-Al-Ta systems involve elements which have very wide variation in their atomic numbers as well as a large difference in their atomic radii.  $\text{Ni}_3\text{Al}$  is a cubic ordered structure with 4 atoms/cell, of which Al occupies the cell corners and Ni the face centre positions in the cubic cell. Any off stoichiometry composition is to increase the Ni or Al content of the cell. This will result in occupancy of Ni as well as Al in the cell corners if Ni content increases or in the cell face centres if Al content increases. The large difference between the atomic scattering factors of Ni and Al is expected to drastically affect the intensity of diffracted beam. Since Ta is the largest size atom and is reasonably close to the size of



Al atom, it is expected that Ta will go into the sites preferred by Al. Ta has the highest atomic scattering factor among the three elements and hence again intensity of diffracted beam is expected to be affected rather drastically with Ta addition. On these assumptions diffraction line intensity calculations may show whether the split diffraction peaks for  $\text{Ni}_3\text{Al}$  or  $\text{Ni}_3(\text{Al}, \text{Ta})$  alloys can be justified by assuming the existence of a miscibility gap.

Initially, structure factor calculations are made for pure  $\text{Ni}_3\text{Al}$  and calculated intensity ratios are compared with the intensity ratios for  $\text{Ni}_3\text{Al}$  containing Boron. Then assuming a split in composition, calculations are made for  $\text{Ni}_3\text{Al}$  at  $1000^\circ\text{C}$ . Finally, the contribution of Ta is considered in a 1 atom % Ta alloy. In all the calculations, the low atomic number element B is not considered as its contribution to diffracted beam intensity is expected to be very small because it is expected to go in industrial solid solution. The following sections show the calculations.

#### 5.7.1 INTENSITY CALCULATIONS FOR $\text{Ni}_3\text{Al}$ AT $1000^\circ\text{C}$

The peaks for  $\text{Ni}_3\text{Al}$  phase  $\gamma$  split up at  $1000^\circ\text{C}$ . We assume that this occurs due to the formation of two phases,  $\gamma_1$  and  $\gamma_2$ , one of which is rich in Ni, the other rich in Al. The compositions of the  $\gamma_1$  and  $\gamma_2$  phases are not known. As the  $\text{Ni}_3\text{Al}$  phase extends to about 3 atomic

percent on either side of the stoichiometric composition, we assume that the composition of the Ni-rich phase is 78 at % Ni, 22 at % Al. and that of the Al-rich phase is 72 at% Ni, 28 at% Al, i.e., correspond to the  $\text{Ni}_3\text{Al}$  phase boundaries. The intensities of the diffracted beams calculated on this basis are given below (Refer Appendix C for details of calculations).

### Ni-Rich Phase

The composition for this phase is 78 at % Ni, 22 at% Al. Since there is excess Ni compared to the stoichiometric composition, the face-centre positions will be fully occupied by Ni atoms, while the cube corners will be occupied by both Al and Ni. Hence, for the (000) sites, we have to use  $f_{\text{Avg}} = m_{\text{Al}} f_{\text{Al}} + m_{\text{Ni}} f_{\text{Ni}}$  where  $m_{\text{Al}}$  and  $m_{\text{Ni}}$  are the atomic fractions of Al and Ni atoms occupying the (000) site. The Al and Ni atoms in the (000) site are present in the ratio 22:3. Therefore,  $f_{\text{Avg}}$  for the (000) site is  $f_{\text{Avg}} = \frac{22}{25} f_{\text{Al}} + \frac{3}{25} f_{\text{Ni}} = 0.88 f_{\text{Al}} + 0.12 f_{\text{Ni}}$ . The solution of the structure factor equation is then given as

$$|F|^2 = (f_{\text{Avg}} + 3f_{\text{Ni}})^2 \text{ for fundamental lines} \quad (5.1)$$

$$|F|^2 = (f_{\text{Avg}} - f_{\text{Ni}})^2 \text{ for superlattice lines} \quad (5.2)$$

### Al-Rich Phase

The composition of this phase is 72 at % Ni, 28 at % Al. The (000) sites are fully occupied by Al atoms.

Assuming random substitution of the excess Al atoms in the three face center positions, and since the Ni atoms and Al atoms in the Ni sub-lattice (face-center positions) are in the ratio 72:3, the  $f_{\text{Avg}}$  is given by

$$f_{\text{Avg}} = \frac{72}{75} f_{\text{Ni}} + \frac{3}{75} f_{\text{Al}} = 0.96 f_{\text{Ni}} + 0.04 f_{\text{Al}}$$

The structure factors are given by:

$$|F|^2 = (f_{\text{Al}} + 3 f_{\text{Avg}})^2 \quad \text{for fundamental lines} \quad (5.3)$$

$$|F|^2 = (f_{\text{Al}} - f_{\text{Avg}})^2 \quad \text{for superlattice lines} \quad (5.4)$$

The calculated, sealed relative integrated intensities are given in Table 5.7 (refer Appendix C for calculations).

Table 5.7 : Calculated and Observed Relative Intensities of the Phases Separated in  $\text{Ni}_3\text{Al}$  at  $1000^\circ\text{C}$  due to a Miscibility Gap

| Line | hkl | $\theta$       | Ni Rich Phase          |                      | Al-rich Phase          |                      |
|------|-----|----------------|------------------------|----------------------|------------------------|----------------------|
|      |     |                | Calculated<br>(scaled) | Observed<br>(scaled) | Calculated<br>(scaled) | Observed<br>(scaled) |
| 1    | 100 | $12.47^\circ$  | 0.78                   | 1.72                 | 1.01                   | 2.50                 |
| 2    | 110 | $17.775^\circ$ | 0.58                   | 1.36                 | 0.75                   | 1.60                 |
| 3    | 111 | $21.965^\circ$ | 10.00                  | 10.00                | 10.00                  | 10.00                |
| 4    | 200 | $25.586^\circ$ | 4.64                   | 4.50                 | 4.65                   | 4.52                 |

The observed peak intensities are based on peak height measurement from the X-ray diffraction patterns.

### 5.7.2 INTENSITY CALCULATIONS FOR $\text{Ni}_3\text{Al}$ WITH 1 ATOM % Ta AND CONTAINING B, AT 1000°C

We assume the Ta goes to substitute Al in a random fashion.

#### Ni-Rich Phase

The composition for the Ni-rich phase is 78 at % Ni, 21 at % Al, 1 at % Ta. The Ni sub-lattice is fully occupied by Ni atoms, while the (000) sites (Al sub-lattice) is occupied by Al, Ni and Ta atoms in the ratio 21:3:1 respectively.

$$\begin{aligned} \therefore f_{\text{Avg}} &= \frac{21}{25} f_{\text{Al}} + \frac{3}{25} f_{\text{Ni}} + \frac{1}{25} f_{\text{Ta}} \\ &= 0.84 f_{\text{Al}} + 0.12 f_{\text{Ni}} + 0.04 f_{\text{Ta}} \end{aligned}$$

The structure factors are given as

$$|F|^2 = (f_{\text{Avg}} + 3 f_{\text{Ni}})^2 \quad \text{for fundamental lines} \quad (5.5)$$

$$|F|^2 = (f_{\text{Avg}} - f_{\text{Ni}})^2 \quad \text{for superlattice lines} \quad (5.6)$$

#### Al-Rich Phase

The composition of this phase is 72 at % Ni, 27 at % Al, 1 at % Ta. Here we consider the contribution of Al and Ta to the atomic scattering factor, together

$$\text{i.e. } f_{\text{Al,Ta}} = \frac{27}{28} f_{\text{Al}} + \frac{1}{28} f_{\text{Ta}} = 0.96 f_{\text{Al}} + 0.04 f_{\text{Ta}}$$

and  $f_{\text{Avg}}$  for the face-center positions is:

$$f_{\text{Avg}} = \frac{72}{75} f_{\text{Ni}} + \frac{3}{75} f_{\text{Al,Ta}} = 0.96 f_{\text{Ni}} + 0.04 f_{\text{Al,Ta}}$$

The structure factors are given by:

$$|F|^2 = (f_{\text{Al,Ta}} + 3 f_{\text{Avg}})^2 \text{ for fundamental lines} \quad (5.7)$$

$$|F|^2 = (f_{\text{Al,Ta}} - f_{\text{Avg}})^2 \text{ for superlattice lines} \quad (5.8)$$

Calculation, similar to those shown in Appendix C, were done to obtain the scaled relative integrated intensities. Table 5.8 shows the comparison between the calculated and observed values.

Table 5.8 : Calculated and Observed Relative Intensities of the Phases Separated in  $\text{Ni}_3\text{Al}$  with 1 at %Ta due to Miscibility Gap at  $1000^\circ\text{C}$

| Line | hkl | $\theta$       | Ni-rich Phase               |  |                                | Al-rich Phase               |   |                                |
|------|-----|----------------|-----------------------------|--|--------------------------------|-----------------------------|---|--------------------------------|
|      |     |                | Calcu-<br>lated<br>(scaled) | Observed<br>Area<br>under<br>curve<br>(scaled) | Step*<br>scan<br>(se-<br>aled) | Calcu-<br>lated<br>(scaled) | Observed<br>Area<br>under<br>curve<br>(sca-<br>led) | Step*<br>scan<br>(scal-<br>ed) |
| 1    | 100 | $12.47^\circ$  | 0.48                        | 1.44   | 1.07                           | 0.68                        | 2.41  | 1.95                           |
| 2    | 110 | $17.775^\circ$ | 0.35                        | 1.10   | 0.86                           | 0.50                        | 1.96  | 1.48                           |
| 3    | 111 | $21.965^\circ$ | 10.00                       | 10.00  | 10.00                          | 10.00                       | 10.00   | 10.00                          |
| 4    | 200 | $28.87^\circ$  | 4.64                        | 4.20   | 4.38                           | 4.64                        | 4.24  | 4.68                           |

\*

The peak height was only measured by the step scan technique. This column does not give relative integrated intensities, while the others do.

In our calculations for the data in Tables 5.7 and 5.9 we had chosen ideal structure with a degree of order equal to one. Moreover, only atomic scattering factor, multiplicity factor and Lorentz polarization factor were considered for the intensity calculations. Other factors were neglected. Owing these reasons the absolute values of the calculated scaled relative intensities do not show close match with the observed values. However, if ratios of intensities are taken, the extraneous factors will get cancelled. From Table 5.8 we see that the ratio of intensities of the (100) reflection for the Ni-rich phase and the Al-rich phase is between 0.6 and 0.7 for both the calculated and observed values. A similar match is observed for (200) reflections

Table 5.8 shows that though the absolute values of the calculated and observed scaled relative intensities do not match closely, the trend of the scaled intensities match. That is, Line 1 (for the 100 reflection) is stronger than Line 2 (for the 110, reflection) in all the cases, without any exception. Moreover, the ratio of the calculated scaled relative intensities for the first two superlattice lines matches very closely with that of the observed scaled relative intensities as shown in Table 5.10.

Table 5.9 : Ratio of the Scaled Relative Intensities  
of the First Two Superlattice Lines  
(100 and 110 reflections)

| Ratio = $\frac{\text{Line 1}}{\text{Line 2}}$ | Ni-rich Phase | Al-rich Phase |
|---|---------------|---------------|
| Calculated ratio                              | 1.37          | 1.36          |
| Observed ratio<br>(area under curve)          | 1.31          | 1.34          |
| Observed ratio<br>(step scan)                 | 1.24          | 1.32          |

This indicates that the calculated values and observed values of intensities are consistent in their trends.

On comparing Tables 5.7 and 5.8, it will be noticed that the calculated scaled relative intensities of the superlattice lines have decreased on addition of 1 at % Ta. Figure 5.1 shows the split 100 peaks for boron doped  $\text{Ni}_3\text{Al}$  without Ta and containing 1 at % Ta. The experimentally obtained diffraction peaks also show the same trend as predicted by the intensity calculations, i.e., the intensity of the superlattice reflections decrease with addition of Ta. A close inspection of equation 5.8 will reveal that the contribution of Ta decreases the difference between  $f_{\text{AlTa}}$  and  $f_{\text{Avg}}$ , thus decreasing the calculated intensities for the superlattice lines.

That the results of structure factor calculations predict the experimental results with reasonable accuracy, indicates that the assumptions we had made were correct. This proves, firstly, that Ta substitutes Al in  $\text{Ni}_3\text{Al}$ , and secondly, what is of most significance is that the hypothesis regarding the existence of a miscibility gap in  $\text{Ni}_3\text{Al}$  is verified.

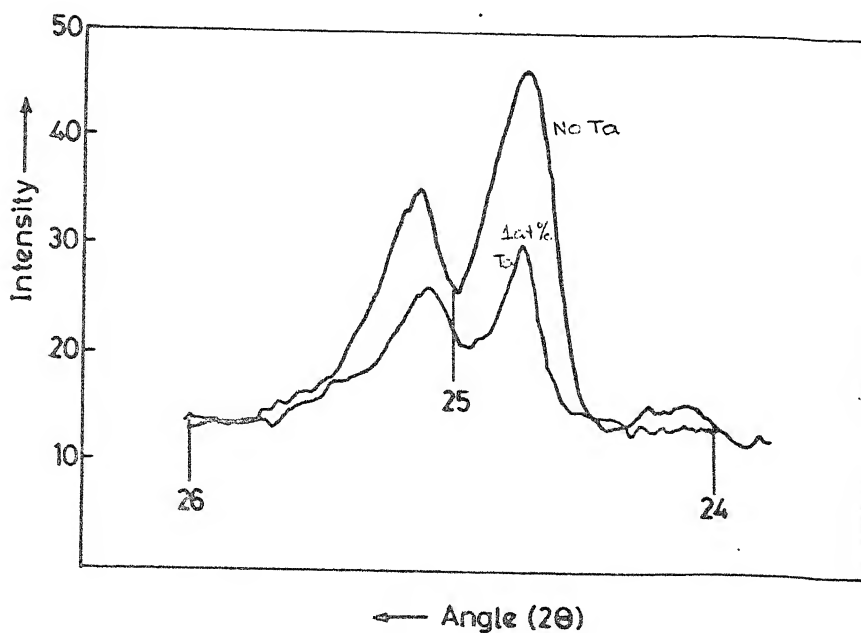


Fig. 5.1 The  $\theta$  split (100) peaks for Boron-doped  $\text{Ni}_3\text{Al}$  without  $\text{Ta}_x$  and containing 1 at % Ta.



REFERENCES

1. P. Willemin, C. Dugue, M. Durand-Charre and J.H. Davidson, Mat. Sc. & Tech., Vol. 2, April 1986, p. 314.
2. ASTM Data Card No. 4-850.
3. ASTM Data Card No. 2-1261.
4. ASTM Data Card No. 34-1284.
5. ASTM Data Card No. 30-31.
6. ASTM Data Card No. 19-855.
7. ASTM Data Card No. 18-893.
8. ASTM Data Card No. 17-699.
9. ASTM Data Card No. 23-438.
10. ASTM Data Card No. 34-1278.
11. ASTM Data Card No. 18-45.
12. M.V. Nathal, R.A. MacKay, R.G. Garlick, Scr. Met., Vol. 22, 1988, pp. 1421-1424.
13. M.V. Nathal, R.A. MacKay, R.G. Garlick, Mat. Sci. Engg., Vol. 75, 1985, pp. 195-205.
14. W.B. Pearson, "A Handbook of Lattice Spacings and Structures of Metals and Alloys, Pergamon Press, p. 379.

CHAPTER 6CONCLUSIONS

From the experimental results and the analysis of those results, the following conclusions can be drawn:

1. X-ray diffraction patterns of all alloys containing Ta and the high microhardness values of grain boundary precipitate particles indicate that TaC has precipitated in the alloys.
2. Carbon was not an intentional addition. It was inferred that the carbon required for the formation of TaC may have come from the diamond cutter. Small pieces of diamond may have got embedded into the materials while cutting.
3. The solubility limit of the  $\text{Ni}_3\text{Al}$  phase was found from microstructural studies to be between 7 at % to 9 at % Ta along the 75 at % Ni line.
4. Boron had no observable effect on the solubility limit.
5. Increase of lattice parameter with addition of Ta and intensity calculations confirmed that Ta substitutes Al in  $\text{Ni}_3\text{Al}$ .
6. Analysis of split diffraction peaks appearing at  $1000^\circ\text{C}$  and intensity calculations verify that a miscibility gap exists in the  $\text{Ni}_3\text{Al}$  phase region.

## CHAPTER 7

### SCOPE FOR FUTURE WORK

The conclusions of the present work leave much scope for future work. Firstly, the source of carbon, which contaminated the alloys and caused precipitation of TaC, has to be determined. For this, alloys have to be prepared by taking precautions to prevent carbon contamination. Initially, the ingredients have to accurately assayed for their carbon contents. The diamond cutter being a potential source of carbon in the process of alloy preparation, the alloys should be melt after grinding off the cut surfaces to remove any embedded carbon. The alloys thus prepared should be assayed for carbon. The diffraction patterns of the alloys should checked for TaC peaks.

The 9 at % Ta alloys show a phase besides TaC and the matrix. Electron microscopy studies should be done to identify this phase.

The lattice parameter of alloys containing Boron shows lower values than for alloys without Boron. This should be investigated further for the possibility of formation of Borides of Ta and Al.

The most important result of the present work was the splitting of all the  $\text{Ni}_3\text{Al}$  peaks. This splitting was explained on the basis of a miscibility gap in the  $\text{Ni}_3\text{Al}$ .

The existence of such a miscibility gap has not been reported before. Further work should be done to investigate the possibility of a miscibility gap. EPM analysis should be done to detect any variation in composition in the grains. The Ni-Al-Ta-C quaternary has not been studied. Possibly, the carbon present in the alloys has caused the miscibility gap. This should be thoroughly investigated in future works.

APPENDIX ACALCULATION OF WEIGHT OF INGREDIENTS FOR MAKING  
15 GMS OF BORON DOPED ALLOY

The calculations involved converting the atomic percentages of Ni, Al and Ta to weights in gm of  $\text{Ni}_3\text{Al}$ , Ni (or Al) and Ta. The first step was to convert the atomic percentages to weight percentages of the elements. The following formula was used for the conversion:

$$\text{wt\%M} = \frac{\text{Atomic \% M} \times \text{Atomic weight M} \times 100}{\sum_i (\text{Atomic \% M}_i \times \text{Atomic weight M}_i)}$$

The effect of Boron is neglected as it is in very small quantity. The second step was to find out whether Nickel or Aluminium had to be added to  $\text{Ni}_3\text{Al}$ . Next, the composition of the alloy was expressed in terms of the weight percentages of  $\text{Ni}_3\text{Al}$ , Ni (or Al) and Ta. Finally, the required weight (in grams) of the components was computed in order to make an alloy with total weight of 15 grams. As an example, the calculations for alloy 5, containing 13 atomic % Ta and Boron, is shown below:

| <u>Element</u> | <u>Atomic %</u> | <u>Atomic Weight</u> | <u>Weight %</u> |
|----------------|-----------------|----------------------|-----------------|
| Ni             | 75              | 58.71                | 62.1984         |
| Al             | 12              | 26.98                | 4.5733          |
| Ta             | 13              | 180.95               | 33.2283         |

In  $\text{Ni}_3\text{Al}$ ,

$$\text{Weight \% Ni} = 86.71656$$

$$\text{Weight \% Al} = 13.28344$$

In alloy S,

$$\text{For } 4.5733 \text{ weight\%Al, weight\% Ni (from } \text{Ni}_3\text{Al)} = 29.85527$$

$$\text{For } 62.1984 \text{ weight\%Ni, weight\%Al (from } \text{Ni}_3\text{Al)} = 9.52769$$

Hence excess Nickel has to be added. The composition of Alloy S can now be expressed as:

$$29.85527 \text{ wt\%Ni} + 4.5733 \text{ wt\%Al} = 34.42857 \text{ wt\% } \text{Ni}_3\text{Al}$$

$$(62.1984 - 29.85527) \text{ wt\%Ni} = 32.34313 \text{ wt\%Ni}$$

$$33.2283 \text{ wt\%Ta}$$

∴ For 15 gms of Alloy S we shall need:

$$\text{Ni}_3\text{Al} = 34.42857 \text{ wt\%} = 5.16428 \text{ gm}$$

$$\text{Ni} = 32.34313 \text{ wt\%} = 4.85146 \text{ gm}$$

$$\text{Ta} = 33.2283 \text{ wt\%} = 4.98424 \text{ gm}$$

---


$$14.99998 \text{ gm}$$


---

APPENDIX BCALCULATIONS FOR LATTICE PARAMETER

For precise lattice parameter measurement initially a correction factor is determined to take care of the error in the goniometer. The diffraction pattern of a standard Si-sample is obtained, the angular positions of the peaks are measured and compared with the calculated peak positions. The error obtained by subtracting the two. Table A-1 shows a sample calculation for correction factor.

Table A-1 : Calculation and Correction Factor

| EXPERIMENTAL<br>2 $\theta$ |                       |                       | CALCULATED<br>2 $\theta$ |                       |                       | CORRECTION FACTOR<br>(Calculate 2 $\theta$ ) -<br>(Experimental 2 $\theta$ ) |                |                |
|----------------------------|-----------------------|-----------------------|--------------------------|-----------------------|-----------------------|--|----------------|----------------|
| For<br>CuK $\alpha$        | For<br>CuK $\alpha_1$ | For<br>CuK $\alpha_2$ | For<br>CuK $\alpha$      | For<br>CuK $\alpha_1$ | For<br>CuK $\alpha_2$ | CuK $\alpha$   | CuK $\alpha_1$ | CuK $\alpha_2$ |
| 47.19                      | -                     | -                     | 47.3673                  | -                     | -                     | 0.1773   |                |                |
| -                          | 56.03                 | 56.13                 | -                        | 56.1497               | 56.3012               | -  | 0.1197         | 0.1412         |
| -                          | 76.18                 | 76.40                 | -                        | 76.4166               | 76.6404               | -  | 0.2366         | 0.2404         |
| -                          | 87.83                 | 88.11                 | -                        | 88.0798               | 88.3549               | -  | 0.2498         | 0.2449         |
| -                          | 94.76                 | 95.06                 | -                        | 95.0085               | 95.3191               | -  | 0.2485         | 0.2591         |

The correction factor is plotted against angles. For the diffraction pattern of an alloy sample, the correction factor corresponding to a 2 $\theta$  - value is read directly from the plot and

is added to the  $2\theta$  value. The final corrected value of  $2\theta$  is used for calculating lattice parameter.

The lattice parameter corresponding to each peak is calculated using the formula:

$$a = (\lambda / 2 \sin \theta) \sqrt{h^2 + k^2 + l^2}$$

These lattice parameters are then plotted against the Nelson-Riley function:

$$\cos^2 \theta \left[ \frac{1}{\sin \theta} + \frac{1}{\theta} \right]$$

Slope of the plot is determined by using the relation:

$$\text{Slope} = \frac{\sum x \sum y - n \sum xy}{(\sum x)^2 - n \sum x^2}$$

where the  $x$  stands for the values of the Nelson-Riley function and  $y$  stands for the lattice parameters.

The extrapolated lattice parameter is, which is taken to be the parameter for the sample under study, is obtained from:

$$\text{Lattice parameter} = y_{\text{Avg}} - (\text{Slope} \times x_{\text{Avg}})$$

where  $y_{\text{Avg}}$  and  $x_{\text{Avg}}$  are the average values of  $y$  and  $x$ .



## APPENDIX C

### STRUCTURE FACTOR AND INTENSITY CALCULATIONS FOR ORDERED $\text{Ni}_3\text{Al}$

#### Atom Positions:

Ordered  $\text{Ni}_3\text{Al}$  has an  $\text{L1}_2$  type of structure. The Al atoms occupy the cubic corners, i.e., the 000 sites, and the Ni atoms occupy the face-center positions, i.e., the  $\frac{1}{2} \frac{1}{2} 0$ ,  $\frac{1}{2} 0 \frac{1}{2}$  and  $0 \frac{1}{2} \frac{1}{2}$  positions.

#### Structure Factor:

Since the structure of  $\text{Ni}_3\text{Al}$  is ordered, the contributions of atomic scattering factors of Al and Ni must be considered separately. Hence the structure factor of ordered  $\text{Ni}_3\text{Al}$  is:

$$F = f_{\text{Al}} + f_{\text{Ni}} \left[ e^{\pi i(h+k)} + e^{\pi i(k+l)} + e^{\pi i(l+h)} \right] .$$

#### Intensity of Diffracted Beams:

The intensity of the diffracted beams depends upon the square of the structure factor, the multiplicity factor, Lorentz polarization factor, temperature factor, absorption factor etc. Since we need only the relative intensities, except the first three all other factors are neglected.

$$\text{i.e. } I \propto |F|^2 \cdot m \cdot (\text{L.P.})$$

m being the multiplicity factor and L.P. the Lorentz Polarization Factor.

Table A-2 shows the calculations for scaled relative intensities and also compares the calculated values with the experimentally obtained values.

Table A.2 : The Calculated Relative Intensities Compared with Observed Relative Intensities of  $\text{Ni}_3\text{Al}$

| Line | hkl | $h^2+k^2+l^2$ | $\theta$ | $f_{\text{Ni}}$ | $f_{\text{Al}}$ | $ F ^2$ | p  | $\frac{1+\cos^2 2\theta}{\sin^2 \theta \times \cos \theta}$ | Relative Calculated  | Integrated Calculated (scaled) | Observed (scaled) |
|------|-----|---------------|----------|-----------------|-----------------|---------|----|---|----------------------|--------------------------------|-------------------|
| 1    | 100 | 1             | 12.47    | 23.2            | 10.05           | 172.9   | 6  | 40.026  | $4.15 \times 10^4$   | 1.44                           | 1.40              |
| 2    | 110 | 2             | 17.78    | 20.7            | 9.00            | 136.9   | 12 | 18.713  | $3.07 \times 10^4$   | 0.77                           | 0.65              |
| 3    | 111 | 3             | 21.96    | 18.9            | 8.45            | 424.5   | 8  | 11.710  | $39.76 \times 10^4$  | 10.00                          | 10.00             |
| 4    | 200 | 4             | 25.58    | 17.5            | 7.95            | 3654.2  | 6  | 8.286   | $18.17 \times 10^4$  | 4.57                           | 4.60              |
| 5    | 210 | 5             | 28.87    | 16.7            | 7.55            | 83.72   | 24 | 6.2940  | $1.26 \times 10^4$   | 0.32                           | 0.20              |
| 6    | 211 | 6             | 31.93    | 16.0            | 7.20            | 77.4    | 24 | 5.0300  | $0.934 \times 10^4$  | 0.23                           | Not resolved      |
| 7    | 220 | 8             | 37.64    | 14.6            | 6.60            | 2540.2  | 12 | 3.6050  | $10.99 \times 10^4$  | 2.76                           | 2.80              |
| 8    | 221 | 9             | 40.37    | 14.1            | 6.30            | 60.84   | 24 | 3.2090  | $0.568 \times 10^4$  | 0.117                          | Not resolved      |
| 9    | 310 | 10            | 43.07    | 13.75           | 6.10            | 58.5    | 24 | 2.9490  | $0.414 \times 10^4$  | 0.104                          | Not resolved      |
| 10   | 311 | 11            | 45.74    | 13.4            | 5.9             | 2125.2  | 24 | 2.795   | $14.256 \times 10^4$ | 3.58                           | 3.51              |
| 11   | 222 | 12            | 48.42    | 13.0            | 5.65            | 1993.6  | 8  | 2.731   | $4.356 \times 10^4$  | 1.09                           | 1.15              |

105851

74

669.967332 Date 5/10/93

B469e This book is to be returned on the  
date last stamped.

[illegible]

ME-1989-M-BHA-EFF

Th  
669.967332  
B.469e

A 105931